

The Effects of Alloy Chemistry on Localized Corrosion of Austenitic Stainless Steels

Submitted in partial fulfillment of the requirements
for the degree of
Doctor of Philosophy
in
Materials Science and Engineering

DAVID O. SAPIRO

B.A., Chemistry, Drew University
M.S., Materials Science Engineering, University of Washington
M.S., Materials Science Engineering, Carnegie Mellon University

Carnegie Mellon University
Pittsburgh, PA

September 2017

© David O. Sapiro, 2017 All Rights Reserved

Acknowledgements

The work presented herein was funded in part by the Oak Ridge Institute for Science and Education in collaboration with Paul Ohodnicki at the National Energy Technology Laboratory.

I would like to thank my adviser, Prof. Bryan Webler, for his guidance, and support throughout this project, as well as endorsement of my extracurricular metallurgical activities. I would also like to thank my committee, Prof. Chris Pistorius, Prof. Tony Rollett, and Dr. Brian DeForce, for their guidance.

This work would not have been possible without the help of the Webler group, as well as the Pistorius group and CISR. The Department of Materials Science staff, as well as Larry Hayhurst, were also instrumental in the completion of this work. This experience was also improved thanks to my bladesmithing group who competed with me at TMS bladesmithing competitions. I would also like to thank my friends and family for their continued support. I would particularly thank my mom, Kathy Sapiro, for the many hours she spent editing my writing. I would also particularly like to thank Whitney Schoenthal for supplying the cheesecake for my thesis defense, as well as the many long discussions about Materials Science.

Abstract

This study investigated localized corrosion behavior of austenitic stainless steels under stressed and unstressed conditions, as well as corrosion of metallic thin films. While austenitic stainless steels are widely used in corrosive environments, they are vulnerable to pitting and stress corrosion cracking (SCC), particularly in chloride-containing environments. The corrosion resistance of austenitic stainless steels is closely tied to the alloying elements chromium, nickel, and molybdenum. Polarization curves were measured for five commercially available austenitic stainless steels of varying chromium, nickel, and molybdenum content in 3.5 wt.% and 25 wt.% NaCl solutions. The alloys were also tested in tension at slow strain rates in air and in a chloride environment under different polarization conditions to explore the relationship between the extent of pitting corrosion and SCC over a range of alloy content and environment. The influence of alloy composition on corrosion resistance was found to be consistent with the pitting resistance equivalent number (PREN) under some conditions, but there were also conditions under which the model did not hold for certain commercial alloy compositions. Monotonic loading was used to generate SCC in 300 series stainless steels, and it was possible to control the failure mode through adjusting environmental and polarization conditions. Metallic thin film systems of thickness 10-200 nm are being investigated for use as corrosion sensors and protective coatings, however the corrosion properties of ferrous thin films have not been widely studied. The effects of film thickness and substrate conductivity were examined using potentiodynamic polarization and scanning vibrating electrode technique (SVET) on iron thin films. Thicker films undergo more corrosion than thinner films in the same environment, though the corrosion mechanism is the same. Conductive substrates encourage general corrosion, similar to that of bulk iron, while insulating substrates supported only localized corrosion.

Contents

Acknowledgements	ii
Abstract	iii
List of Figures	vii
List of Tables	xi
1 Introduction and Motivation	1
1.1 The Cost of Corrosion	1
1.2 The Importance of, and Failure of Stainless Steels	1
1.3 Corrosion Detection and Inhibition	3
1.4 Organization of this Document	3
2 Background	5
2.1 Materials	5
2.1.1 Stainless Steels	5
2.1.2 Thin Films	6
2.2 Corrosion	7
2.2.1 Conditions Leading to Corrosion	7
2.2.2 General Corrosion	10
2.2.3 Localized Corrosion	15
2.2.4 Thin Film Corrosion	16
2.3 Pit Solution Chemistry	23
2.3.1 Aqueous Chemistry	23
2.3.2 Aqueous Chemistry Within a Pit	25

2.4	Passivity and Corrosion of Stainless Steels	26
2.4.1	Localized Corrosion of Stainless Steels	26
2.4.2	Localized Corrosion of Stainless Steel Thin Films	33
2.4.3	Effect of Alloying on Passivity and Corrosion	38
2.4.4	Effect of Alloying on Passivity and Corrosion in Thin Films	44
2.5	Mechanical Behavior in Corrosive Environments - SCC Resistance	45
2.5.1	Effects of Alloy Chemistry on Mechanical Properties	45
2.5.2	Effect of Environment on Mechanical Properties	49
2.5.3	Crack Initiation and Pit to Crack Transition	50
3	Objectives	54
4	Hypotheses	56
5	Experimental Equipment	57
5.1	Instrumentation	57
5.2	Environmental Chambers	60
5.2.1	Avesta Cell	60
5.2.2	SVET Environmental Chamber	62
5.2.3	SSRT Environmental Chamber 1	64
5.2.4	Environmental Chamber 2	66
5.2.5	Environmental Chamber 3	68
6	Bulk Potentiodynamic Polarization	70
6.1	Experimental	70
6.1.1	Materials	70
6.1.2	Effects of Environmental Conditions	73
6.1.3	Effects of Temperature	73
6.2	Results and Discussion	73
6.2.1	Effects of Environmental Condition	73
6.2.2	Effects of Temperature	82
6.3	Discussion	86
7	Thin Films	90
7.1	Experimental Materials and Methods	90

7.1.1	Materials	90
7.1.2	Resistivity	91
7.1.3	Potentiodynamic Polarization	91
7.1.4	SVET	92
7.2	Results and Discussion of Fe and Fe-Pt Films	92
7.2.1	Resistivity	92
7.2.2	Polarization	95
7.2.3	SVET Environment Composition	98
7.2.4	Submerged SVET	103
7.3	Discussion	107
8	Slow Strain Rate Testing	110
8.1	Experimental	110
8.1.1	Preliminary Tests: Effect of Specimen Geometry	110
8.1.2	Effects of Polarization and Environment	113
8.2	Results and Discussion	115
8.2.1	Effect of Geometry	115
8.2.2	Effect of Polarization and Environment	123
8.3	Discussion	131
9	Conclusion	134
10	Future Work	135
10.1	Bulk Pitting	135
10.2	Thin Film Corrosion	135
10.3	Stress Corrosion Cracking	136
	References	138

List of Figures

2.1	Alloying and environmental effects on corrosion	8
2.2	Corrosion of constituents of stainless steel	9
2.3	Standard reduction potentials	12
2.4	Pourbaix diagram of Fe and Cr	13
2.5	Evans diagram	14
2.6	Fe bulk and thin film polarization	17
2.7	Carbon steel bulk and thin film polarization	18
2.8	Stainless steel bulk and thin film polarization curve	20
2.9	Nanocrystalline passive film nucleation	21
2.10	Effect of sputtering procedure on corrosion	22
2.11	Saturated chloride solutions	24
2.12	Cation concentration in passive film	27
2.13	Diffusion through passive film	28
2.14	Film thinning model	29
2.15	Film rupture model	30
2.16	Nucleation of pitting at inclusion particles	31
2.17	Thin film pit radius	34
2.18	Thin film pit depth	35
2.19	Thin film pit cover	36
2.20	Thin film pit growth	37
2.21	Thin film pit current	38
2.22	Polarization of Fe-Cr alloys	40
2.23	Carbide formation rates	41
2.24	Polarization of Fe-Cr-Ni-Mo alloys	43

2.25	Polarization of Fe-Cr alloy thin films	45
2.26	Molybdenum effect on K_{ISCC}	47
2.27	Nickel effect on K_{ISCC}	48
2.28	SCC crystallographic planes	51
2.29	Pit and SCC growth	52
2.30	SCC growth rates	53
5.1	SVET schematic	59
5.2	SVET current schematic	59
5.3	SVET potential schematic	60
5.4	Avesta Cell	61
5.5	SVET environmental chamber 1	62
5.6	SVET environmental chamber 2	63
5.7	SVET environmental chamber 3	63
5.8	Environmental chamber design 1	65
5.9	Environmental chamber design 2	67
5.10	Environmental chamber design 3	69
6.1	Microstructures	72
6.2	Polarization curves explained	75
6.3	Polarization curves	76
6.4	Pitting potentials	77
6.5	Polarization curves at 24 °C	78
6.6	Polarization curves at 24 °C	79
6.7	Polarization curves at 70 °C	79
6.8	Pitting potentials	80
6.9	Hysteresis loops	82
6.10	Cyclic polarization curves at 24 °C	82
6.11	Pitting potentials vs. temperature	84
6.12	Repassivation potentials vs. temperature	84
6.13	Difference between pitting and repassivation potentials	85
6.14	Pitting potentials vs. PREN	86
6.15	Pitting rate control	87
6.16	Metastable pitting	87

7.1	Measured Fe thin film resistivity	93
7.2	Thin film resistivity	93
7.3	Effect of electrolyte on resistivity	94
7.4	Fe thin film polarization curves	96
7.5	Fe and Fe+Pt thin film polarization curves	96
7.6	Ecorr vs. resistivity	97
7.7	Micrographs of corroded Fe thin films	98
7.8	SVET of Fe thin film	99
7.9	Micrographs of corroded iron thin films	100
7.10	SVET of Fe thin film on Pt+Ta	101
7.11	SVET min and max	102
7.12	SVET of 20 nm Fe thin film	104
7.13	SVET of 100 nm Fe thin film	104
7.14	SVET of 20 nm Fe thin film with Pt+Ta	105
7.15	SVET of 100 nm Fe thin film with Pt+Ta	105
7.16	SVET min and max	106
7.17	Ecorr vs. resistivity	107
8.1	Microstructures	111
8.2	EC 1 tensile specimens	113
8.3	EC 2 tensile specimens	114
8.4	Effect of strain rate on SCC	115
8.5	The effect of geometry on mechanical properties.	117
8.6	Effect of stress state on strain-dry	118
8.7	Effect of stress state on strain-wet	119
8.8	Fracture surface of 304 flat samples	120
8.9	Fracture surface of 6XN flat samples	120
8.10	Environmental effect on stress	121
8.11	Environmental effect of notch on strain	122
8.12	Stress-strain curves 304L	124
8.13	Stress-strain curves 316L	124
8.14	Stress-strain curves 310S	125
8.15	Stress-strain curves 317L	125

8.16	Stress-strain curves AL-6XN	126
8.17	Surface of AL-6XN	126
8.18	Stress-strain curves for drop-potential test	127
8.19	Current in drop-potential test	127
8.20	Pit on 304 surface	128
8.21	316L SCC fracture surface	129
8.22	316L SCC cross section	130
8.23	SCC vs strain rate	132

List of Tables

2.1	Diffusivity of ions and compounds	25
2.2	Chemistries of common grades of austenitic stainless steels	39
6.1	Alloy chemistry for polarization, EC 2, and EC 3 tests	71
7.1	Composition of Fe thin films	91
8.1	Alloy chemistry for EC 1 tests	111

Chapter 1

Introduction and Motivation

1.1 The Cost of Corrosion

Since the discovery of metal, humankind has been fighting the inevitability of corrosion. Corrosion is directly responsible for loss of 3 % of the total value of goods produced and services provided in the world each year, affecting everything from cars, ships, and spacecraft, to bridges, pipelines, and the Statue of Liberty [1–3]. Because of the drain on resources attributed to corrosion, there has been tremendous effort to prevent corrosion in its various forms. Throughout history there has been extensive development of coatings, cleaning processes, acceptable environments and environmental modifications, surface modifications, and alloy chemistry. One major breakthrough in corrosion resistance was the advent of stainless steel, generally attributed to Harry Brearley in 1913 [2]. The most basic chemistry of a stainless steel is iron alloyed with chromium and carbon, though many other additions are possible. These steels have become ubiquitous in household, industrial, and military applications. There are several types of stainless steels, and optimal material/environment combination results in good performance. However, there are many situations in which the optimum combination is not achieved and a significant amount of work has been devoted to describing the thermodynamics and kinetics of stainless steel corrosion.

1.2 The Importance of, and Failure of Stainless Steels

The need for corrosion-resistant materials has led to the demand for stainless steel increasing by about 6 % each year [4]. The different types of stainless steel are generally classified by the

crystal structure of iron: ferritic, austenitic, martensitic, duplex (austenite+ferrite). This work concentrates on austenitic grades, though the distinguishing features of the different types of stainless steels are discussed further in Section 2.1.1. Austenitic stainless steels, steels with high nickel and chromium concentrations, have many advantageous properties, such as good weldability, high ductility, and, most notably, high corrosion resistance [5]. Some austenitic stainless steels even feature corrosion resistance that is higher than that of nickel alloys in certain environments [6].

The high corrosion resistance results from a thin oxide layer, the passive film, that grows on the surface of these steels. This film is able to adapt to its environment within seconds to quickly protect the underlying metal [6]. Although these passive films prevent corrosion in many environments, they are not impenetrable under all conditions. Particularly important to stainless steel degradation are localized corrosion phenomena, for example pitting, where the metal corrodes over an area only a few microns in diameter. Although pitting itself can be detrimental to part life, pits also serve as nucleation sites for stress corrosion cracking (SCC) when a component is under load. A major cause of component failures, SCC can occur in chloride containing solutions such as salt water, but can also take place in other environments, including under solid salt deposits or inert surface coatings in warm, humid conditions. In each of these cases, SCC is dependent on salt concentration, or salt film thickness and humidity, and temperature [7, 8]. Austenitic stainless steels have been known to corrode at chloride concentrations as low as 10-20 mg/L and at temperatures as low as 35 °C [9, 10]. While any corrosion is generally to be avoided, SCC is a major concern for the reliability of stainless steels in corrosive environments. Despite a significant amount of research and alloy development devoted to minimizing SCC, there is still much to be learned and improved upon.

Stress corrosion cracking in stainless steels is heavily dependent on material, environment, and stress [11]. In this study, the mechanical and environmental effects on corrosion in commercially-produced austenitic stainless steels of several chemistries were investigated. The sections below review current understanding of the alloy chemistry on passivity and corrosion resistance of stainless steels.

1.3 Corrosion Detection and Inhibition

Corrosion can be prevented through proper alloying and manufacturing processes, but in real-world applications, constraints such as cost or other material properties may limit feasible corrosion resistance of a structural alloy. In some of these cases, corrosion can be slowed through corrosion resistant coatings. Alternatively, corrosion rates can be monitored with corrosion sensors to allow for ample warning before a catastrophic failure occurs to allow for proper maintenance. Metallic thin films have been suggested as ideal materials for both of these cases, though understanding corrosion properties of metallic thin films is still preliminary [12, 13]. A deeper understanding of metallic thin film corrosion would lead to improvements in corrosion sensor technology as well as protective coatings for metal products in corrosive environments. Thin films also allow manipulation in ways that are difficult to achieve in bulk alloys, so it is possible to use thin films as analogs to study bulk metal properties.

The variables that affect thin film corrosion, such as film thickness as well as other attributes that also affect bulk corrosion, are not fully characterized. In this study, the effect of film thickness will be investigated in iron thin films. Additionally, stainless steel thin films with a continuum of alloy chemistry will be used to predict alloying effects in bulk stainless steels. The sections below review current understanding of the corrosion phenomena of iron and stainless steel thin films.

1.4 Organization of this Document

The focus of this work is the study of localized corrosion of austenitic stainless steels. Chapter 2 introduces the corrosion phenomena observed in stainless steel systems. In addition to bulk stainless steels, thin film corrosion is also investigated, both in connection to bulk stainless steel corrosion, and in its own right. Current understanding of thin film corrosion is reviewed in Section 2.2.4 and stainless steel thin films in Section 2.4.2. Chapters 3 and 4 are the objectives and hypotheses, respectively. Much of the work described herein concentrates on developing methods to observe and quantify corrosion phenomena and assess various alloy systems. Chapter 5 focuses on the equipment and instrumentation that was developed and utilized to collect the data throughout this work. In each of the experimental and results chapters, Chapters 6, 7, and 8, a section is devoted to discussing the experimental techniques

developed for the approach, followed by a collection of results and discussion of those results. Though the work completed is concluded in Chapter 9, a comprehensive understanding of the phenomena observed is far from complete. Chapter 10 suggests studies that could be utilized to continue the progress described here to understand pitting corrosion of stainless steels, thin film corrosion, and stress corrosion cracking of austenitic stainless steels.

Chapter 2

Background

There are many classes of corrosion that afflict metal systems, though corrosion processes are very alloy- and environment-specific. Austenitic stainless steels are primarily susceptible to localized corrosion, particularly pitting and stress corrosion cracking (SCC). This chapter briefly reviews general corrosion phenomena and then discusses pitting and SCC specific to austenitic stainless steels, as well as localized corrosion in iron and austenitic stainless steel thin films in chloride-containing aqueous environments.

2.1 Materials

2.1.1 Stainless Steels

Iron-based alloys are generally known for their propensity to rust, but this special class, stainless steels, are distinguished because they "stain" less. Stainless steels are iron alloys with greater than 12 wt.% Cr. Although steels with lower Cr contents are more corrosion resistant than plain carbon steels, 12 % is the empirical boundary between a steel that will rust and a steel that will not rust under ordinary conditions. Although all stainless steels grow a protective passive film, there are many different classes with vastly different properties. In ferritic stainless steels, the iron has a body centered cubic (BCC) crystal structure. These steels are used where cost, and sometimes mechanical properties, are more important than corrosion resistance. Ferritic steels are less prone to SCC than other classes of stainless steel, but are also less resistant to general corrosion. Martensitic stainless steels are hardenable using standard quench and temper processes, giving these steels the high hardness

that is required for knives and other such tools. Precipitation hardening stainless steels can be machined in the annealed condition and precipitation hardened without much distortion, making them ideal for high strength/toughness applications. In austenitic steels, the iron has a face centered cubic (FCC) crystal structure, generally due to high Ni contents. These grades are the most resistant to general/uniform corrosion in most environments and tend to be more corrosion resistant than ferritic stainless steels with the same Cr content [14]. Austenitic stainless steels are widely used in many applications, but they are the best suited for high corrosion resistant applications where strength is not a key limitation. However, austenitic stainless steels are particularly susceptible to SCC in chloride environments. Finally, duplex steels are approximately 50 % austenite and 50 % ferrite, making them stronger than austenitic steels and more corrosion resistant than ferritic steels, although the complex microstructure makes processing more difficult than the other classes, leading to unwanted phases and limited application temperature ranges [15].

The major advantage of austenitic stainless steels over the other classes is the superior corrosion resistance. Although steels of increased strength have been developed, heightening corrosion resistance has been the primary goal of research and development in this class of steels.

2.1.2 Thin Films

Thin films are a class of materials for which material properties are similar within the plane of the film, but are different in the thickness direction of the film due to mechanical, electronic, or other constraints. This can produce unique properties that cannot be established in bulk materials. In metals, such as iron or stainless steel, these thin films can be a few atomic layers to hundreds of nanometers thick, though their properties do vary with thickness [16–18]. Because these films are too thin to structurally support themselves, they require a substrate to lend mechanical support. Substrate materials span a wide range of properties, depending on the application, such as silica glass for clear, electrically insulating surfaces, doped silicon wafers that allow for some electrical condition or semiconductor applications, or metal substrates, including the same metal as the thin film itself. Sometimes functional thin films do not adhere to the ideal substrate material, so thin adhesion layers of other materials are used to ensure proper bonding. There are many techniques for forming thin films that are suited to specific materials, structures, and applications. Magnetron sputtering, used

to form metallic thin films such as those discussed in the sections below, is a plasma vapor deposition technique in which positively charged metal ions (plasma) are accelerated toward a negatively charged substrate by coulombic interactions. Magnetron sputtering can create metallic thin films with uniform thickness and homogeneous composition across the film [19].

2.2 Corrosion

2.2.1 Conditions Leading to Corrosion

Corrosion is ubiquitous throughout structural metals in nearly every imaginable environment. Corrosion is defined in the Merriam-Webster dictionary as "a gradual wearing away or alteration by a chemical or electrochemical essentially oxidizing process (as in the atmospheric rusting of iron)" [20]. Many different types of corrosion occur in metal systems; a very common example is rust, the general corrosion of iron.

Every alloy has some conditions under which it will corrode, some conditions under which no corrosion will occur, and some conditions under which corrosion may be thermodynamically possible but does not occur due to kinetic limitations or other processes that transpire. As discussed in Section 2.2.2, corrosion is dependent on environmental factors, such as applied potential, pH, and temperature, as well as other variables including solution chemistry. The solubility of an alloy's constituent metal ions in an environment is the primary factor determining whether corrosion can happen.

Most metals have multiple oxidation states, which can be stabilized by the environment. Some environments stabilize metal ions in solution while others promote compound formation, which can then either remain in solution or precipitate out. There are myriad metal ion compounds that form during corrosion, such as oxides, hydroxides, chlorides, sulfates, *etc.* If the ions or compounds are soluble in the environment, corrosion will continue until the system equilibrates; however if the compounds are insoluble, they can form a solid layer on the metal surface. An adherent permeable corrosion product layer may influence the corrosion kinetics, but will generally not greatly change the corrosion behavior, while an adherent impermeable layer is capable of inhibiting corrosion by preventing metal-environment contact. This is the passivation process that is well known in stainless steels under many conditions. Some metal-ion diffusion occurs through the passive film, but most stainless steel corrosion only occurs locally when the film ruptures.

Alloy corrosion can be a far more intricate process than corrosion of any single component. Chromium in stainless steel allows the steel to passivate under conditions where it would otherwise actively corrode. Figure 2.1 shows that even small additions can change the corrosion properties and the conditions under which an alloy will corrode [14]. Though some alloying effects are simple, alloying effects on corrosion and passivation do not always follow a simple rule of mixtures. Stainless steel can be more corrosion resistant than any of its constituents, as shown in Figure 2.2 [21].

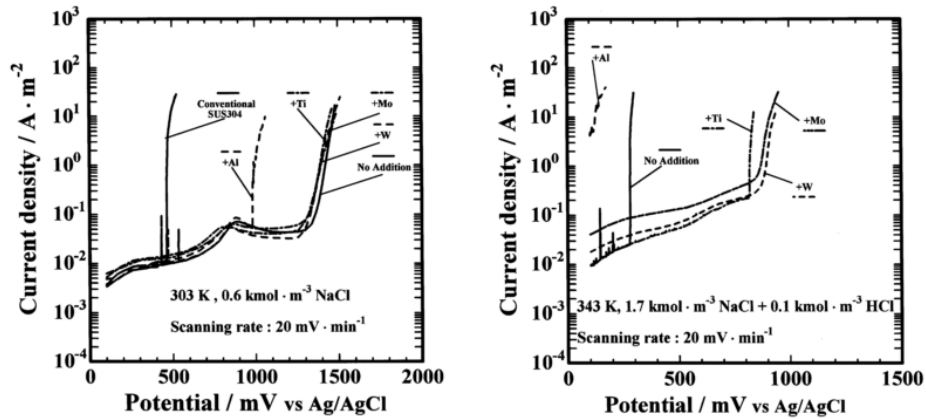


Figure 2.1: Polarization curves showing alloying effects on 304 stainless steel thin films with varying additives in different environments [14].

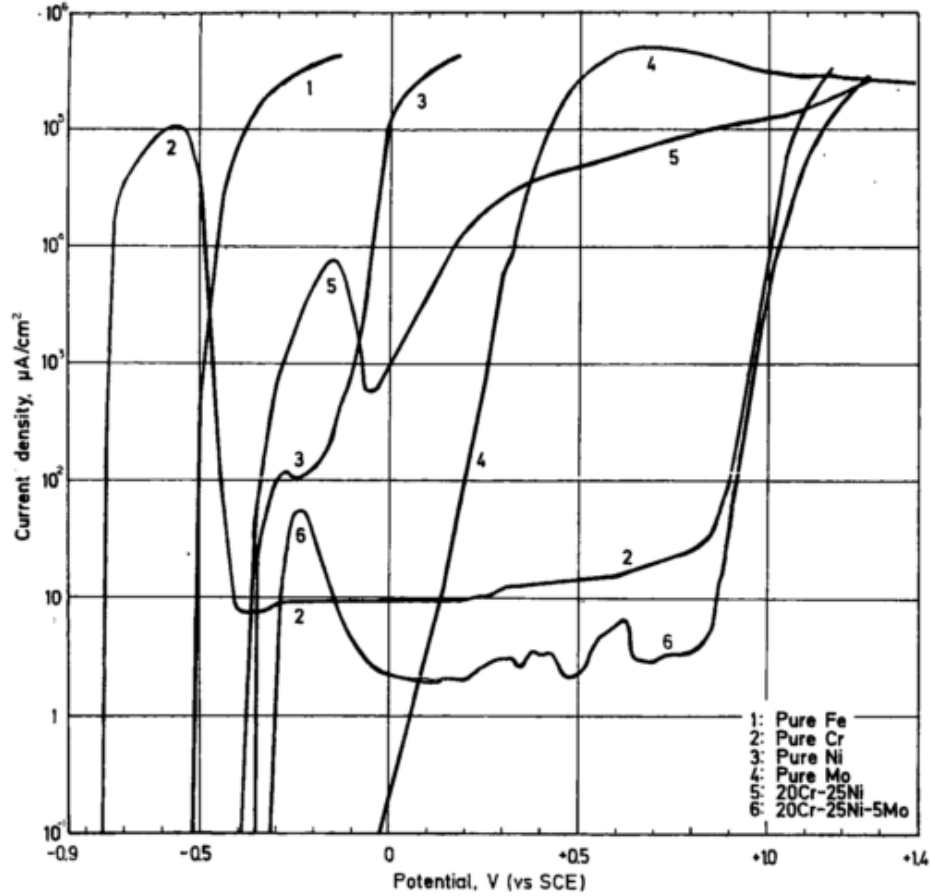
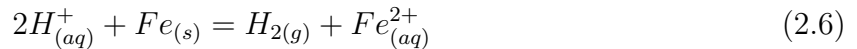
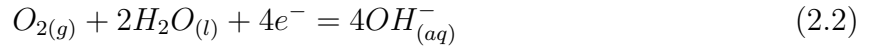


Figure 2.2: Polarization of Fe, Cr, Ni, and Mo, and stainless steel in 1 N HCl at 25 °C [21].

Microstructure can also play a large role on corrosion properties, even in a single-phase metal. Single crystal studies have shown that corrosion occurs along specific crystallographic planes, so single crystal and polycrystalline structure are likely to corrode in different manners [22]. Even in polycrystalline systems, grain size can have an impact on the corrosion mechanism in a given system. Some nanocrystalline alloys (grain size < 100 nm), such as iron and 304 stainless steel, demonstrate higher corrosion resistance in salt water than their coarser-grained counterparts, while other alloys, such as copper, are less corrosion resistant in their nanocrystalline form [23–25]. Though every metal corrodes, the corrosion process is greatly dependent on the environment, alloy chemistry, and structure.

2.2.2 General Corrosion

Corrosion is dependent on reactions between, and transport of, charged species, and is accordingly electrochemical in nature. For corrosion to proceed, there must be a cathodic reaction, such as those in Equations 2.1 and 2.2 and an anodic reaction such as in Equations 2.3, 2.4, and 2.5. Because these reactions all require unbound electrons, and free electrons are not a common occurrence without an applied potential, each of these anodic and cathodic reactions are considered half-cell reactions. When the cathodic and anodic reactions in Equations 2.1 and 2.3 are combined, they represent a full-reaction, such as shown in Equation 2.6.



The thermodynamics of these reactions are directly related to the work performed by transferring charge across a potential drop. This is expressed by Equation 2.7, where ΔG is the Gibbs free energy change (J/mol), n is the number of equivalents (charge/mol of ions), F is the Faraday constant (96,487 C/mol), and E is electric potential (V). For chemical reactions, combining Equation 2.7 with the law of mass action gives the Nernst equation, Equation 2.8, where E° is the standard reduction potential (V), R is the gas constant (8.314 J/K mol), T is temperature (K), and Q is the equilibrium constant.

$$\Delta G = -nFE \quad (2.7)$$

$$E = E^\circ - \frac{RT}{nF} \ln(Q) \quad (2.8)$$

The tendency of a metal to corrode can be quantified by the potential at which its anodic dissolution reaction becomes thermodynamically favorable ($\Delta G < 0$). This is shown in Figure 2.3 for standard conditions (metal in equilibrium with its ions at 25 °C) [3]. By convention, these are written as reduction reactions and the potentials are expressed relative to the standard hydrogen electrode. The stability of metals and their corrosion products and passive films can also be visualized through Pourbaix diagrams. Pourbaix diagrams show the stable phases that form under a range of pH and potential conditions in a given environment. It should be noted that these are equilibrium diagrams and do not account for reaction kinetics. Figure 2.4 shows an example, overlaid iron and chromium Pourbaix diagrams that approximate behavior of a stainless steel. The diagram shows the conditions where a passive oxide film can be stable.

Reaction	$E^0(\text{V vs. SHE})$	
$\text{Au}^{3+} + 3e^- \rightarrow \text{Au}$	+1.498	Noble
$\text{Pt}^{2+} + 2e^- \rightarrow \text{Pt}$	+1.18	↑
$\text{Pd}^{2+} + 2e^- \rightarrow \text{Pd}$	+0.951	
$\text{Hg}^{2+} + 2e^- \rightarrow \text{Hg}$	+0.851	
$\text{Ag}^+ + e^- \rightarrow \text{Ag}$	+0.800	
$\text{Cu}^+ + e^- \rightarrow \text{Cu}$	+0.521	
$\text{Cu}^{2+} + 2e^- \rightarrow \text{Cu}$	+0.342	
$2\text{H}^+ + 2e^- \rightarrow \text{H}_2$	0.000	
$\text{Pb}^{2+} + 2e^- \rightarrow \text{Pb}$	-0.126	
$\text{Sn}^{2+} + 2e^- \rightarrow \text{Sn}$	-0.138	
$\text{Mo}^{3+} + 3e^- \rightarrow \text{Mo}$	-0.200	
$\text{Ni}^{2+} + 2e^- \rightarrow \text{Ni}$	-0.257	
$\text{Co}^{2+} + 2e^- \rightarrow \text{Co}$	-0.28	
$\text{Cd}^{2+} + 2e^- \rightarrow \text{Cd}$	-0.403	
$\text{Fe}^{2+} + 2e^- \rightarrow \text{Fe}$	-0.447	
$\text{Ga}^{3+} + 3e^- \rightarrow \text{Ga}$	-0.549	
$\text{Ta}^{3+} + 3e^- \rightarrow \text{Ta}$	-0.6	
$\text{Cr}^{3+} + 3e^- \rightarrow \text{Cr}$	-0.744	
$\text{Zn}^{2+} + 2e^- \rightarrow \text{Zn}$	-0.762	
$\text{Nb}^{3+} + 3e^- \rightarrow \text{Nb}$	-1.100	
$\text{Mn}^{2+} + 2e^- \rightarrow \text{Mn}$	-1.185	
$\text{Zr}^{4+} + 4e^- \rightarrow \text{Zr}$	-1.45	
$\text{Hf}^{4+} + 4e^- \rightarrow \text{Hf}$	-1.55	
$\text{Ti}^{2+} + 2e^- \rightarrow \text{Ti}$	-1.630	
$\text{Al}^{3+} + 3e^- \rightarrow \text{Al}$	-1.662	
$\text{U}^{3+} + 3e^- \rightarrow \text{U}$	-1.798	
$\text{Be}^{2+} + 2e^- \rightarrow \text{Be}$	-1.847	
$\text{Mg}^{2+} + 2e^- \rightarrow \text{Mg}$	-2.372	
$\text{Na}^+ + e^- \rightarrow \text{Na}$	-2.71	
$\text{Ca}^{2+} + 2e^- \rightarrow \text{Ca}$	-2.868	
$\text{K}^+ + e^- \rightarrow \text{K}$	-2.931	↓
$\text{Li}^+ + e^- \rightarrow \text{Li}$	-3.040	Active

Figure 2.3: Standard electrode potentials of various metals. Noble metals (top) tend to be more corrosion resistant while active metals (bottom) are more likely to corrode [3].

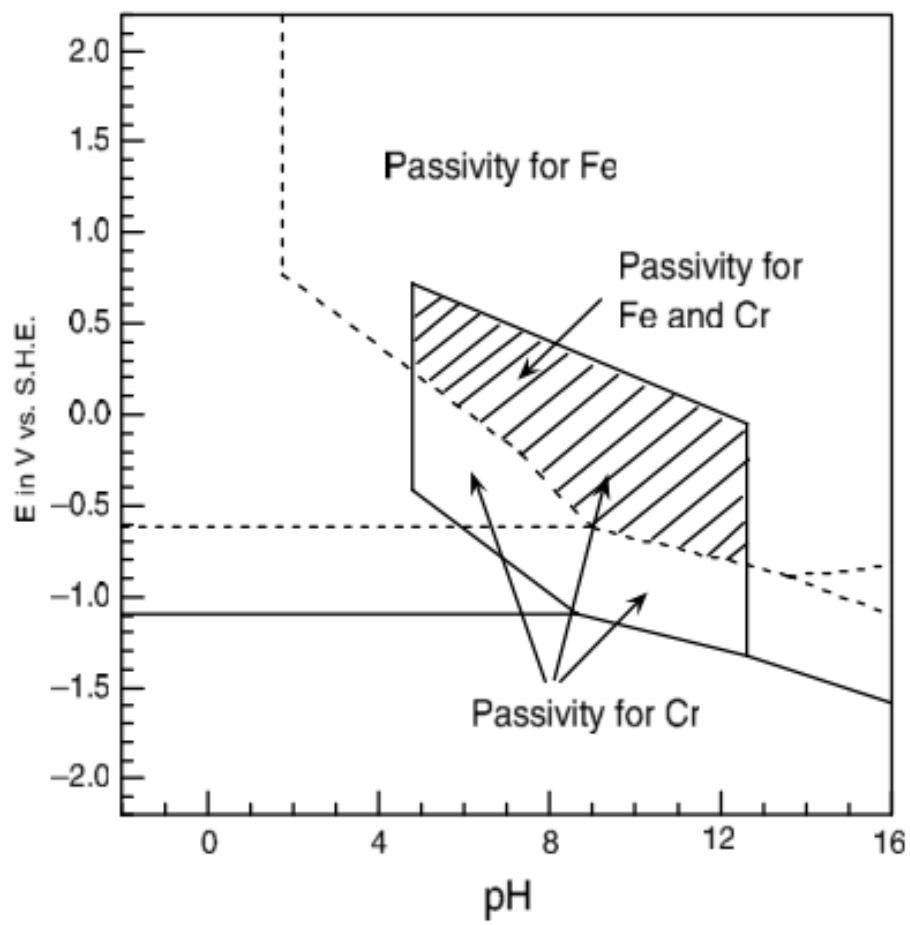


Figure 2.4: Overlaid Pourbaix diagrams of Fe and Cr at 25 °C [3].

Corrosion kinetics are also essential to describing corrosion phenomena. The mixed potential theory of corrosion dictates that each electrochemical reaction can be subdivided into individual reduction and oxidation reactions. At equilibrium, the anodic and cathodic reaction rates are equal due to conservation of charge. The corrosion potential (E_{corr}) and corrosion current (i_{corr}) can be determined by combining the anodic and cathodic reactions. This is accomplished graphically in an Evans diagram in Figure 2.5 [3].

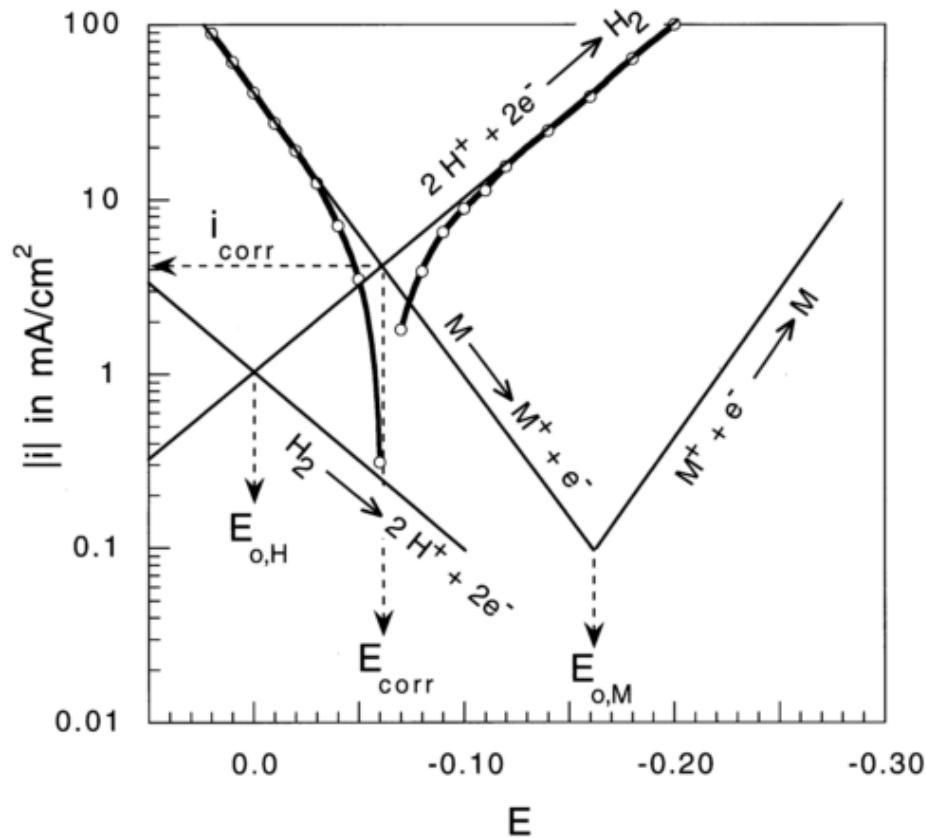


Figure 2.5: Evans diagram for hydrogen (cathodic) and a metal (anodic) in acid [3]. The straight lines represent the ideal half-cell reactions and the curved lines represent the expected measured currents due to a combination of all reactions.

When the chemical reactions are rate controlling, the kinetics can be quantified with the Butler-Volmer equation, Equation 2.9, where i is the current density (A/m^2), i_0 is the exchange current density (A/m^2), β is the charge transfer coefficient, and η is the overpotential. The overpotential is the distance of the applied potential from the equilibrium potential for a given reaction, Equation 2.10, which acts as the thermodynamic driving force.

$$i = i_0 \left[\exp\left(\frac{-n\beta F\eta}{RT}\right) - \exp\left(\frac{n(1-\beta)F\eta}{RT}\right) \right] \quad (2.9)$$

$$\eta = E - E_{eq} \quad (2.10)$$

When the solution near the anode becomes saturated with metal ions, such as within a pit or a stagnant solution, ion transport becomes the kinetic limiting factor. Diffusion controlled kinetics can be modeled with Fick's first law, Equation 2.11, where J is flux (mol/m²s), c is species concentration (mol/m³), D is the diffusion coefficient (m²/s), and x is position (m). Corrosion on a metal surface or in a small pit can be modeled with reaction controlled kinetics, but diffusion controlled kinetics become more substantial as the pit grows deeper.

$$J = -D \frac{\partial c}{\partial x} \quad (2.11)$$

2.2.3 Localized Corrosion

Though a given metal may be susceptible to corrosion, a protective coating may make the metal effectively immune to corrosion while the coating is intact. If the protective coating fails, due to abrasion, mechanical rupture, chemical failure, *etc.*, the underlying metal will then be in contact with the environment and hence vulnerable to corrosion. The basic corrosion processes and thermodynamics that occur are the same as in the case of general corrosion, yet the conditions of localized corrosion are sufficiently different that localized corrosion is considered distinct from general corrosion.

Stainless steels are susceptible to localized corrosion because the passive film, which prevents general corrosion, can fail and allow the environment to contact the bare metal surface in a small, localized region. There are two common types of localized corrosion: crevice corrosion and pitting. Crevice corrosion occurs when there is some confined area that diminishes diffusion to the bulk solution, such as the corner of a chamber, interface between parts, edge of a protective coating, or under a salt deposit [26]. Corrosion occurs because the confined environment diverges from the bulk solution, becoming more concentrated and, after corrosion begins, more acidic [27, 28]. Anionic impurities, such as Cl⁻, tend to congregate in diffusion limited occluded regions, which leads to corrosion [29].

Even without a macroscopic crevice, stainless steels are still susceptible to pitting, a similar phenomenon to crevice corrosion, but one that occurs on the bulk surface [28]. Although

some metals may be impervious to corrosion under certain circumstances, every passive metal is susceptible to pitting [30, 31].

Crevice corrosion and pitting can both occur in a metal without any detrimental stress, although stress can increase corrosion rates, while stress corrosion cracking is a form of localized corrosion that only occurs under some stress, either external or internal. Stress corrosion cracks typically grow from pits or crevices, but are a distinct type of localized corrosion and can also occur directly on the surface of a metal [32]. The defining factor of SCC is the brittle failure of an otherwise ductile material due to environmental interactions. There are multiple mechanisms of SCC that vary widely between alloy systems and environments.

2.2.4 Thin Film Corrosion

Thin films can have vastly different corrosion properties from their bulk counterparts [13, 14, 23–25, 33]. The differing corrosion properties of thin films have many possible causes, including divergence from bulk structure, secondary phases, resistivity, and grain size. Nanocrystalline Fe has been shown to have lower current densities than coarser-grained Fe, and can even passivate where coarse-grained Fe actively corrodes [23]. Similarly, nanocrystalline 304 stainless steel passivates faster and remains passive at higher potentials than its coarse-grained counterpart [24]. However, not all alloy systems benefit from a nanocrystalline surface, such as Cu, where the nanocrystalline thin film corrodes faster than bulk Cu [25]. The primary dissimilarities between corrosion in bulk metals and their thin film counterparts have been attributed to grain size and homogenized chemistry [12, 25, 34]. This has been supported by the effects of surface treatments on bulk metals, such as laser remelting, that form homogeneous nanocrystalline layers that have been shown in tool steels and stainless steels to act similarly to thin films [12]. The higher grain boundary area of nanocrystalline films allows for faster diffusion, which is expected to increase corrosion rates in actively corroding metals and decrease corrosion in passive metals [25, 34]. Homogeneous composition resulting in fewer second-phase particles is expected to decrease localized corrosion [14, 33].

Though bulk Fe normally actively corrodes in salt water, Fe thin films can actually be more corrosion resistant in salt water than bulk 304 stainless steel [23]. Figure 2.6 shows that 300 nm Fe thin films have corrosion potentials more anodic than bulk Fe, and even demonstrate passivation behavior [23]. The difference between the thin film behaviors is likely due to varying defects in the films from their differing formation processes. Defects

on thin film surfaces can decrease corrosion resistance, shown in Figure 2.7 [13]. Smoother substrates increase the corrosion potential by limiting the number of surface defects on the thin film. The rougher films form active sites promote corrosion, but each of the thin films passivates while the bulk steel continues to actively corrode [13]. Though the impact of surface defects is established, the mechanism by which iron and steel thin films passivate while their bulk counterparts actively corrode is not well understood.

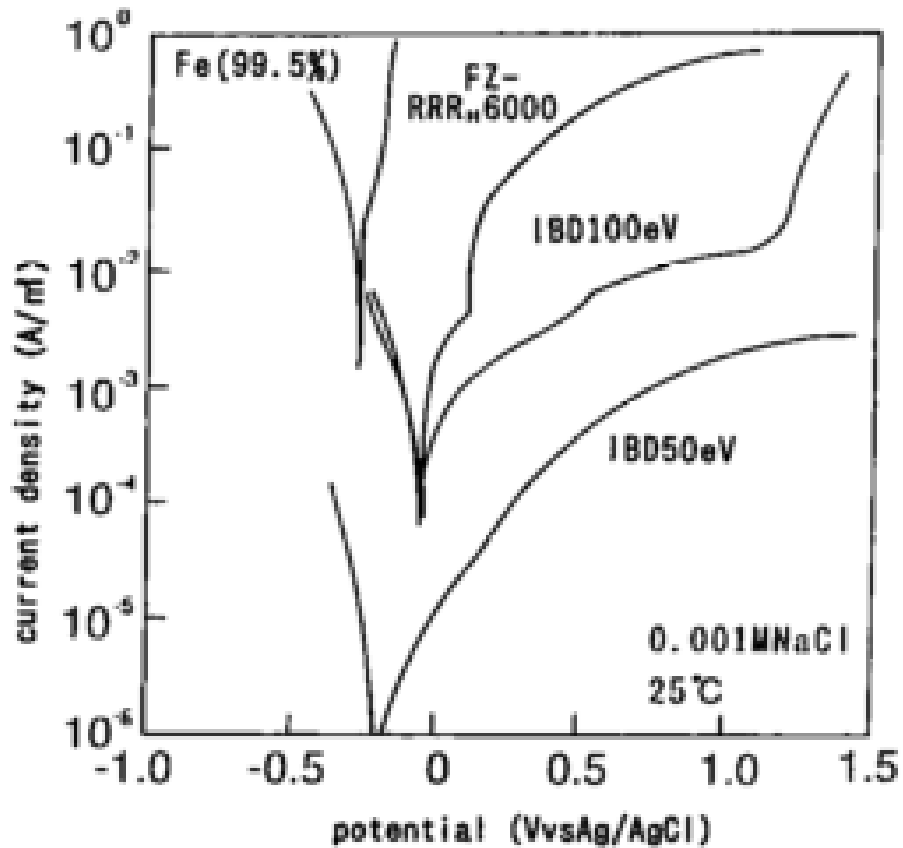


Figure 2.6: Polarization curve of bulk Fe, purified Fe sheet (FZ-RRR_H6000), and two 300 nm Fe thin films (IBD100eV and IBD50eV) in 0.001 M NaCl at 25 °C [23]. More noble metals have a higher E_{corr} . Slower corrosion results in lower i_{corr} , so FZ-RRR_H6000 and IBD100eV are the most noble, while IBD50eV undergoes the least corrosion if no potential is applied.

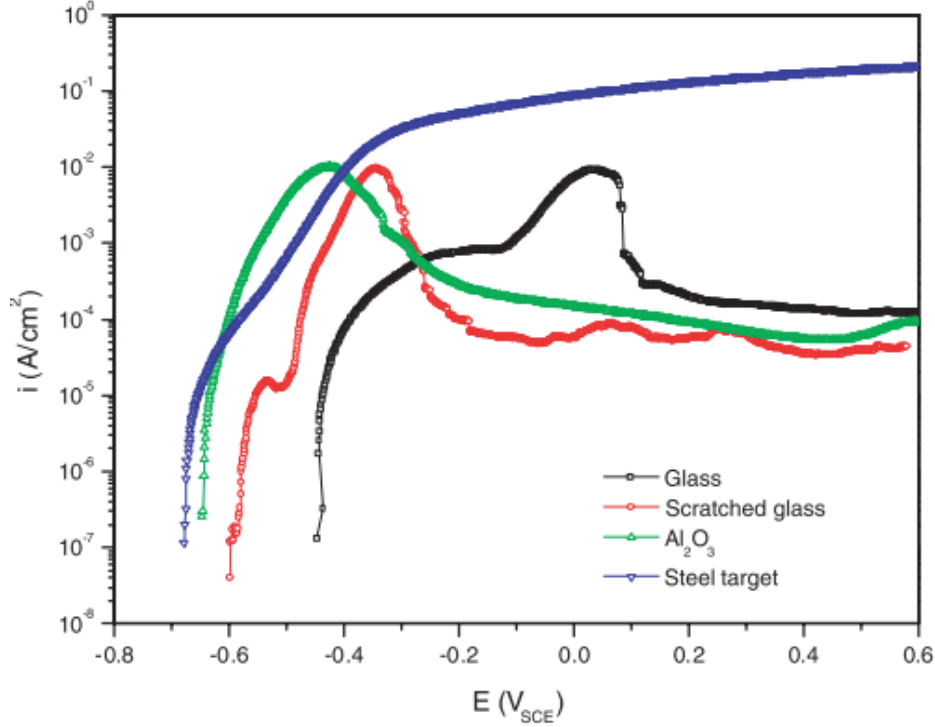


Figure 2.7: Polarization curve of bulk carbon steel and 600 nm carbon steel thin films on various substrates in 3.5 wt.% NaCl at 25 °C [13].

Austenitic stainless steel thin films also show improved corrosion resistance over bulk steels, though there are some key differences [13, 14, 19, 33, 35, 36]. In bulk stainless steels, austenitic steels are more corrosion resistant than ferritic steels with the same Cr content; however thin film metastable austenitic stainless steels, such as 304 and 309, have been shown to be primarily ferritic and polycrystalline with no texture [13, 14, 19, 36]. Sputtered 304 nanocrystalline films contain about 6 % austenite with the remainder ferrite [37]. Between 477 °C and 677 °C, the ferrite can be annealed to austenite, though this temperature range also leads to sensitization, so any advantage from annealing would likely be countered by Cr depletion [37]. Deposited films are thought to be ferritic because of rapid quenching, causing thickness independent high residual stresses on the order of 1 GPa [37]. Stainless thin films maintain their passivity at higher potentials than their bulk counterparts, shown in Figure 2.8 [24, 36]. The increase in corrosion resistance is due to a higher Cr/Fe ratio in the passive film, faster passivation, and homogeneous composition [19, 33, 38]. The higher Cr/Fe ratio and faster passivation are possible because of the high grain boundary area, increasing diffusion rates within the metal. Faster diffusion leads

to quicker dissolution of Fe during the passivation process, so the remaining passive film contains more Cr. The large number of defects associated with smaller grains increases the number of passive film nucleation sites, shown in Figure 2.9, increasing the passivation rate and forming a more compact and resistant film with fewer harmful anions (Cl^-) dissolved in the oxide [33, 34, 36]. The more compact nature of the nanocrystalline film also increases the mechanical toughness and decreases ion transport through the oxide [36, 39]. Nanocrystalline stainless steels, particularly sputtered thin films, have improved corrosion resistance due to their homogeneous composition [33]. Figure 2.10 shows that films produced under higher vacuums are more corrosion resistant, ostensibly because of residual water reactions in low vacuums forming oxides during sputtering [14, 40]. Because of the lack of second phase inclusions compared to coarse-cast material, metastable pitting on thin films can be too small to observe, while similar bulk metal can form obvious metastable pits [33]. Metastable pitting on thin films is faster, and more frequent than metastable pitting on bulk metals because of the high number of surface defects [35]. Though stainless steel thin films have more metastable pit nucleation sites than coarse-cast steel, the evolution of stable nucleation is a slower process on thin films [35].

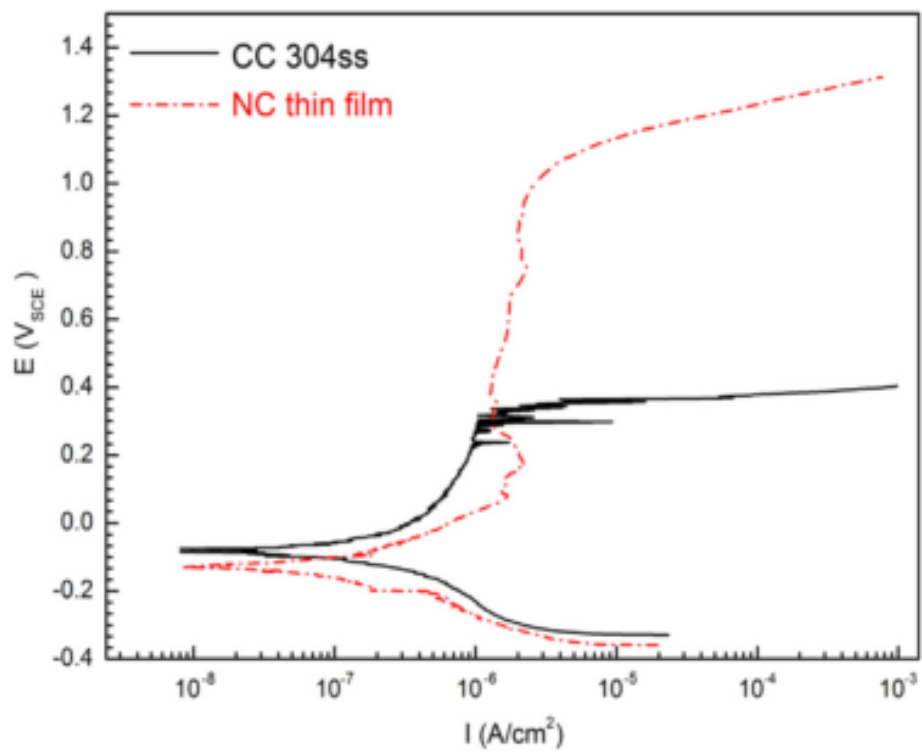


Figure 2.8: Polarization curve of bulk 304 and 150 nm 304 thin films in 3.5 wt.% NaCl at 25 °C [24].

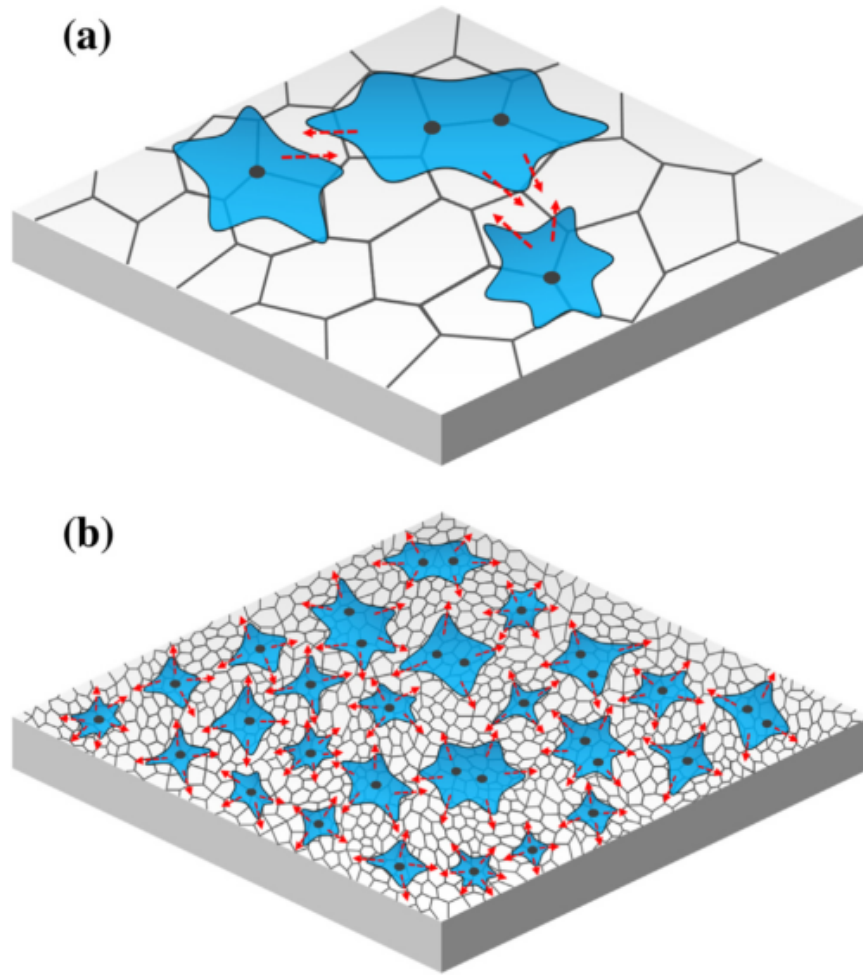


Figure 2.9: Schematic showing the increased passive film coverage of nanocrystalline metals compared to coarse-grained metals [33].

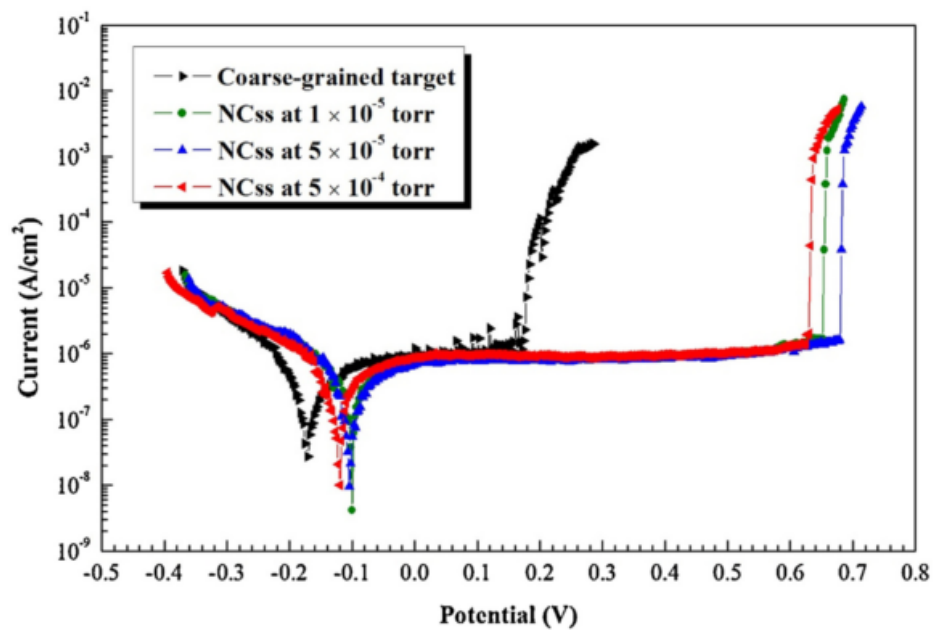


Figure 2.10: Polarization curve of bulk 304 and 100-200 nm 304 thin films sputtered under different conditions in 3.5 wt.% NaCl at 30 °C [40].

2.3 Pit Solution Chemistry

Pitting is a form of localized corrosion that can occur on an otherwise flat and passive metal surface, even under no mechanical loads. Pits tend to be round, though they can be faceted, and grow straight into the metal normal to the surface [41]. Small pits can be hemispherical but pit growth is usually accompanied by an increase in aspect ratio (depth to diameter) [42]. The occluded nature of pit interiors concentrates the localized environment which thus become harsher than the bulk environment at the surface of the metal. Pits can both initiate and inhibit SCC, making pitting a critical process in the SCC lifecycle.

2.3.1 Aqueous Chemistry

Due to the complex chemical interactions that occur during localized corrosion, it is important to consider the properties of the solvent and solutes that constitute the environment. The effect of cation species on anion activity can affect the potency of the overall environment, even if there are no direct metal-cation interactions; different cations can give rise to varying chloride content. Saturated chloride concentration does not change much with temperature for most compounds, as shown in Figure 2.11, though there are some exceptions such as FeCl_3 [43]. A solution with Fe^{2+} or Ni^{2+} cations can have a much higher chloride concentration than a simple NaCl solution. Chloride ions decrease the stability of stainless steel passive films, but their effect is redoubled because Cl^- presence increases the activity of H^+ , thus decreasing the pH and creating an even harsher environment [44].

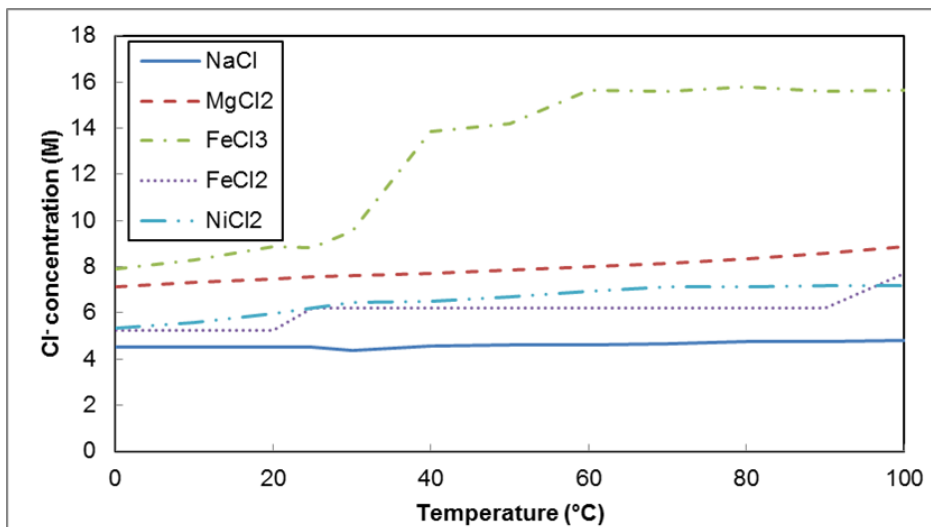


Figure 2.11: Chloride concentrations for various saturated salt solutions as a function of temperature [43].

Though chloride concentration is considered the major corrosive factor in relevant environments, the salinity of the solution can have other effects as well, such as decreasing the solubility of dissolved CO_2 , which can lead to carbonic acid formation [45].

While there are many potentially harmful ions and compounds that can be found in water, their presence is irrelevant unless they are in close proximity to the metal surface. The local environment is not always homogeneous; ions can evolve from distinct points along the metal surface due to metal inhomogeneities, ions can enter the environment far from the metal surface, or an occluded region in or near the metal surface can prevent fast diffusion to the bulk solution. Iron ion corrosion products (Fe^{2+} , $\text{Fe}(\text{OH})^+$, $\text{Fe}(\text{OH})_2$) all have similar diffusivities in water, while halides (Cl^-) and their saline counter-ions (Na^+) have about double the diffusivity of the iron compounds, and H^+ diffusivity is an order of magnitude higher still, shown in Table 2.1 [46]. All compounds in the solution will undergo some diffusion, but the dissimilar diffusion rates between different ion varieties can result in increasing the magnitude of local inhomogeneities, further increasing environmental effects. Thus the chemistry within the occluded regions of localized corrosion pits, crevices, or cracks becomes vastly more concentrated than the bulk solution.

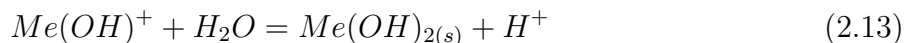
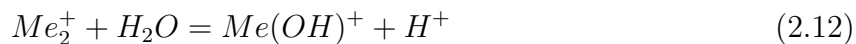
Species	Na ⁺	Cl ⁻	H ⁺	OH ⁻	Fe ²⁺	FeOH ⁺	Fe(OH) ₂
Charge (z)	+1	-1	+1	-1	+2	+1	0
Diffusion Coefficient ($\times 10^{-9}$ m ² /s)	1.995	1.995	9.976	0.9976	0.9976	0.9976	0.9976

Table 2.1: Diffusion coefficients of ions and ion compounds in water at 298 K [46].

2.3.2 Aqueous Chemistry Within a Pit

Bulk solution chemistry governs the initiation of localized corrosion, but the propagation stage is determined by the chemistry within the occluded region. The chemistry within a pit can vary greatly from the bulk solution chemistry because of the limited diffusion between the occluded region and the bulk solution, resulting in a highly concentrated solution [46]. Though diffusion limitation plays a major role in pit solution chemistry, metal-solution and aqueous reactions greatly influence the evolution of the local environment.

The corrosion reactions in Section 2.2.2 are examples of those responsible for leaching metal ions into the solution, however the metal ions continue to react with their environment. In solution, metal hydrolysis, Equation 2.12, yields metal ion compounds and H⁺, thus decreasing the pH of the solution. The resulting ion compounds can be further hydrolyzed, Equation 2.13, to form solid precipitates and further decrease the pH. While this does occur in bulk solutions, the change in pH at the metal surface is negligible due to the fast diffusion of H⁺ away from the metal. In contrast, when hydrolysis occurs in the occluded cell of localized corrosion, the H⁺ does not diffuse into the bulk solution as quickly due to the diffusion barrier and the stabilization by the other ions in solution, resulting in a severe drop in pH in the local environment [47, 48].



In addition to the species that are formed at the pit base, ions from the bulk environment are also drawn into and held within the localized pit environment. The high concentration of cations formed from metal dissolution and hydrolysis creates a coulombic force that attracts negatively charged chloride ions into the pit to maintain electric neutrality [9, 30, 44]. As chloride anions migrate into the pit, the H⁺ activity increases; the accompanying drop in

pH results in increased metal dissolution, causing an autocatalytic positive feedback [9, 44]. Once a pit, or other form of localized corrosion, is large enough to sustain stable growth, the localized environment becomes saturated with metal ions, around 5 M, and can precipitate hydroxide and chloride compounds, contains chloride concentrations as high as 12 M, and has a pH as low as 0 [7, 26, 32, 44, 49, 50]. The solution becomes supersaturated with metal ions, leading to the precipitation of chloride salts (FeCl_2 , CrCl_3 , *etc.*) along the pit walls [41, 50, 51]. The salt film acts as a resistive layer as discussed in 2.2.3. Few metals exist that can withstand this harsh environment, so even highly corrosion resistant and passivated materials can be susceptible to localized corrosion.

2.4 Passivity and Corrosion of Stainless Steels

2.4.1 Localized Corrosion of Stainless Steels

Stainless steel's defense against corrosion lies in a passive 1-3 nm thick chromium rich oxide film that forms when exposed to air or an oxidizing environment [6, 52–54]. As long as the passive film remains intact, it will protect the underlying metal from further exposure to the environment. Because of the dissimilar conditions at the metal-oxide interface and the oxide-environment interface of the passive film, it forms layers of different compositions [39, 52, 53]. The passive film in neutral and acidic environments is composed of layers as shown in Figure 2.12 [6, 52]. The metal immediately adjacent to the passive film is enriched in nickel, while the passive film itself consists of a chromium-rich oxide inner layer and an iron-rich hydroxide outer layer. The nickel rich layer is formed because of diffusion of iron and chromium out of the bulk metal into the oxide. The hydroxide outer layer is due to interactions between water and the oxide. The thickness, composition, and strength of each of these layers is dependent on overall alloy composition and environment [39, 52, 53].

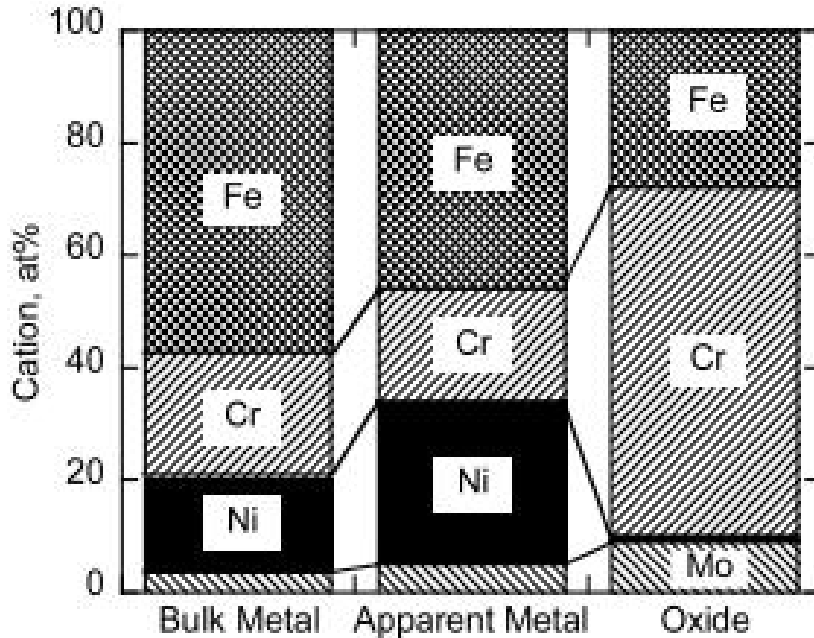


Figure 2.12: Cation concentrations in the bulk metal compared to the passive film [6].

In spite of every attempt to prevent localized corrosion and SCC in stainless steels and to tailor alloy chemistries for specific service environments, even the most advanced alloys still degrade in harsh environments. There is no evidence that any alloy or surface treatment is completely corrosion resistant [30]. However, corrosion can occur within hours or days after contact with a harsh environment or be prolonged by years through treatment and alloying [30, 31]. There are three main stages of localized corrosion development, each of which can be modified through alloy chemistry and processing: nucleation, metastable growth, and stable growth.

Initiation of localized corrosion requires a breakdown of the protective passive film. One model for this process has been devised by considering point defect transport through the oxide. Metal cation dissolution into the environment results in film degradation, while film growth is controlled by anion transport to the oxide-metal interface [31, 47, 49, 55, 56]. The directions of ion and vacancy diffusions are shown in Figure 2.13. The dissimilarity between cation diffusion rates within the oxide film and bulk metal allows vacancies to congregate on the metal-oxide interface [30]. If the concentration of vacancies at the metal-oxide interface grows large enough, the vacancies coalesce into voids, locally detaching the passive film from the bulk metal. If the oxide and metal are detached, the oxide no longer has a

supply of cations, thus any cation dissolution into the corrosive fluid results in a net decrease in thickness of the passive film [30, 31, 48]. Cation vacancies are in equilibrium at the oxide interfaces, and oxide films support fast diffusion due to high point defect concentrations, especially at grain boundaries and other local inhomogeneities. Consequently, as long as there is ample available electrolyte, metal-oxide interface cation transport determines whether localized corrosion will occur [6, 31, 49, 56, 57]. Compressive strain in the oxide lattice slows cation diffusion, retarding vacancy coalescence, while increasing anion diffusion, affording oxide growth [57]. If cation flux through the oxide is slower than between the metal and oxide, vacancies will not coalesce and pitting will not occur. Conversely, tensile strain increases cation diffusion and accelerates void coalescence and passive film breakdown. Detrimental tensile strains can originate from external macroscopic stresses (tensile loads), internal stresses (heat affected zones of welds), or steric stresses (absorbed Cl^-).

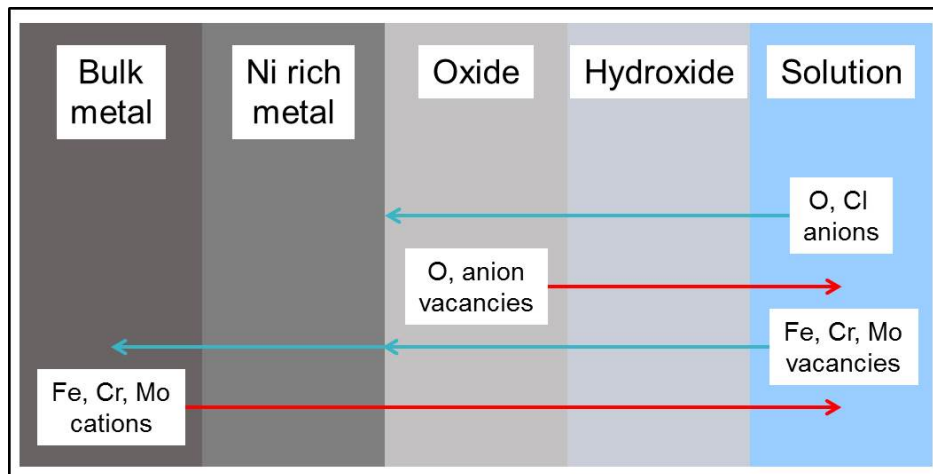


Figure 2.13: Diffusion of ions and vacancies through passive film.

Another possible localized corrosion initiation mechanism is the film thinning model. Adsorbed chloride ions disrupt the passive film and increase the dissolution rate of metal cations, resulting in localized thinning. Chloride ions adsorb preferentially to fast-path diffusion regions, so corrosion occurs primarily in high-defect regions such as grain boundaries and metal-inclusion interfaces. The film decreases in thickness until bare metal is exposed, shown in Figure 2.14 [3].

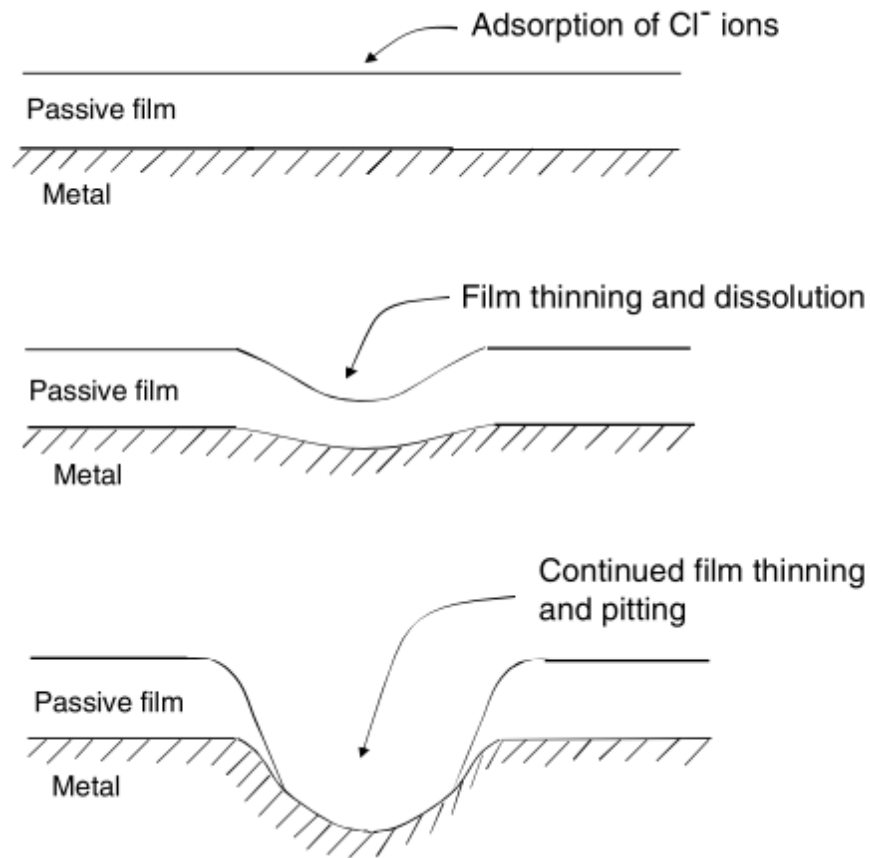


Figure 2.14: Chloride adsorption increases passive film dissolution and exposes bare metal [3].

The film rupture model relies on mechanical failure of the passive film. There are always stresses along the metal-oxide interface caused by the mismatched lattice size of the metal and oxide. Two mechanisms of film rupture may occur due in chloride solutions. Absorbed chloride ions decrease the mechanical strength of the passive film by disrupting the network covalent bonds, allowing residual stresses between the metal and oxide to fracture the film. Alternatively, steric strain caused by the large chloride ions within the oxide causes a mechanical rupture, exposing the bare metal to the environment, shown in Figure 2.15 [3].

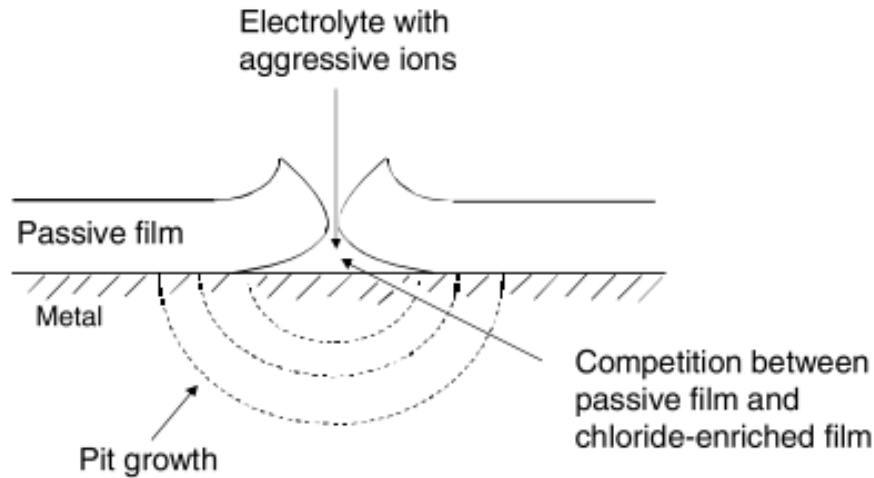


Figure 2.15: Chloride absorption causes passive film fracture and exposes bare metal [3].

The stability of a passive film can be described by its pitting potential (more positive potential), which is the electrical driving force required to degrade the film, and corrosion potential (more negative potential), which is the electrical potential at which the cathodic and anodic reactions are in equilibrium. Consequently, an applied voltage can accelerate (held above pitting potential) or halt pit growth (held below pitting potential) [49, 52, 58]. Pitting is an anodic reaction where the pit interior is the anode and the passive surface of the metal is the cathode [30, 41, 59, 60]. The current passing through the metal is directly proportional to the number of metal ions dissolved into the electrolyte, and does not vary significantly with potential within the passive region [30]. Pitting potential is determined by material, environment, and load. Chromium, molybdenum, and nitrogen increase the pitting potential, while nickel has little effect because it is not a significant constituent of the oxide [52, 61]. Meanwhile, chloride ions decrease the pitting potential because they are detrimental to the stability of the passive film [58]. Pitting potential also decreases with tensile stress on the oxide film [58]. A metal polarized to its pitting potential will pit spontaneously, but localized corrosion can occur in electrically neutral environments as well.

Oxides and sulfides, particularly manganese sulfide, can disrupt the passive film, dissolve preferentially, and form pit nucleation sites through mechanisms such as that shown in Figure 2.16 [48]. To decrease pitting and film failure due to inclusion particles, advanced steels tend to be "clean" (low in sulfur and other inclusion causing elements). In very clean alloys, such as sputtered stainless steel thin films, the small number and size of inclusions increases the

corrosion resistance without impacting the passive current density compared to less clean specimens [24, 33, 50]. In such steels, no MnS inclusions are observed, so pitting nucleates at metal-oxide inclusion interfaces, which break down at higher pitting potentials [24]. In extremely clean steels with no ceramic inclusions, even inhomogeneities of clusters only a few atoms large can decrease the stability of the passive film enough to nucleate pits [50].

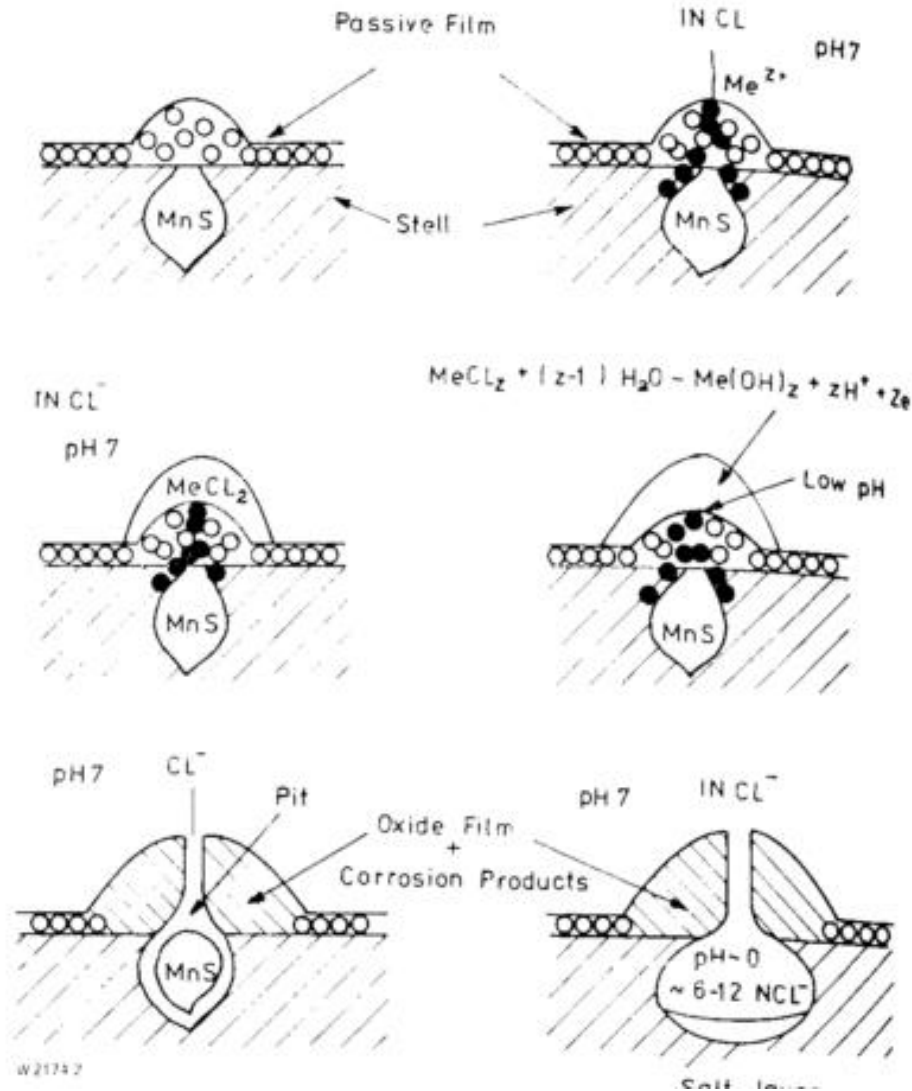


Figure 2.16: Mechanism of pit nucleation at MnS inclusion particles in neutral chloride solutions [48].

Defects in the passive film, such as at grain boundaries, slip boundaries, coherent twins, inclusions, and strain hardened areas, promote pit nucleation [31, 48, 62–64]. For a given

environment, there is a finite number of pit nucleation sites, though harsher environments allow for pit nucleation at less favorable sites [65, 66]. The nucleation process at any of these sites is very fast, creating small, metastable pits [49, 53]. Further pit growth is then slow, with current densities as low as 0.1 A/cm^2 , and metastable until the pit is large enough to support a stable local environment and slow diffusion between the pit base and bulk solution [49, 50, 53]. During metastable pit growth, pits nucleate, grow, then die, leaving small inhomogeneities on the surface. Once a metastable pit has grown deep enough to form an occluded region, generally within the micron length range, the localized environment can begin to concentrate due to the diffusion limitation and stable pitting can occur [50].

Stable pit interiors are extremely acidic and saturated with metal salts, generating a self catalyzed occluded cell [7, 9, 26, 49]. When metal dissolution occurs, positively charged metal ions are released into the occluded cell. To maintain electric neutrality, chloride ions migrate towards the growing pit, decreasing the pH within the pit, and further leeching the metal [9, 28, 30, 47, 48]. Pit walls are not passivated, so metal within pit actively dissolves at current densities around 7 A/cm^2 [50]. Active dissolution at the anode occurs at a lower potential than cathodic reaction on the metal surface, so Ohm's law implies some ohmic difference (IR drop) between the base of the pit and metal surface. This IR drop is possible due to the resistivity of the solution, any pit cover that remains over the pit mouth, as well as any salt film that precipitates due to the high concentration of metal and chloride ions [41, 50, 60]. Once an occluded cell is formed, stable pit growth rate can be suppressed through repassivation of the exposed metal, but can also be increased by tensile stress in the metal or at the oxide-metal interface [62, 67, 68].

Pits can propagate through steel components to cause failure, but more often, part failure is due to propagation of SCC from within pits. SCC will initiate at pits larger than some critical size, therefore decreasing the number and size of pits decreases the likelihood of SCC initiation [48, 64]. However, stress corrosion cracks are not always tied to pits; SCC can also nucleate at slip steps, grain boundaries, inclusion boundaries, *etc.* [59, 69]. Similar to pitting and crevice corrosion, SCC is always preceded by a rupture in the passive film [31, 54, 58]. Although surface reactivity is not different for plastically deformed metal, SCC can form during deformation upon reaching the 0.2 % yield stress of the bulk metal [70, 71].

Because SCC is a corrosion process, cracking is dependent on passivation rate; fast repassivation can stunt SCC growth [72]. Due to the kinetic limitation of corrosion processes, SCC and pitting are somewhat competitive, so as one corrosion mechanism escalates, the oppos-

ing process diminishes [73, 74]. If anodic dissolution is faster than crack growth rate, pitting will dominate, and conversely, if crack growth rate is faster than pit propagation rate, SCC will dominate [74]. Chloride induced SCC is often transgranular at the surface due to dissolution along slip planes, but cracks can progress to intergranular paths, especially when a crack nucleates from a pit [59, 75, 76]. Sensitization causes intergranular cracking due to the depleted chromium content along grain boundaries. Unlike pitting, SCC requires stress on the metal, therefore SCC growth rate is also dependent on material strength and crack tip strain rate [77].

2.4.2 Localized Corrosion of Stainless Steel Thin Films

Corrosion of thin films is fundamentally the same as corrosion of bulk metals, though there are some crucial differences. As discussed in section 2.2.4, the passive film on nanocrystalline metal has more defects, but is also quicker to repassivate than on bulk metal. For this reason, metastable pitting events are more frequent than on bulk metal [24]. Thin film metastable current transients are also shorter and smaller than on bulk metal, but the shape is similar, signifying a similar repassivation mechanism [24]. Correspondingly, pit radii tend to be smaller in thin films, shown in Figure 2.17 [24, 38]. Pits in thin films have also been shown to be shallower than in bulk stainless steels, shown in Figure 2.18, though this observation could be skewed by the unknown extent of undercutting [24]. Similar to bulk stainless steel, thin film pits are diffusion controlled, though thin films have significantly higher current densities, around $80 A/cm^2$, because of their smaller diffusion barriers [50].

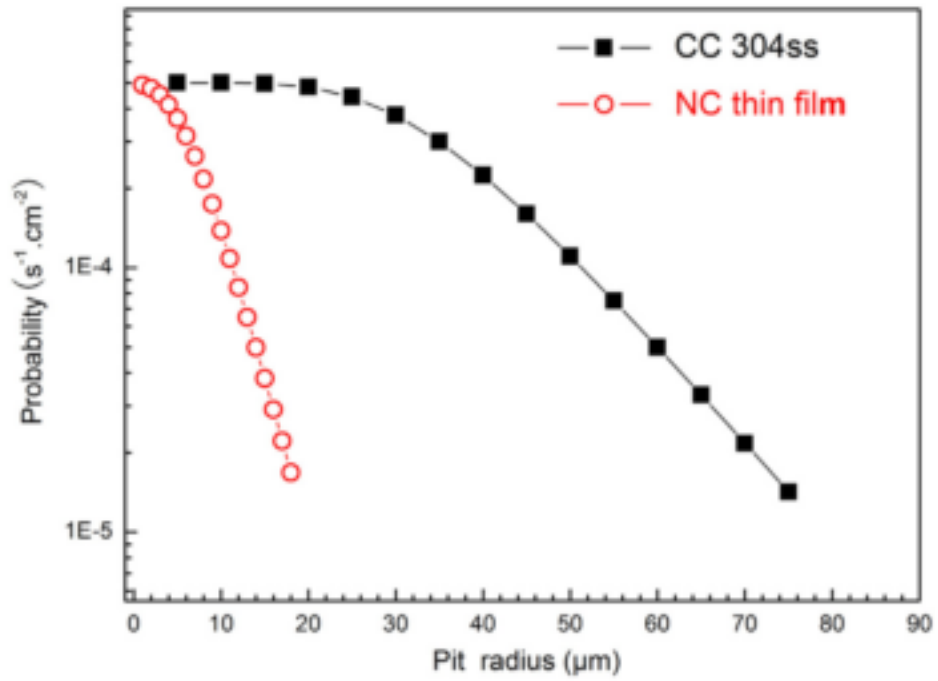


Figure 2.17: Calculated frequency of 304 stainless steel thin film (nanocrystalline) and bulk (coarse-cast) pits of varying radius [24].

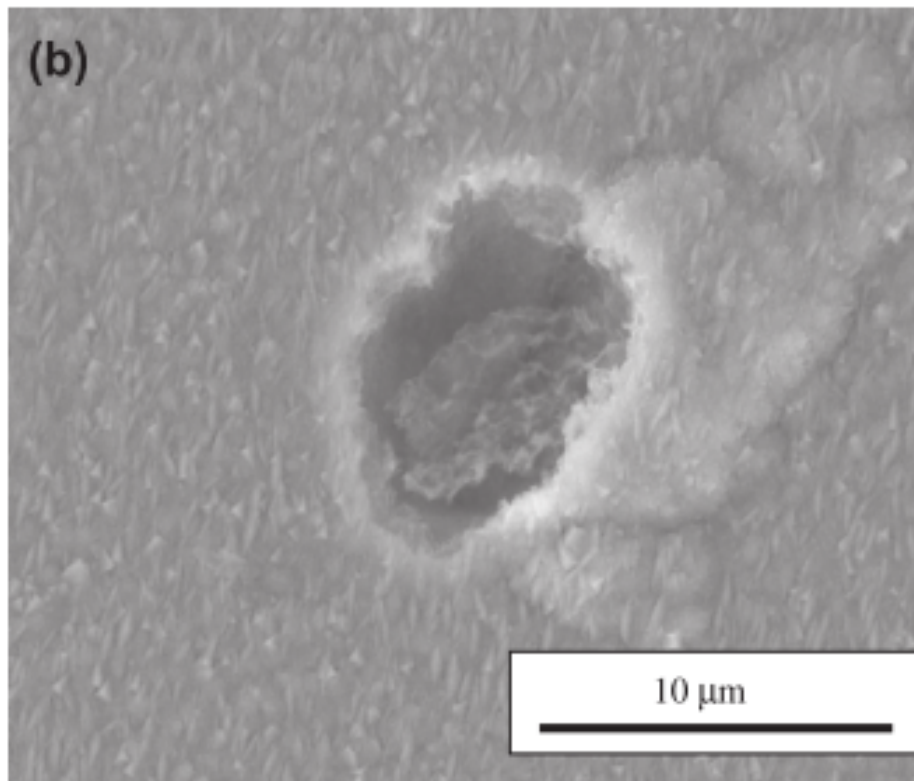
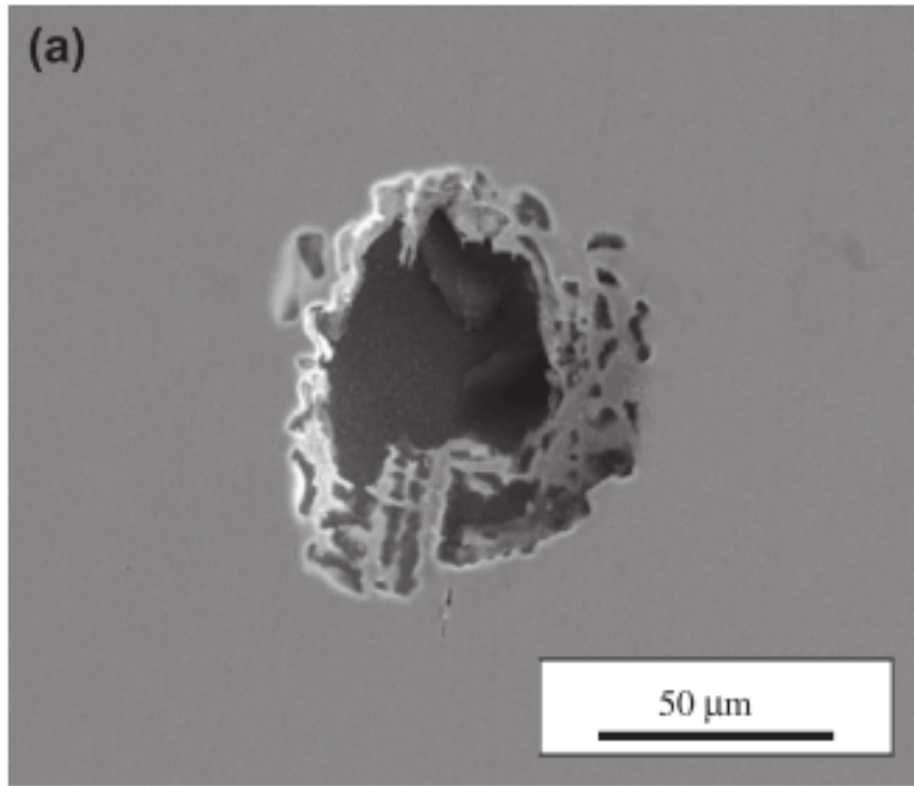


Figure 2.18: Micrographs of pits in 304 stainless steel a. bulk metal and b. thin film [24].

The initiation and early growth of stainless steel thin film pits are similar in mechanism and morphology to bulk pits. Thin films even demonstrate similar undercutting, with lacy pit covers of oxide and unreacted metal [33, 39, 50]. However, pits that grow into thin films are constrained by the inert substrate on which the metal thin film resides. Large pits grown on thin films exhibit a unique morphology with concentric circles radiating from the center of the pit, shown in Figure 2.19 [33]. The radial pattern of the holes of the pit cover are evenly spaced, and the concentric ring spacing is correlated to the depth of the pit [33].

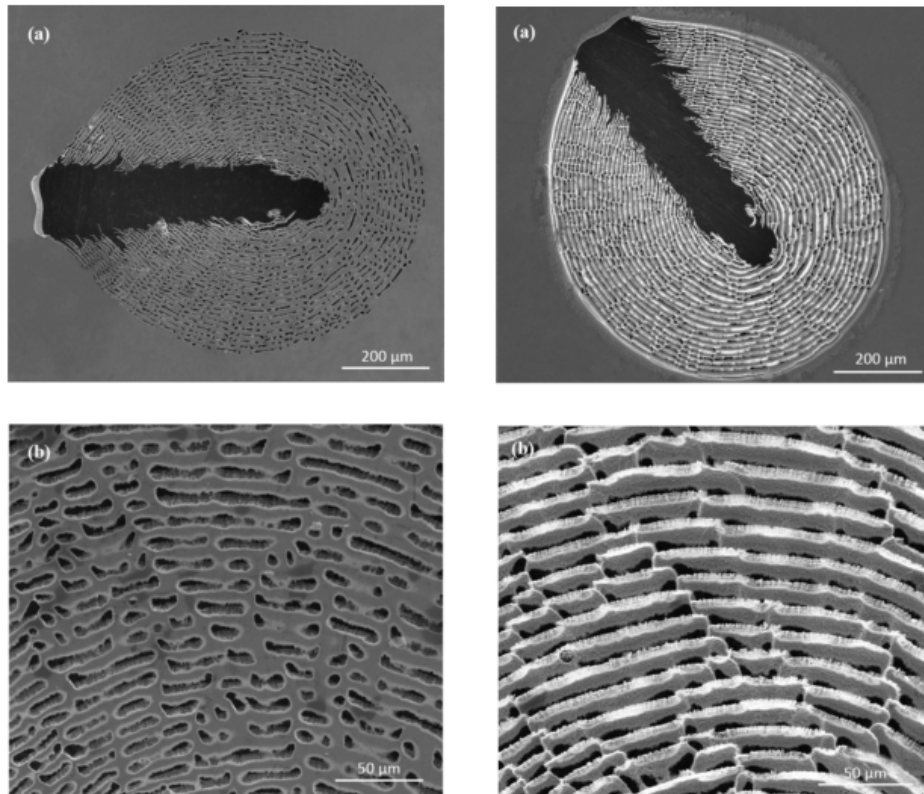


Figure 2.19: Micrographs of a pit cover from 304 stainless steel thin film pitted in a 3.5 wt.% NaCl solution. Left: pit cover as seen on substrate, Right: back side of pit cover removed from insulating substrate [33].

In addition to forming a mesmerizing pit cover, the constraint of an inert substrate influences the growth rates of pits on thin films. Pit growth into thin films can be separated into two distinct regions: hemispherical and radial. At early stages, thin film pit growth is hemispherical, similar to bulk pit growth, but growth into the metal is halted by the substrate and supplanted by radial growth. Figure 2.20 shows that thin film pit radius grows linearly

with time, even though pits can no longer grow deeper [50]. The current measured during pit growth follows a similar trend. During early thin film pit growth, current increase is parabolic, as is expected in bulk pits, though once the pit is constrained by the substrate and pit growth is radial rather than hemispherical, the current change is linear with time, shown in Figure 2.21 [33].

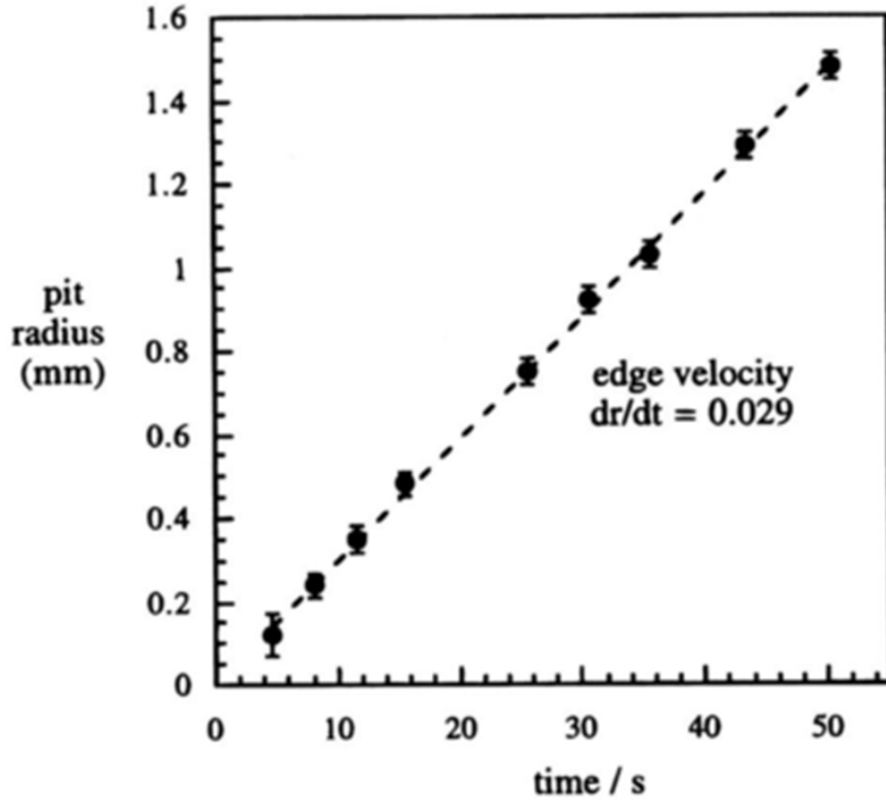


Figure 2.20: Radius as a function of time during pit growth in a 15 wt.% Cr steel in acid [50].

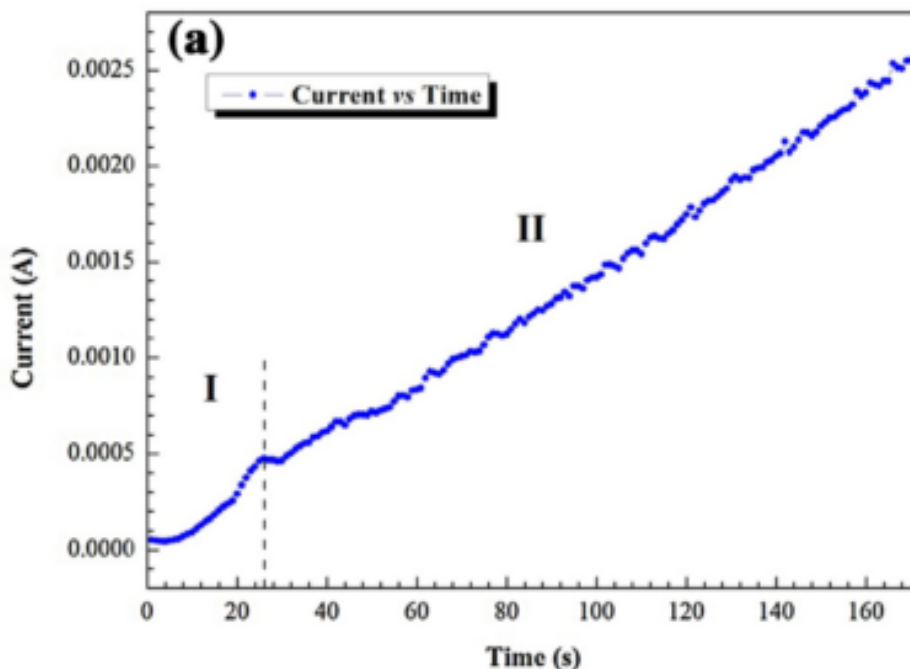


Figure 2.21: Current as a function of time during pit growth in 304 stainless steel in a 3.5 wt.% NaCl solution. Region I shows a parabolic relation, while region II is linear [33].

2.4.3 Effect of Alloying on Passivity and Corrosion

Advanced stainless steels often contain high concentrations of nickel and molybdenum in addition to chromium and iron. In these austenitic steels, the composition of the passive film does not directly reflect the composition of the bulk metal [6]. The alloying elements can have nuanced effects under different conditions such that elements like nickel impact the corrosion resistance without a large presence in the passive film. These highly alloyed steels can also contain intermetallic, carbide, oxide, and sulfide phases, many of which tend to nucleate at grain boundaries. These other phases can decrease corrosion resistance of the steel. For example high carbon steels tend to be stronger, but less corrosion resistant. Precipitation of chromium carbides at grain boundaries leads to chromium depletion along grain boundaries, which may result in intergranular corrosion or intergranular SCC [47, 78, 79]. Chromium depletion at grain boundaries is known as sensitization because the steel becomes more sensitive to corrosive environments. Similar to carbon, nitrogen is also used to interstitially strengthen steels, but nitrogen increases corrosion resistance. It is therefore imperative to weigh the ramifications of each alloy addition against the requirements of each application.

In the pursuit of higher corrosion and SCC resistance, the chemistry of the common austenitic stainless steel 304 alloy (18 wt.% Cr, 8 wt.% Ni) has been modified extensively, as shown in Table 2.2 [80]. Alloy additions such as chromium, nickel, molybdenum, and nitrogen increase chloride corrosion resistance and thus are used extensively in advanced austenitic stainless steels. Varying the concentrations of each of these elements enables tuning of the corrosion resistance. The higher alloy grades, such as 904L and AL-6XN, have been shown to be considerably more corrosion resistant, against both pitting and SCC, than 304 in highly corrosive chloride environments [26].

Alloy	C	N	Cr	Ni	Mo	Cu
304L	0.03	0.10	18.0-20.0	8.0-12.0	-	-
316L	0.03	0.10	16.0-18.0	10.0-14.0	2.0-3.0	-
317L	0.03	0.10	18.0-20.0	11.0-15.0	3.0-4.0	-
317LMN	0.03	0.10-0.20	17.0-20.0	13.5-17.5	4.0-5.0	-
Alloy 20	0.07	-	19.0-21.0	32.0-38.0	2.0-3.0	3.0-4.0
904L	0.02	-	19.0-23.0	23.0-28.0	4.0-5.0	1.0-2.0
AL-6XN	0.03	0.18-0.25	22.0-22.0	23.5-25.5	6.0-7.0	0.75
254SMO	0.02	0.18-0.22	19.5-20.5	17.5-18.5	6.0-6.5	0.5-1.0
25-6MO	0.02	0.15-0.25	19.0-21.0	24.0-26.0	6.0-7.0	0.5-1.0
654SMO	0.02	0.45-0.55	24.0-26.0	21.0-23.0	7.0-8.0	0.3-0.6
27-7MO	0.02	0.3-0.4	20.5-23.0	26.0-28.0	6.5-8.0	0.5-1.0

Table 2.2: Chemistries of common grades of austenitic stainless steels given in weight percent [80].

The main alloying element in most stainless steels is chromium (12-29 wt.%) [81]. Chromium is exploited primarily to produce the Cr_2O_3 -rich passive film [47]. Without chromium, molybdenum and nickel do not increase pitting resistance of iron alloys, and Figure 2.22 shows that increasing chromium concentrations result in more corrosion resistant alloys [21]. Although chromium is necessary in stainless steels, increasing chromium content is not always advantageous. High concentrations of chromium allow σ -phase (FeCr intermetallic) to form if the steel is not heat treated properly or if the part is heated during fabrication or use. Intermetallic phases, particularly σ -phase, deplete chromium from the local metal and form brittle particles, thus adversely affecting both corrosion resistance and mechanical properties

[47, 78]. While many other intermetallic phases exist in stainless steel systems, they are not common in the alloys or conditions studied and thus will not be discussed in this review [82].

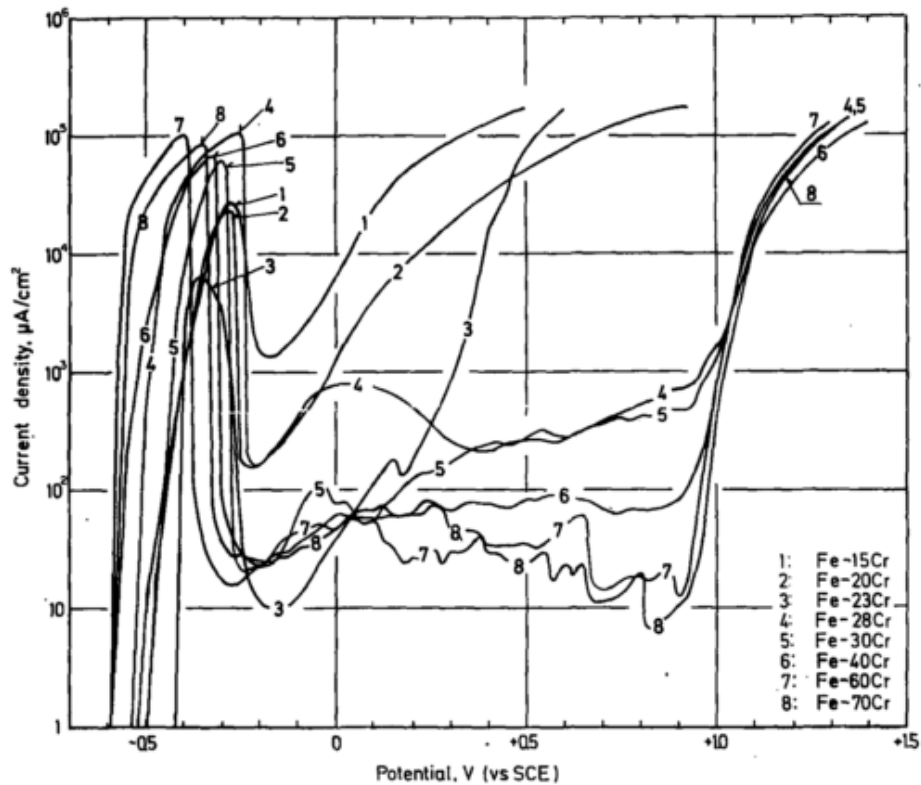


Figure 2.22: Polarization curves showing the passivating effect of Cr on Fe alloys in 1 N HCl at 25 °C [21].

In steels with more than 0.03 wt.% carbon, formation of chromium-rich $M_{23}C_6$ carbide particles can lead to sensitization and intergranular attack as discussed above [75]. Accordingly, many common alloys also have a low carbon variation (e.g. 304L and 316L) to prevent sensitization of the grain boundaries without significant, expensive changes to the alloy composition. The effect of carbon content on carbide formation is shown in Figure 2.23, which compares standard grade (e.g. 304) carbon content of 0.08 wt.% with low carbon grade (e.g. 304L) carbon content of 0.03 wt.% [80]. For example, 304 would form carbide inclusions in under a minute at 800 °C, while 304L would take nearly 10 hours to form carbides at 600 °C. Titanium and niobium are both used to preferentially form fine carbides rather than large chromium carbides in some advanced stainless steels. Fine titanium and niobium carbides decrease sensitization and improve both strength and resistance to corrosion [30, 83].

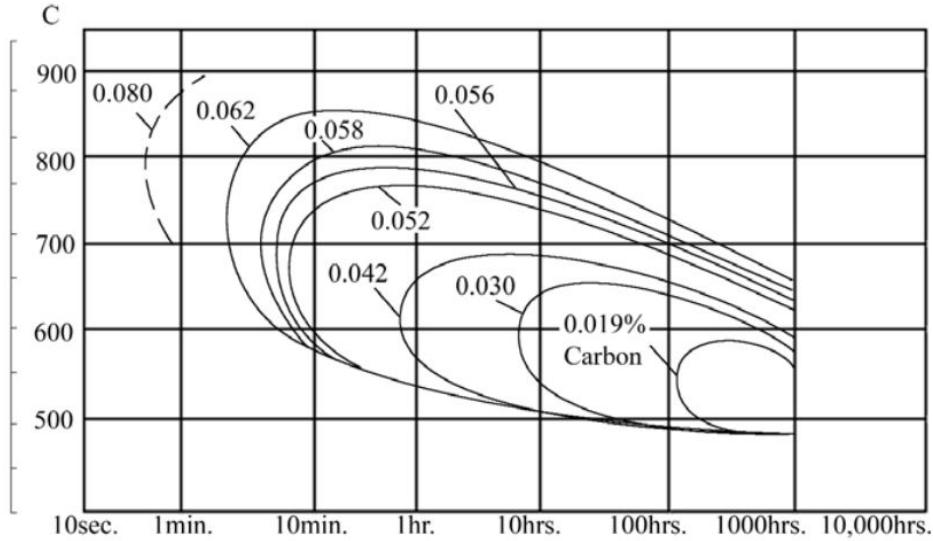


Figure 2.23: Rate dependence on temperature and concentration of sensitization due to carbide formation [80].

Nickel is the second most important addition to austenitic stainless steels (6-28 wt.%), although there is nearly no nickel in the oxide film [6, 59, 81]. The importance of nickel is its austenite stabilizing properties, although it can also increase SCC resistance up to concentrations of about 20 wt.% nickel, above which increasing nickel content does not affect cracking [59]. Nickel increases SCC resistance by increasing the stacking fault energy, resulting in more cross slip and hence lower stress concentrations at slip bands [84]. Lower stress concentrations allow for more defects to form from sources such as mechanical deformation before the passive film is fractured (the first step in crack initiation). Though nickel has little effect on localized corrosion initiation, because it is not a large constituent of the passive film, nickel decreases the active corrosion rate in some environments, including acidic chloride solutions [85]. Alloys with more chromium and molybdenum require higher nickel contents to stabilize the austenite phase; lower alloy austenitic stainless steels (300 series) are considered metastable because their low nickel contents are less effective at preventing δ -ferrite and martensite formation than "super-austenitic" steels (e.g. 904L and AL-6XN) [4, 14, 79, 86, 87]. Increasing nickel content beyond what is required to maintain an austenitic matrix decreases the formation of σ -particles and most other detrimental second phases [78, 82]. Equation 2.14 is used as a guideline in alloy development; it shows that the

concentration of nickel must be at least that of the sum of the chromium and molybdenum contents in order to fully preclude second phase formation [88].

$$\frac{[Ni\%]}{[Cr\%] + [Mo\%]} > 1 \quad (2.14)$$

Molybdenum increases steel strength and, although it is a ferrite and σ -phase stabilizer, molybdenum decreases sensitization by preventing the formation of $M_{23}C_6$ carbides [5, 26, 61, 78, 79]. However, the main reason molybdenum is alloyed in stainless steels is the correlation between molybdenum content and resistance to localized corrosion such as pitting and SCC through multiple mechanisms [6, 28, 30, 55]. Molybdenum replaces some of the chromium in the passive film, stabilizing the oxide and increasing pitting resistance [26, 52, 53, 61]. Addition of molybdenum causes the repassivation rate to increase, as well as increasing the lattice constant of the oxide [53, 56, 57, 87]. Strain in the oxide caused by the increased lattice constant decreases cation diffusion through the passive film, reducing the cation dissolution rate and increasing the lifespan of the passive film [57]. Quick repassivation diminishes localized corrosion by healing the passive film after it is broken, stunting the advance of the corrosion process. This is especially true in the acidic region within a pit. Molybdenum decreases the pH at which stainless steels remain passive in acidic chloride solutions, preventing active dissolution in small, young pits [89]. Even in conditions under which the steel actively corrodes, molybdenum decreases the active dissolution rate, reducing stable pit growth rate [14, 21, 60]. The beneficial effects of molybdenum in resisting acidic environments is shown in Figure 2.24 [21]. The effects of molybdenum can also be complimented by other elements. Nitrogen coupled with molybdenum has been shown to work synergistically to further stabilize the oxide and strain its lattice [28, 90]. The coupling of molybdenum and nitrogen can be attributed to the increase in interstitial diffusion due to the larger lattice spacing.

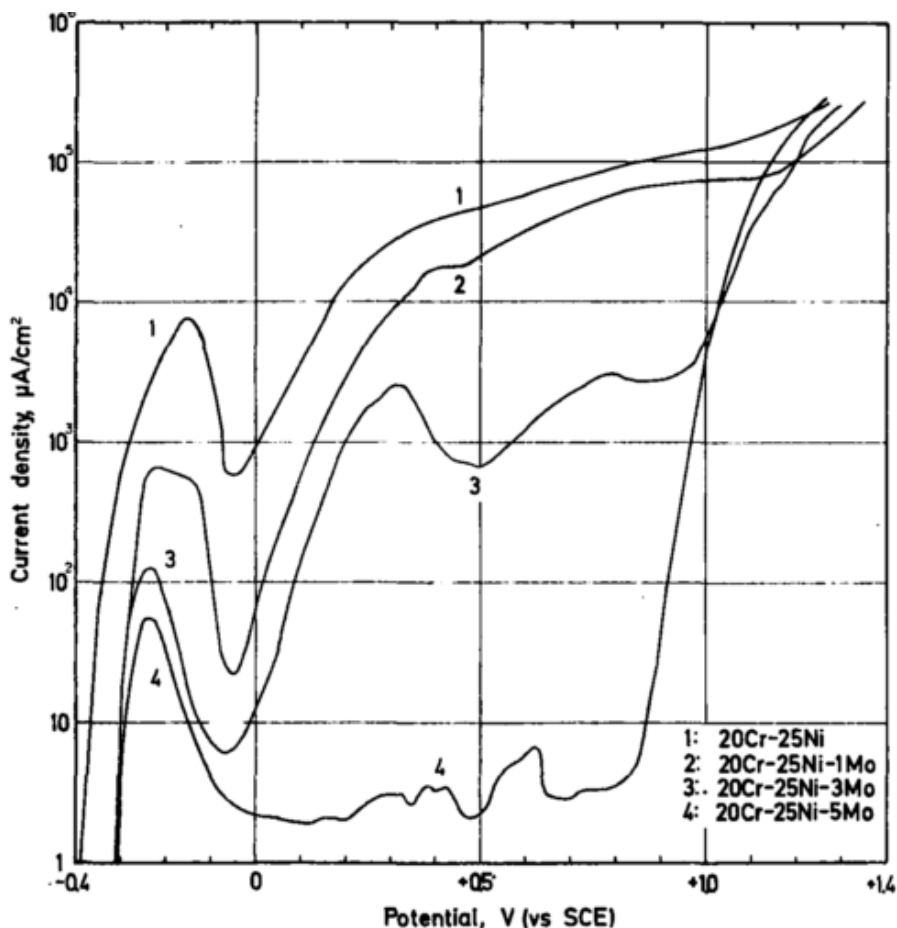


Figure 2.24: Polarization curves showing the passivating effect of Mo on Fe-Cr-Ni alloys in 1 N HCl at 25 °C [21].

High molybdenum steels often contain nitrogen to further increase strength and work hardening through interstitial strengthening, as well as to improve localized corrosion resistance [63, 67, 90]. Along with reinforcing the oxide lattice effect of molybdenum, nitrogen also dissolves into pits, which increases the local pH through the formation of NH_3 [6, 28]. Nitrogen can also be alloyed into steels with the purpose of stabilizing austenite, allowing for a reduction in nickel, resulting in lower cost alloys [30, 67].

Though alloying can intricately affect localized corrosion resistance, general models have been used to estimate alloy corrosion resistance. The simplest method for ranking corrosion resistance of austenitic stainless steels is the pitting resistance equivalent number (PREN), shown in Equation 2.15, where a higher PREN predicts a more corrosion resistant alloy [80, 82, 91–93]. This model, originally developed by Lorenz, was determined by testing

alloys with a range of chromium and molybdenum contents in a saltwater and ferrocyanide solution and observing whether or not corrosion occurred [93]. It was found that above some PREN value, corrosion generally did not occur. Other investigations have used critical pitting temperature measurements to quantify pitting resistance [94].

PREN is an empirical model, so it is limited by the conditions under which its trend has been evaluated. Multiple coefficients have been suggested, most notably $30 * \%N$ observed in high nitrogen steels, but not all of the boundaries of the effectiveness of the PREN model are known [82, 94, 95]. PREN was also formulated to be a simplistic calculation to allow easy comparison of alloys, so many constituents are not accounted for in the most basic equations. Because molybdenum has a higher impact than chromium on PREN, more advanced stainless steels tend to rely heavily on increasing molybdenum content. Higher molybdenum steels also tend to have higher nickel contents in order to offset the ferrite stabilizing properties of molybdenum, but this is not necessarily reflected directly in pitting resistance. The coefficients of some lesser used elements are known, such as tungsten, but are disregarded except when those elements are significantly impactful [96]. PREN is also not valid for extreme alloy chemistries because some of the effects saturate, such as chromium contents above 27 wt.% [97]. Questions have also been raised about the reliance on PREN as a sole defining characteristic of an alloy [94, 98]. While PREN cannot be used as the definitive descriptor of an alloy, it is a useful model to predict pitting resistance of an austenitic stainless steel.

$$PREN = 1 * \%Cr + 3.3 * \%Mo + 16 * \%N \quad (2.15)$$

2.4.4 Effect of Alloying on Passivity and Corrosion in Thin Films

Thin films follow similar trends to bulk stainless steels in regard to alloying effects, with a few notable differences. Because of their homogeneous composition, thin films do not have MnS inclusions, but rather have an even distribution of manganese and sulfur [24]. Without second phases, iron clusters become the primary destabilizing factor for the passive film. Chromium content drastically improves corrosion resistance at 16 wt.% Cr, as shown in Figure 2.25, because the stoichiometry is such that iron clusters no longer form in homogeneous systems [50].

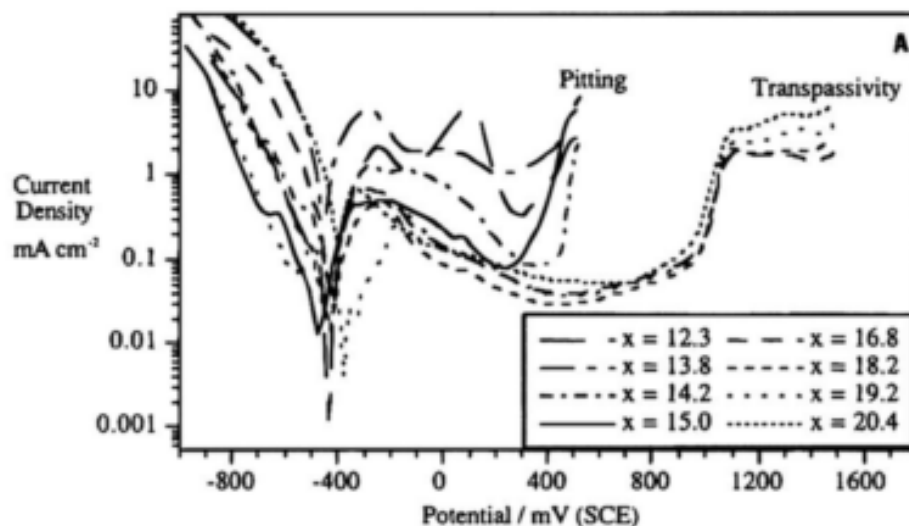


Figure 2.25: Polarization curves showing the effect of Cr content in stainless steel thin films [50].

2.5 Mechanical Behavior in Corrosive Environments - SCC Resistance

2.5.1 Effects of Alloy Chemistry on Mechanical Properties

While corrosion resistance is a key metric by which stainless steels are distinguished, most component failures are due, at least in part, to mechanical failure. Austenitic grades of stainless steel are not generally used in high strength applications, but the constituent elements' effects on mechanical properties cannot be discounted. Frequently discussed are the effects of these elements on the alloy's stacking fault energy (SFE). The SFE controls the tendency of a full dislocation to dissociate into partial dislocations (lower SFE means easier formation of stacking faults and therefore more dissociation of full dislocations). The dissociation affects the work hardening behavior of a metal because full dislocations can cross-slip while partial dislocations cannot. The motion and build-up of dislocations is an important factor when considering the SCC behavior of stainless steels.

The primary alloying additions to stainless steels, Cr, Ni, and Mo, have major effects on SFE and alloy mechanical behavior. Chromium offers a small amount of substitutional hardening and decreases the SFE [99]. Nickel is mainly added to stabilize austenite and it increases SFE [99]. Molybdenum also decreases the stacking fault energy, but it is a more

effective solution strengthener [87]. Large quantities of molybdenum, above 4 wt.%, increase δ -ferrite formation, which can be detrimental to mechanical properties [5].

The effects of the alloying elements on stainless steel mechanical properties combine with their effects on corrosion resistance when SCC is possible. Molybdenum has been correlated with increasing the threshold stress intensity in corrosive conditions (K_{1SCC}), as shown in Figure 2.26 [100, 101]. Figure 2.27, which mimics the behavior found by Copson, shows the effect of nickel content on alloy SCC resistance [100–102]. Copson used static tests in boiling $MgCl_2$ solutions, while Figure 2.27 shows Speidel's observations of fracture mechanics in boiling $NaCl$ solutions. Part of the challenge in describing the effects of various alloying elements is that alloys with higher molybdenum contents tend to have higher nickel contents, and the effects are difficult to separate.

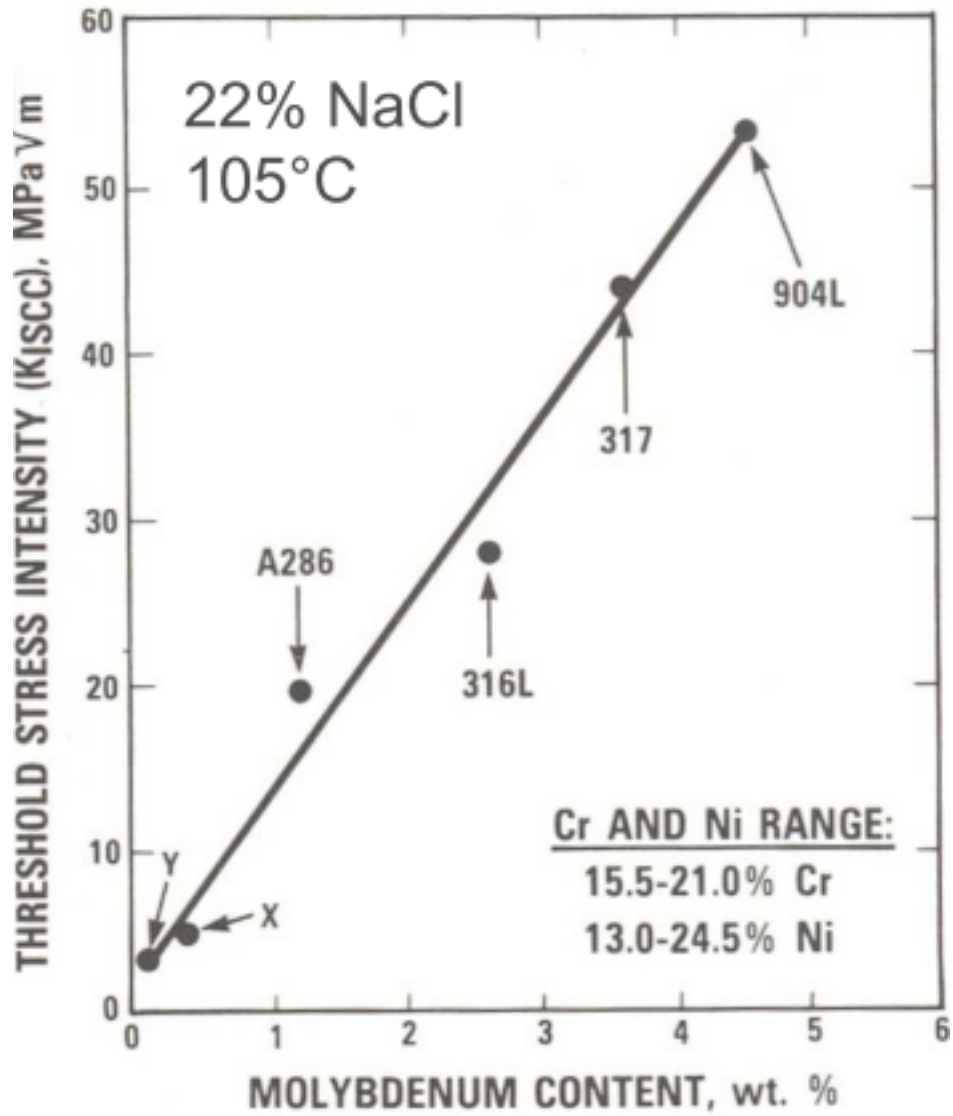


Figure 2.26: Effect of molybdenum on K_{ISCC} in a chloride environment [100].

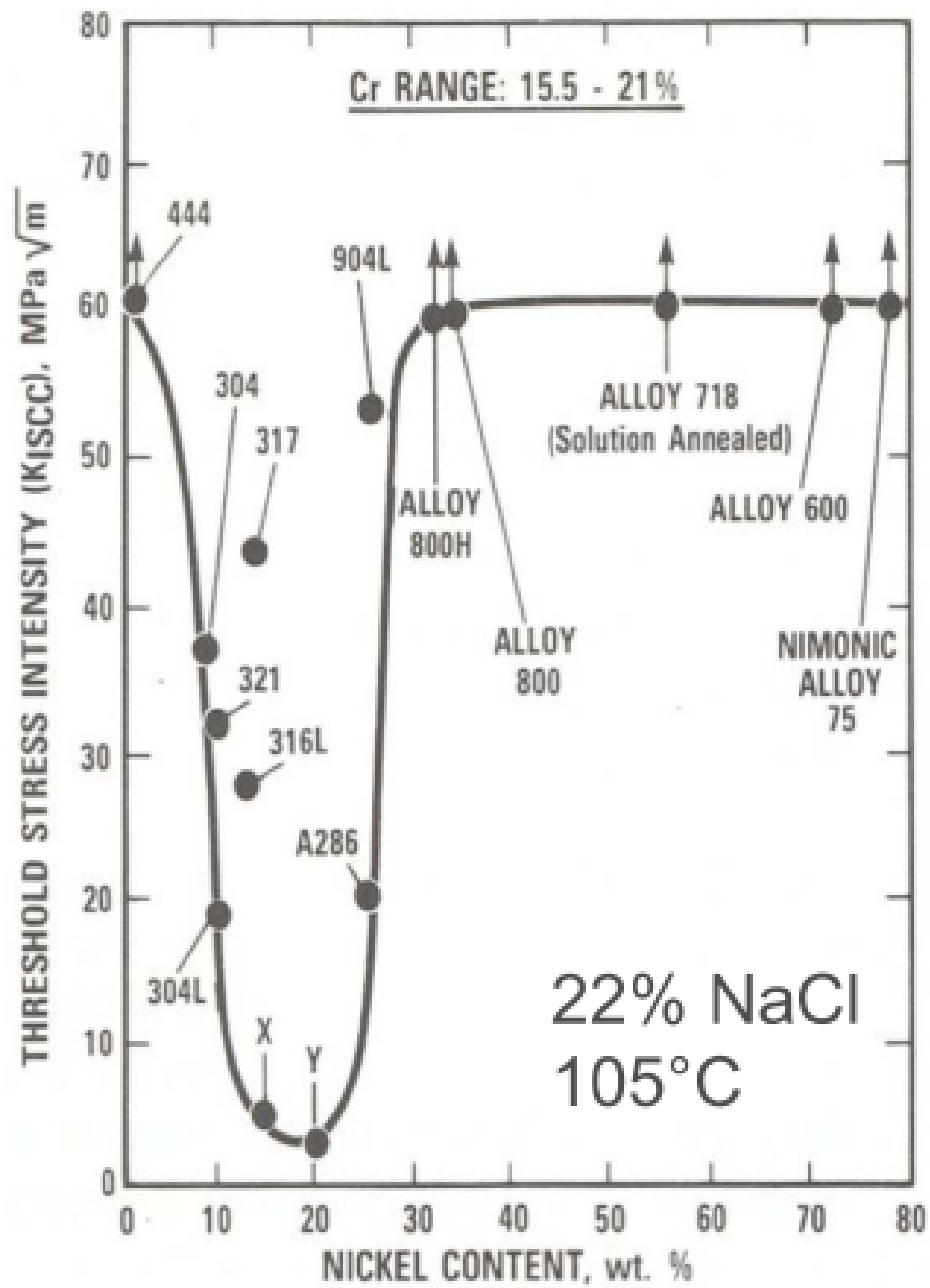


Figure 2.27: Effect of nickel on K_{ISCC} in a chloride environment [100].

Certain stainless steel grades contain nitrogen as an interstitial strengthener in systems where high carbon contents would be disadvantageous. Nitrogen increases strength and work hardening properties and also pins dislocations, creating a finer deformation structure [63, 103, 104]. Unsurprisingly, this improvement in strength is coupled with a decrease in ductility, along with a decrease in stacking fault energy [104].

As with other steels, carbon is added to increase strength. Many alloys have a high carbon variety (e.g. 304H) with 0.08 wt.% carbon to increase strength without costly alloy additions [80]. As previously discussed, high carbon contents greatly increases carbide formation which decreases toughness and increases likelihood of intergranular fracture [105].

2.5.2 Effect of Environment on Mechanical Properties

Stress corrosion cracking, as the name suggests, employs a full spectrum of proposed mechanisms, from primarily mechanically dominant to primarily electrochemically dominant [106]. Within the spectrum, chemical environments can influence mechanical properties and mechanical stresses can impact metal dissolution rates. Chemisorption of anions, especially chlorides, facilitates dislocation nucleation at the metal surface [107]. Anodic dissolution, such as occurs within corrosion pits or in SCC, can also occur on slip bands, leading to increased plasticity known as corrosion-deformation [108].

Just as mechanical properties are not solely dependent on alloy composition and bulk mechanical forces, pit growth is not purely dependent on solution chemistry. Bulk mechanical strain increases the number of stable pits, probably because strain decreases the observed pitting potential [58, 68]. Stress on the metal also increases pit growth rate [62]. The effects of stress and strain are more damaging to corrosion resistance than is surface roughness, which can aid in the concentration of the local environment [62].

Mechanical failure of the passive film is also critical to component failure and is heavily dependent on environmental effects. Stress corrosion cracking can only occur after a rupture of the passive film. The oxide can fail either chemically or mechanically. Stresses on the metal-oxide interface during loading can lead to passive film failure [54]. Substrate deformation does not affect the oxide strength directly, but it can cause detrimental stresses at the film-metal interface as the metal and oxide deform at different rates [52, 59]. Changes in the environment, such as ion concentration (e.g. NaCl and MgCl₂), pH, electric potential, and temperature, can also affect mechanical properties of the oxide layer [6, 31, 52, 54]. The

film can absorb chloride ions, up to 1-5 wt.%, which can sterically drive the film to rupture [6, 31, 52, 54, 55]. Chloride solutions, especially at low pH, decrease passive film strength by dissolving molybdenum and iron cations out of the oxide [52, 54]. Polarization changes passive film thickness, resulting in increasing or decreasing film resilience. While temperature does not directly affect mechanical strength, thermal energy can influence chemical interactions that play a role in mechanical stability [52].

2.5.3 Crack Initiation and Pit to Crack Transition

Stress corrosion cracks, as the name implies, do not form below the yield stress of the material [22]. Crack initiation may take hours at the yield stress, but initiation occurs more quickly as stress increases [22]. Similarly, as stress increases above the yield stress, higher currents pass through the metal, indicating that SCC rate increases at higher stress levels [22]. Transgranular SCC occurs preferentially along specific crystallographic planes, as shown in Figure 2.28 [22]. These cracks transitioned from micro-pits that nucleated at slip steps and grew along slip planes [22].

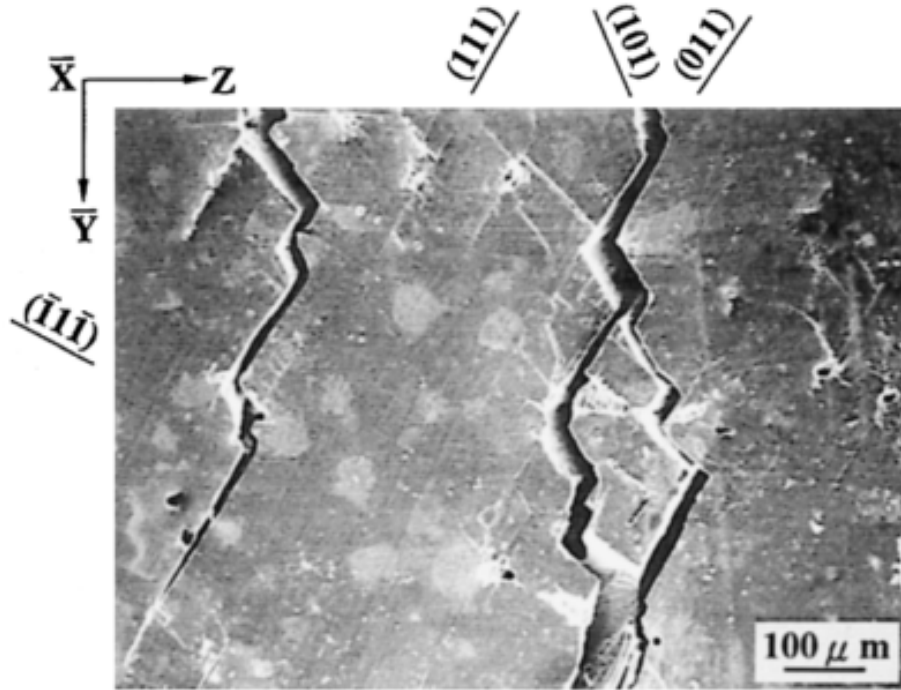


Figure 2.28: SCC grown in single crystal 304 in $2.5 \text{ kmol m}^{-3} \text{ H}_2\text{SO}_4 + 0.4 \text{ kmol m}^{-3} \text{ NaCl}$ with notations of crystallographic orientation [22].

Pitting and SCC can often be found together because environments that cause one generally also cause the other. There is little consensus on the mechanism of SCC initiation, and especially the pit to crack transition. In some systems, cracks tend to form at the mouth of pits, presumably due to the high strain localization [42]. Yet even in these systems, some cracks form at the base of pits, where the localized stresses are most concentrated [42]. A threshold equivalent stress of 700 MPa has been observed for the propagation of cracks in 304L, though crack blunting can then occur to arrest the SCC, as expected for crack growth in a ductile material [109]. New cracks can form at the stress concentration of the crack tip, and it has even been suggested that crack growth is a discontinuous process, requiring alternating crack propagation and arrest events [22, 110, 111].

A number of studies have suggested that SCC can only initiate when pitting growth rates are below a certain threshold. That is, SCC will never manifest under conditions where pitting is rapid. This has been demonstrated in 304 (and similar chemistries) by Tsujikawa [74]. In these tests, pits were initially grown at the alloy's pitting potential and

then the applied potential was dropped to lower values. The specimens were cyclically loaded and SCC initiation was promoted as the magnitude of the potential drop increased.

This interplay was illustrated schematically by Newman in Figure 2.29 [112]. In Figure 2.30, higher SCC crack growth rates were observed in Mo-containing 316 compared to the higher Cr and Ni grade 310 [112]. These results suggest that the relative growth rates of pitting and SCC in a particular environment determine which corrosion process dominates. Because SCC can grow from pits and the two corrosion processes compete for resources, pitting and SCC are competitive processes. SCC tends to be favored in higher repassivation rate alloys and environmental conditions, while pitting is more prominent in lower repassivation systems [113]. Though this phenomenon is not fully understood, it is probably due to the interplay between chemically-assisted mechanical failure and mechanically-assisted chemical failure. Pit propagation relies nearly entirely on anodic dissolution at the crack tip, so repassivation can substantially stunt pit growth. Conversely, SCC relies upon mechanical failure augmented by anodic dissolution, so while repassivation slows crack growth, there are more forces at play.

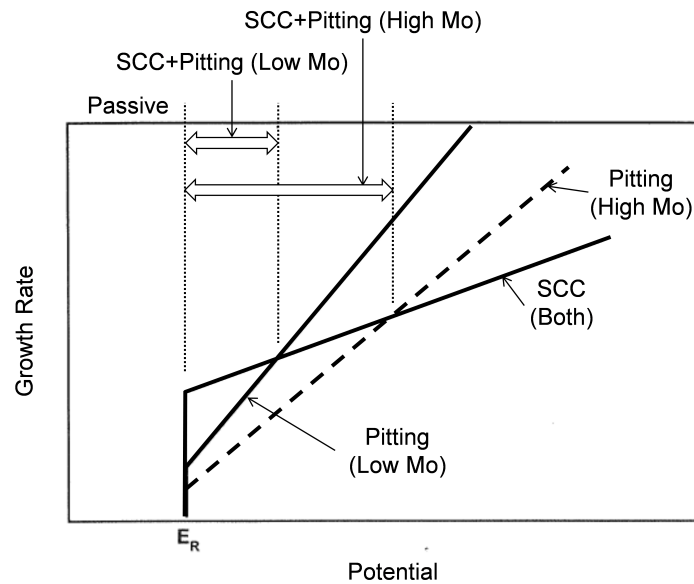


Figure 2.29: Schematic of potential regions in which pit growth or SCC growth dominate [112].

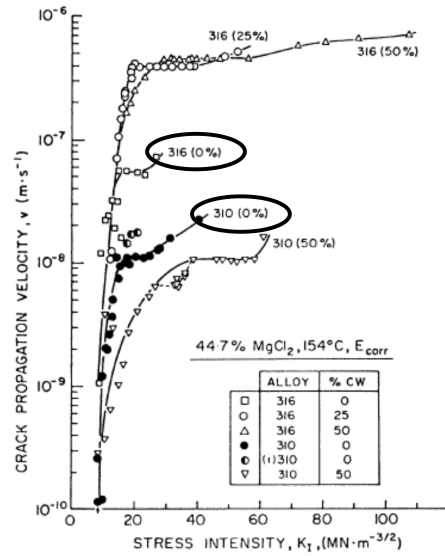


Figure 2.30: SCC growth rates for alloys 316 and 310 [112].

Not all studies indicate these trends, however. A study of alloys with varying Mo content has indicated that increasing Mo content increases SCC resistance in an 18 wt.% Cr, 14 wt.% Ni alloy [114]. There is, therefore, a complicated effect of alloy chemistry on pitting, SCC, and the transition between the two that has not been fully explored.

Chapter 3

Objectives

There are many methods with which to study localized corrosion in stainless steels. This work will concentrate on examining methodologies to evaluate localized corrosion behavior across wide composition ranges in austenitic stainless steels. The relationship between pitting and SCC will be observed primarily in 300 series austenitic stainless steels because of their wide range of molybdenum and chromium contents with otherwise similar alloy chemistry and engineering applications. The corrosion properties of a higher corrosion resistant alloy, AL-6XN, will also be measured for comparison.

Pitting resistance will be measured through potentiodynamic polarization without an applied external stress. The effects of environmental conditions will be measured for each alloy using potentiodynamic polarization at differing temperatures and pH values in aqueous chloride environments. However, in commercial alloys, a direct comparison between composition and localized corrosion cannot be determined because multiple components are changed between each alloy. It is possible to manufacture model alloys by sputtering thin films with chromium or molybdenum gradients, allowing for simple comparison across a spectrum of alloy compositions. The thin film corrosion can be related to bulk corrosion by comparing the corrosion properties of thin films alloys with their bulk counterparts. Methods will be developed to measure localized corrosion spatially to enable measurements across gradient systems.

Slow strain rate testing (SSRT) will be used to relate polarization response under varying conditions to the environmental effect on SCC. Resistance to SCC will be quantified by comparing the bulk change in mechanical properties between dry and corrosive conditions. To further understand the difference between these alloys, the conditions under which each alloy

undergoes SCC will be determined. This determination will be accomplished by controlling pit and crack initiation and growth through potentiostatic and drop-potential SSRT.

Chapter 4

Hypotheses

- Chromium and molybdenum each increase corrosion resistance, but have different effects in various environments as a result of different mechanisms. There are conditions under which increasing chromium results in higher resistance to stable pit formation than increasing molybdenum content, such as elevated temperatures in chloride containing environments.
- The lower electrical conductivity of thin films compared to bulk metals leads to higher corrosion resistance in thin films.
- For stainless steels in chloride solutions, monotonic loading can be used to show the same interplay between SCC and pitting that has been observed with cyclic loading.

Chapter 5

Experimental Equipment

Corrosion science is a well established field, so many instruments and techniques have been designed to further the study of corrosion processes. However, new methods and equipment are still being developed to continue to advance the current understanding of corrosion. This chapter summarizes the instrumentation that is used to observe and control corrosion phenomena. Because of the ever-changing nature of science and technology, equipment, also discussed in this chapter, was designed to enable the study of the corrosion phenomena of interest through novel methods, such as scanning vibrating electrode technique and slow strain rate testing of flat samples.

5.1 Instrumentation

A Gamry Interface 1000 potentiostat controlled by Gamry Framework software was used for all potentiostatic and potentiodynamic polarization experiments in the Avesta Cell and SSRT environmental chamber setups discussed below. The polarization tests were all measured using a three electrode system with a platinum wire as the counter electrode and saturated calomel electrode (SCE) reference electrode (+0.242 V *vs.* standard hydrogen electrode). An electrolyte bridge was used to prevent heating of the reference electrode. The electrolyte bridge was constructed by affixing a glass capillary with a 1.6 mm diameter opening to a beaker with a hose barb via a flexible polymer tube. For polarized scanning vibrating electrode technique (SVET), a Gamry reference 600+ potentiostat was used with a platinum counter electrode and Ag/AgCl reference electrode placed directly in the environmental chamber.

Two load frames were used throughout this work. The specimens assessed in environmental chamber (EC) 1 (described in Section 5.2.3) were elongated using a model 1125 Instron load frame with a 5500R crosshead. An extensometer measured the gauge section of each sample tested in air. All measurements (load and extension measured by crosshead, and strain by extensometer) were collected using Instron Bluehill software. The testing in EC 2 and EC 3 (described in Sections 5.2.4 and 5.2.5) was conducted with an MTS 880 servohydraulic load frame. The load frame was controlled by a Flextest 40 controller with load and actuator displacement monitored throughout the test using MTS TestSuite Multipurpose Elite software.

All light optical microscopy (LOM) was imaged using a Zeiss Axio optical microscope. An FEI Aspex Explorer scanning electron microscope (SEM) with secondary electron imaging mode was used to observe samples from EC 1. Samples from EC 2 and EC 3 were observed using a Philips XL30 SEM. All metallographic samples were polished to 1 μm and electrolytically etched with oxalic acid.

Thin film sample resistivities were measured using a Signatone S-301-6 four-point probe resistivity meter connected to a Keithley 220 programmable current source and Keithley 182 sensitive voltmeter. The surface of each sample was either left as received or cleaned using isopropanol as necessary. The resistivity, ρ , is calculated based on the probe geometry using Equation 5.1, where t is film or sample thickness, I is applied electrical current, and V is measured electric potential [115].

$$\rho = \frac{\pi}{\ln(2)} t \frac{V}{I} \quad (5.1)$$

An Ametek VersaSCAN SVET running VersaSCAN software was used to characterize the local current at the surface by measuring the voltage drop in the solution along the surface of a sample through a Pt vibrating microelectrode. The microelectrode had a diameter of 2 μm at the tip. The measurements were carried out using the Pt microelectrode immersed in an electrolyte on the sample surface. Figure 5.1 shows a schematic of a SVET system where the Pt electrode vibrates in the z direction while scanning in the x and/or y directions [116]. Ionic currents caused by corrosion in an anodic region lead to potential gradients above the sample, such as shown in Figure 5.2 [117]. The potential gradients contain elliptical equipotential surfaces between which the vibrating electrode moves, creating a measurable potential difference, shown in Figure 5.3 [117]. Thus SVET characterizes the ionic current emanating from anodic corrosion sites through a measurement of the change in potential.

Large magnitudes of change in potential relate to large ionic currents, which in turn relate to high corrosion rates. By scanning across the surface of a corroding metal, corrosion sites can be spatially mapped along the surface and their corrosion rate can be observed through the magnitude of the ionic current. It is important to note that the potential measurements (V) do not relate to the potential on the sample surface or corrosion reaction potentials.

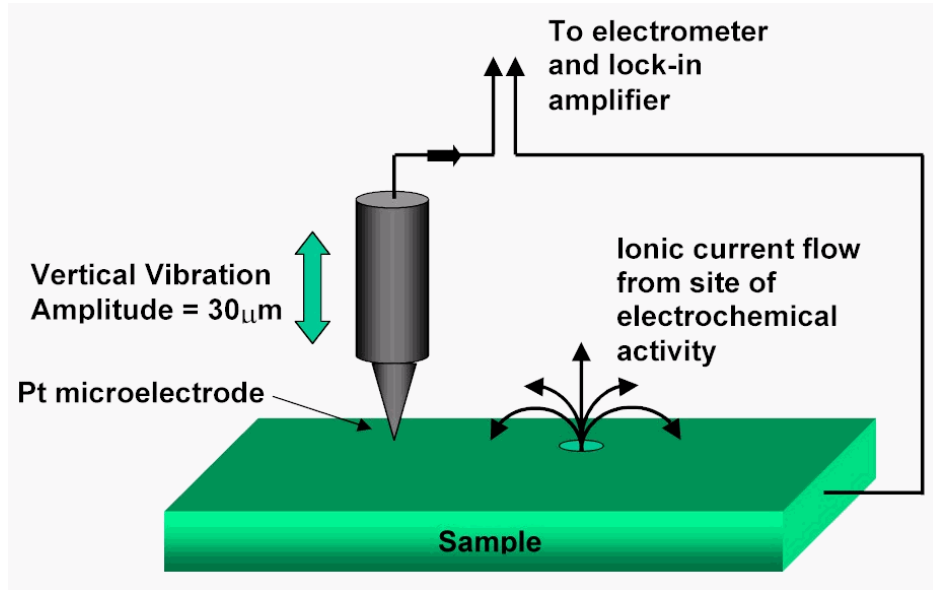


Figure 5.1: Schematic of a SVET measurement. The Pt electrode vibrates in the z direction while scanning in the x or y directions [116].

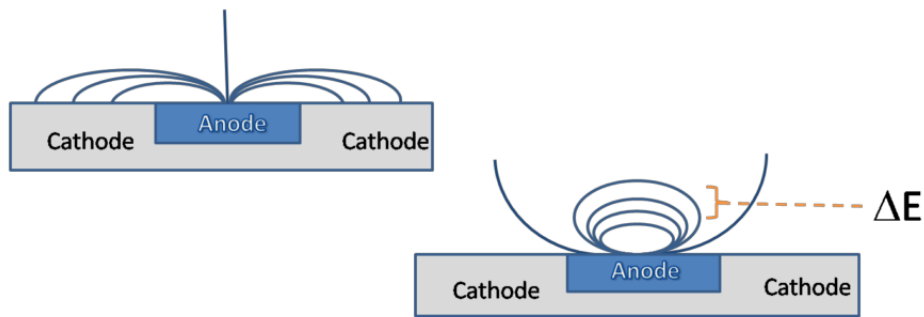


Figure 5.2: Ionic currents caused by corrosion lead to potential gradients above the sample [117].

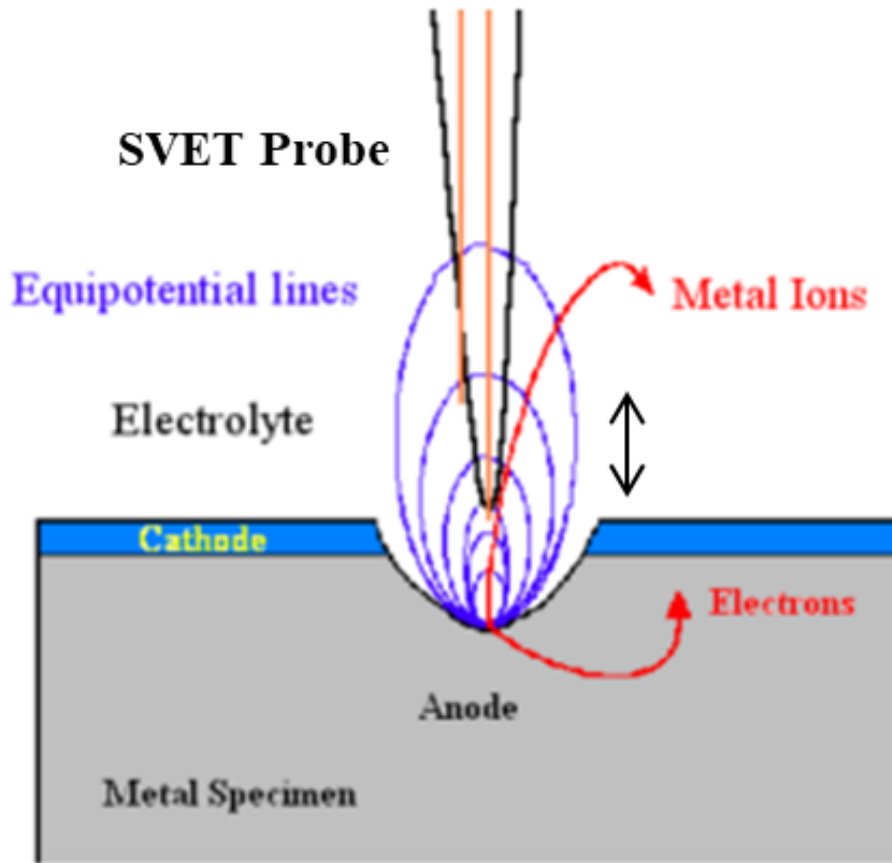


Figure 5.3: Potential gradients are measured by vibrating the electrode between equipotential surfaces [117]. The schematic shows an example of localized corrosion.

5.2 Environmental Chambers

5.2.1 Avesta Cell

A Bank Elektronik double walled Avesta cell was used to measure the polarization response of each alloy while preventing crevice corrosion at the specimen edges. This cell allows a small flow of deionized water into the environment through a filter paper annulus at the circumference of tested area, as shown in Figure 5.4. The hole in the filter paper ring had a diameter of 12 mm, leaving an exposed sample area of 1.13 cm^2 . The solution was aerated using either compressed air from the building air supply or an aquarium air pump. Alternatively, the solution was deaerated using nitrogen gas for 30 minutes before the test and throughout the test [50, 92, 118]. The gas (air or nitrogen) supply was high enough to

cause cavities to form in the solution, but not high enough to cause extreme turbulence. The environment was heated by a Thermo-Fisher DC10 heater with silicone oil and an Omega spot heater on the back of the sample. In order to prevent long heating times, the water used in the heated experiments was preheated and left to equilibrate for no more than 5 minutes before the polarization began.

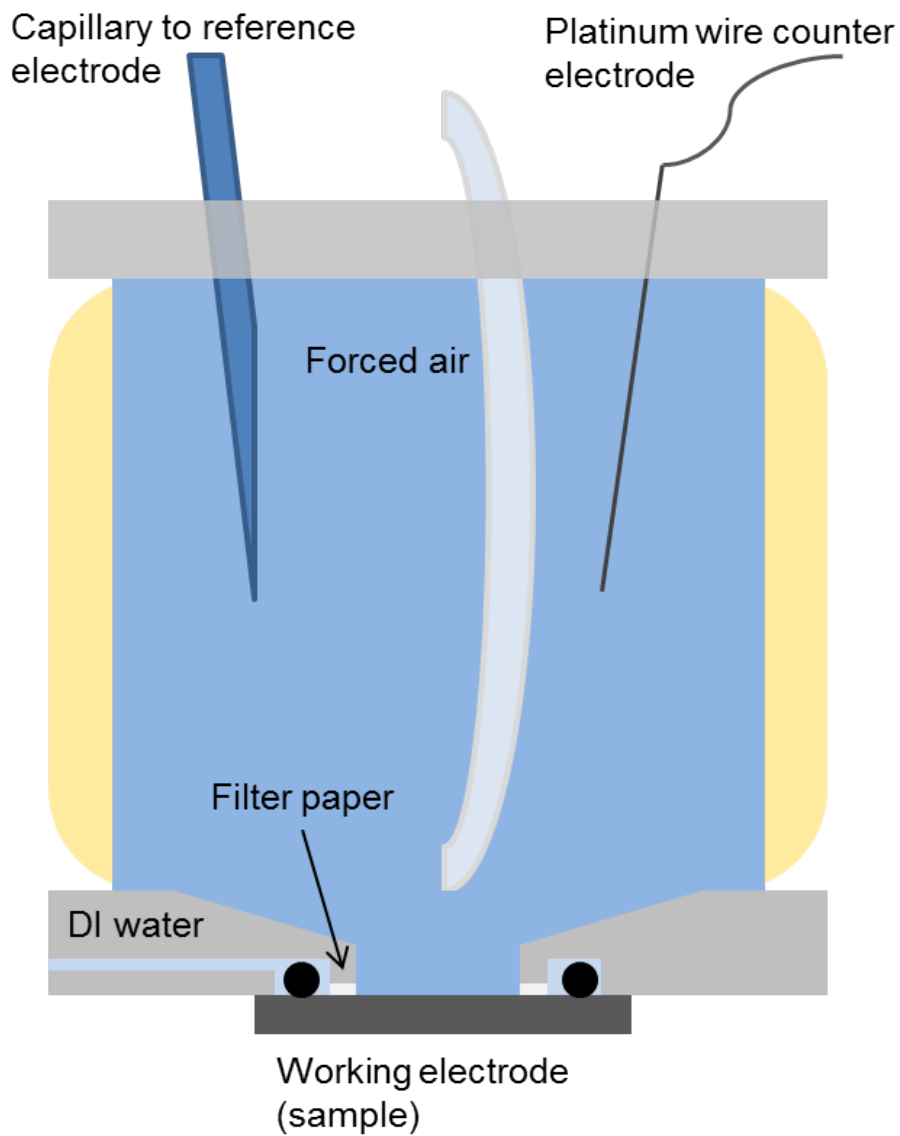


Figure 5.4: Diagram of an Avesta cell.

5.2.2 SVET Environmental Chamber

The SVET environmental chamber consisted of a glass dish and plastic sample holder seated upon three thumb screws to allow for precise leveling before each experiment to ensure the vibrating electrode-sample distance remained constant as the electrode moved across the sample. The same environmental chamber was used throughout all SVET testing, however several methods for establishing, controlling, and maintaining the environment were used. The setup used in Section 7.2.3 is shown in Figure 5.5. A droplet of solution was placed on the surface of the sample in which the vibrating electrode could scan. Figure 5.6 shows a schematic of the setup used in Section 7.2.4. This design is similar to that of Figure 5.5, however polytetrafluoroethylene (PTFE/Teflon) tape added to contain the edge of the water drop. The water drop is contained to inhibit a water-metal-air interface. All polarized samples, discussed in Section 7.2.4, require the environmental chamber to be filled, shown in Figure 5.7.

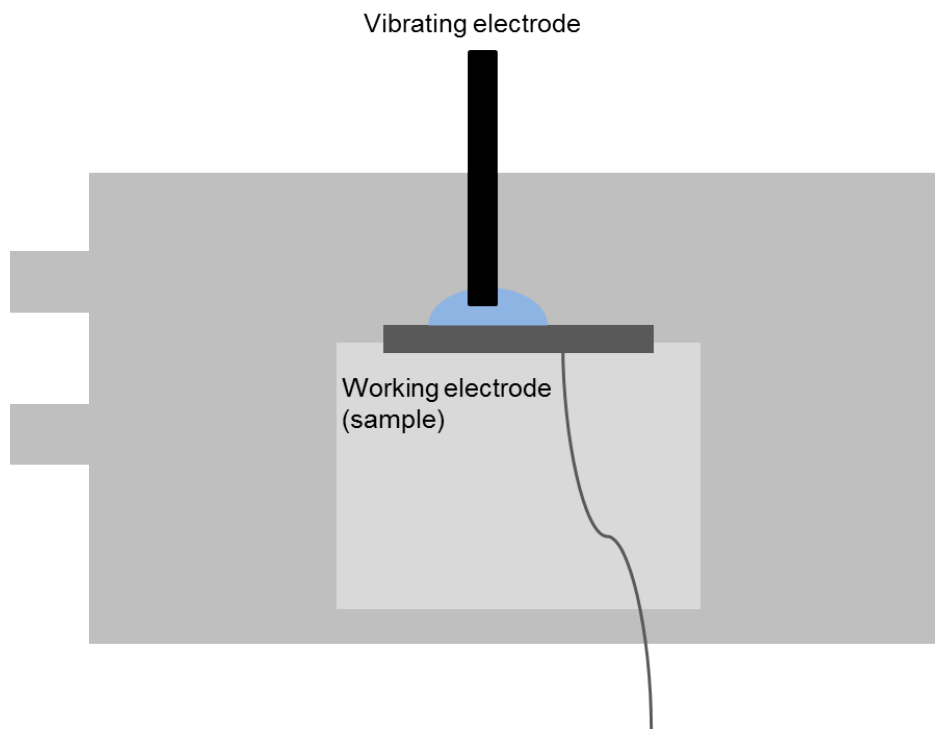


Figure 5.5: Diagram of SVET environmental chamber with droplet.

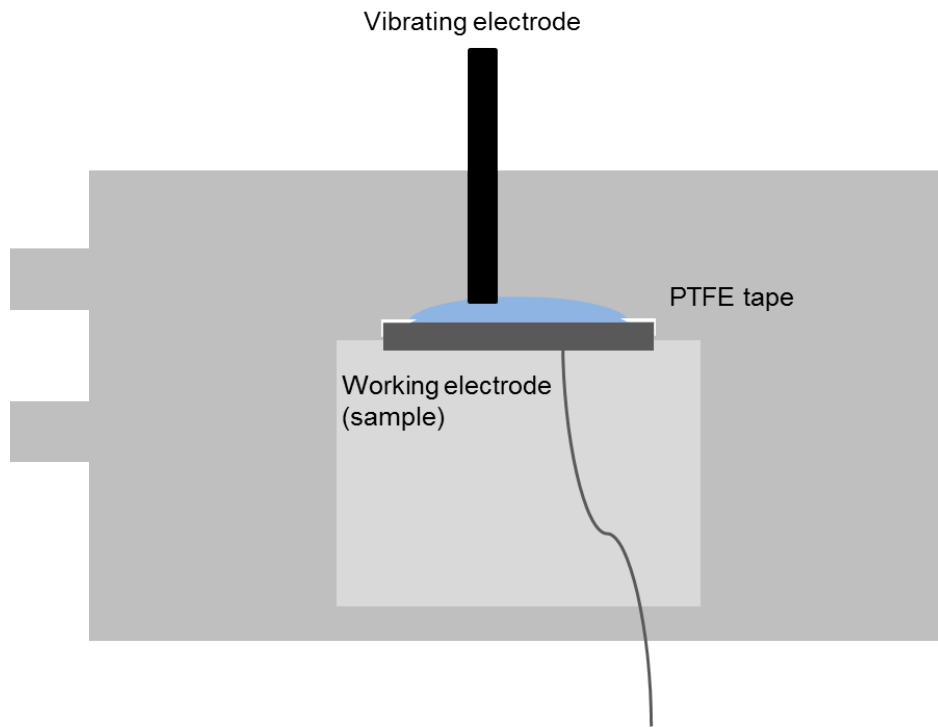


Figure 5.6: Diagram of SVET environmental chamber for non-polarized samples.

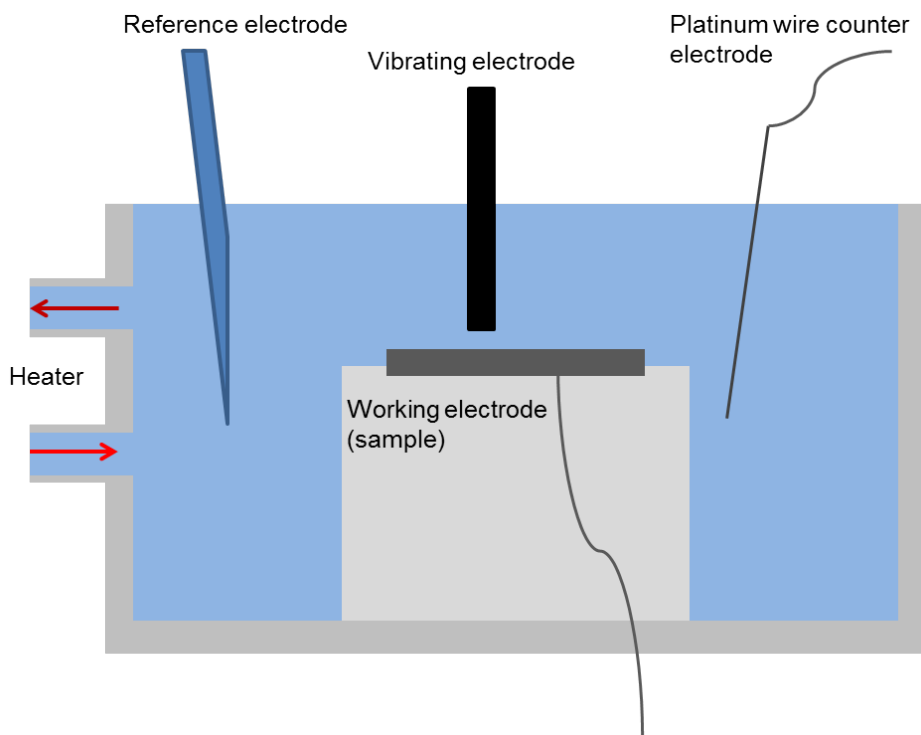


Figure 5.7: Diagram of SVET environmental chamber for polarization.

5.2.3 SSRT Environmental Chamber 1

SSRT testing requires an environmental chamber to maintain a corrosive environment around the sample during deformation. Three different environmental chamber designs were used due to varying constraints on the experimental setup. The first environmental chamber design (EC 1), shown in Figure 5.8, allowed the use of pin-loaded samples with 17-4 PH clevises and pins. Pin-loaded samples were used to allow for consistent sample placement and robust environmental sealing. The base and lid were machined from polysulfone and the base plug and wall were polycarbonate. Viton o-rings were used to create all of the seals. The simple design ensured consistent assembly and good sealing properties; however disassembly led to some solution leakage.

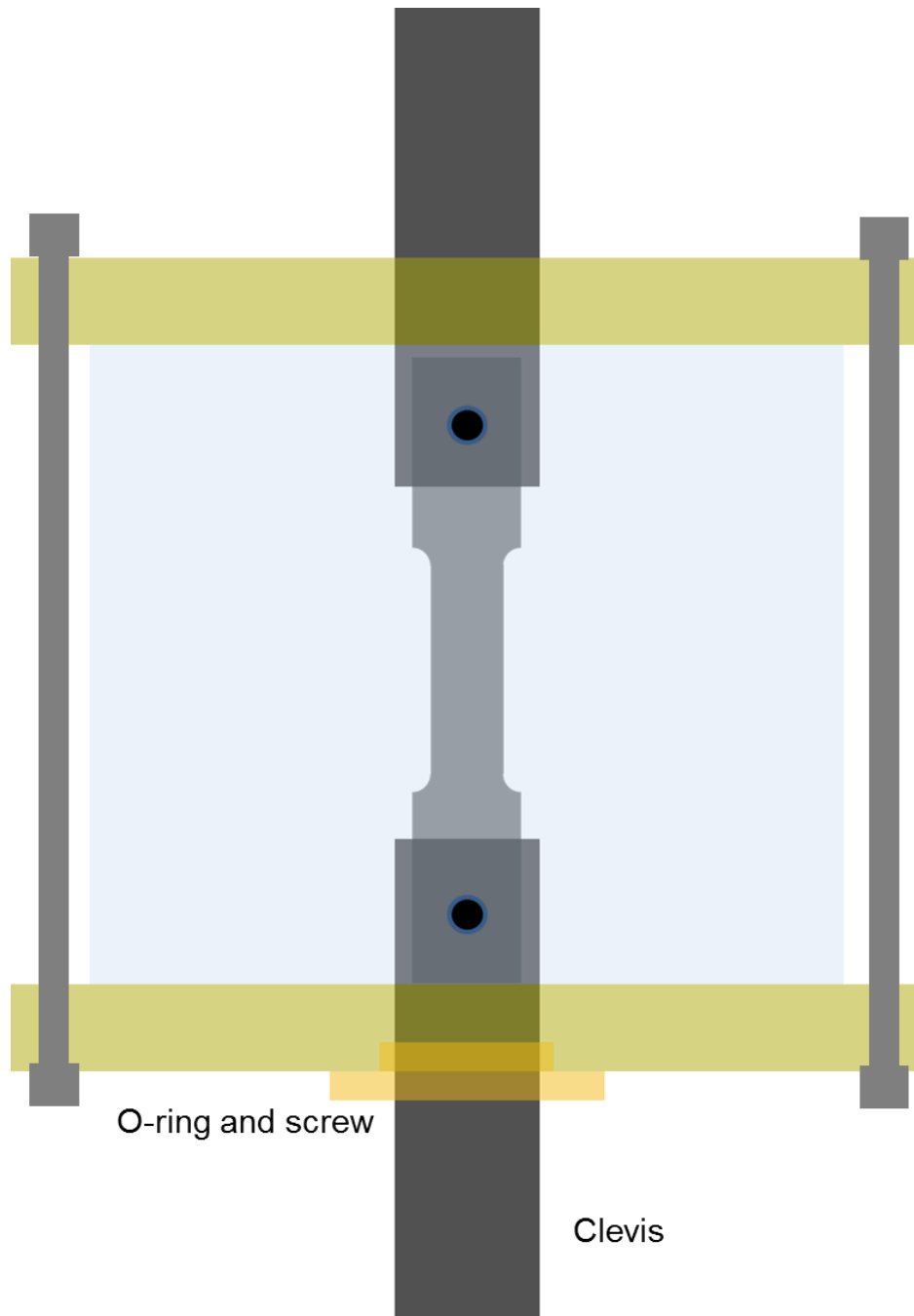


Figure 5.8: Diagram of environmental chamber 1 and test sample. The sample is held in place via pins within the clevis.

The clamped lid design required a pump to introduce and remove the salt solution to and from the chamber. The solution was pumped at a rate of approximately 150 mL/min

through Omega FPU500 peristaltic pumps from a reservoir to the environmental chamber and back. The flow rate was chosen to be high enough to prevent large gas pockets from forming in the water lines, which prevents flow, while being slow enough to minimize any turbulence in the environmental chamber. Flow rate has little effect on corrosion as long as there is no turbulent flow on the sample [119]. The apparatus contained about 4 L of solution in order to dilute any corrosion products. About 1 L of solution was added to the reservoir after about half of the samples from each alloy had been tested in order to account for water loss during sample change. The entire solution was replaced and the water lines were purged between testing each alloy so as to prevent cross contamination. Although there was slight water loss through evaporation, small salt deposits formed around any openings in the system, implying that the water solution chemistry changed very little throughout the experiment.

The solution reservoir was heated with a hotplate. An in-line heater (copper pipe with heat tape), and heat tape and insulation surrounding the environmental chamber prevented heat loss throughout the experiment.

EC 1 was effective for non-polarized tests, however it was not suitable for polarized testing because the clevises were not electrically isolated from the sample. Hence if the sample were polarized, the clevises would be as well, and corrode accordingly, changing the polarization response of the system and weakening the clevises. There may have been galvanic interaction between the clevises and samples in non-polarized conditions because 17-4 pH is less noble than the austenitic stainless steels of interest. However, significant corrosion was not seen on the clevises, so this effect was determined to be negligible.

5.2.4 Environmental Chamber 2

Polarized measurements require that the working electrode be electrically isolated within the environment and that the sample be electrically accessible to the potentiostat. EC 2 was designed to remove the clevis from the environment by directly gripping the sample, as shown in Figure 5.9. A clamshell lid was used to allow easy access to the sample during setup and to facilitate adding the environmental solution. The base and lid were both made from ultra-high molecular weight polyethylene (UHMW PE) and the wall was polycarbonate. J-hooks were used to hold the wall to the base so the lid would not have to be bolted to the base, as with EC 1. Room temperature vulcanizing (RTV) silicone was used to seal

the wall to the base because, after high temperature use, the base showed significant creep deformation and caused leakage.

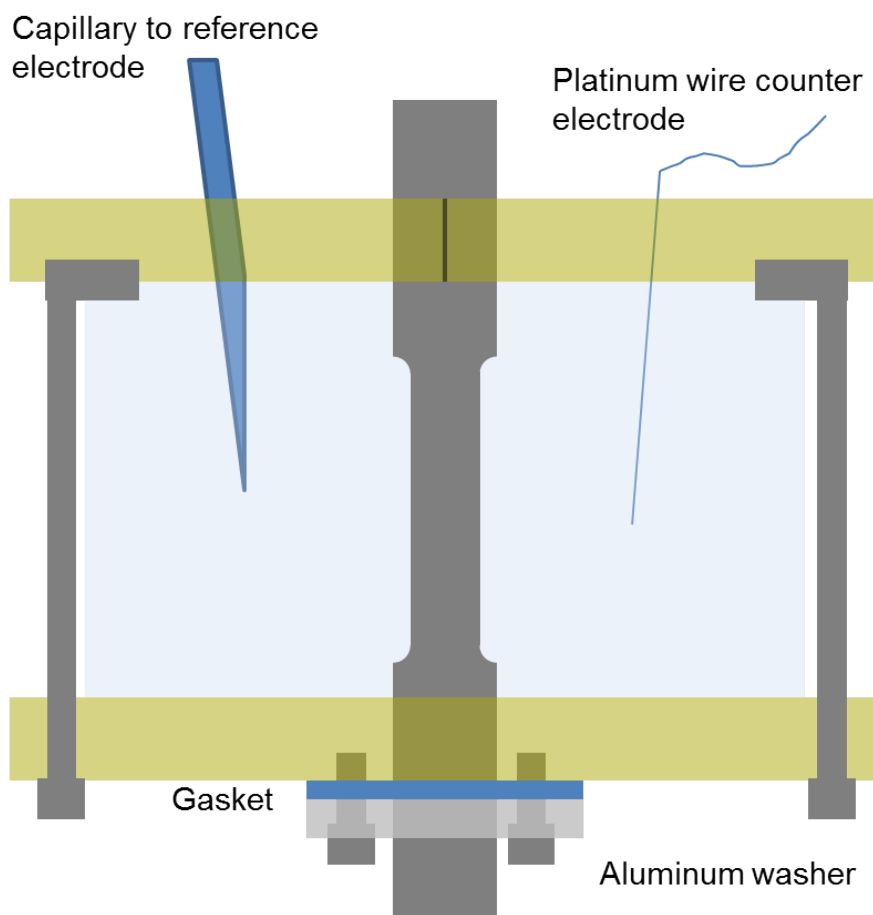


Figure 5.9: Diagram of environmental chamber 2 and test sample. The sample is clamped directly to the load frame via hydraulic wedge grips

Samples were secured and sealed to a piece of 1.6 mm all-purpose gasket material by first coating the interface with an aerosol asphalt, then laying a bead of RTV silicone. The gasket was attached to the base by an aluminum washer screwed to the base.

Temperature control up to 70 °C was achieved using a Thermo-Fisher DC10 fluid immersion heater. Silicone oil was heated and circulated through tubing immersed in the environmental chamber. In order to avoid long heating times, the water used in the heated experiments was preheated and left to equilibrate for no more than 5 minutes before the polarization began. A stir bar was used to obviate hot spots and localized corrosion product buildup.

5.2.5 Environmental Chamber 3

Problems with securing the EC 1 and EC 2 were caused by the screws and bolts used, so EC 3 was constructed to avoid the use of any threaded hardware, as shown in Figure 5.10. The base was polysulfone, the wall was polycarbonate, and they were fastened together with a bead of RTV silicone on the inner and outer interface. A slot was carved into the center of a silicone stopper through which samples were inserted. The bottom of the stopper was sealed to the samples with RTV silicone. To prevent leakage and crevice corrosion, the top of the stopper was sealed to the sample using PTFE paste, which contains fine particles of PTFE suspended in a hydrophobic solvent. The stopper was press-fit into the base. The same clamshell lid as EC 2 was used. The environment was heated using the same method as with EC 2. Glad Press'n Seal plastic sheeting was used to slow evaporation out of the chamber and condensation on the grip region of the sample. Some evaporation was inevitable because the system was not perfectly sealed, so the electrolyte bridge discussed above was used as an external reservoir to buffer solution height within the environmental chamber and through which more solution could be added during long experiments.

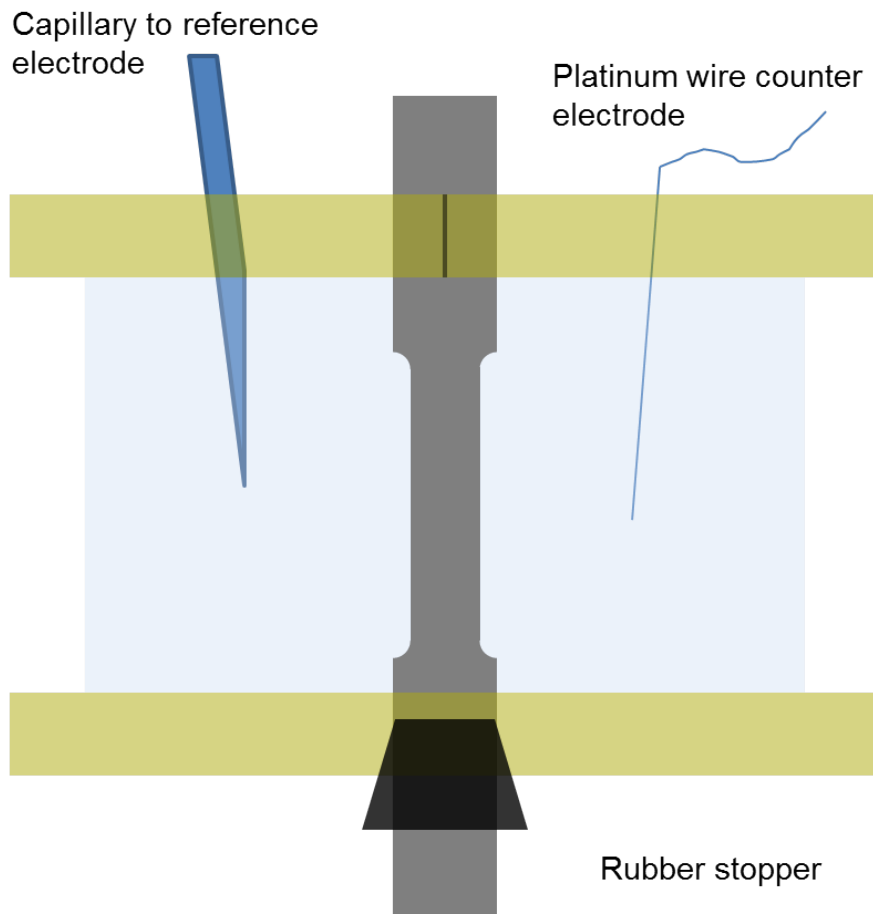


Figure 5.10: Diagram of environmental chamber 3 and test sample. The sample is clamped directly to the load frame via hydraulic wedge grips

Chapter 6

Bulk Potentiodynamic Polarization

The corrosion properties of a metal can be quantified using electrical polarization. For stainless steels, a transition from passive to stable corrosion can be measured by a sharp increase in current as voltage is increased. In this chapter, potentiodynamic polarization is employed to quantify the pitting resistance of various commercial stainless steels in chloride environments of low and high concentrations and multiple temperatures.

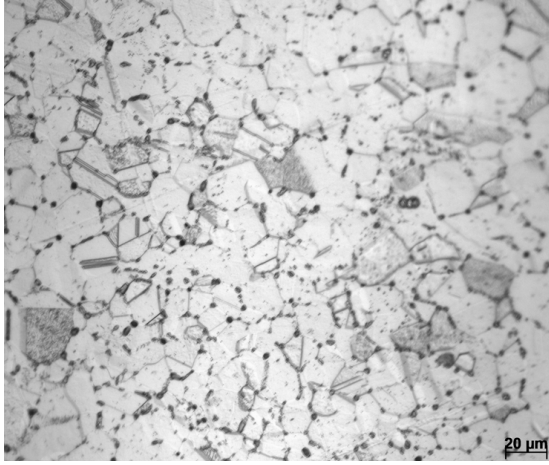
6.1 Experimental

6.1.1 Materials

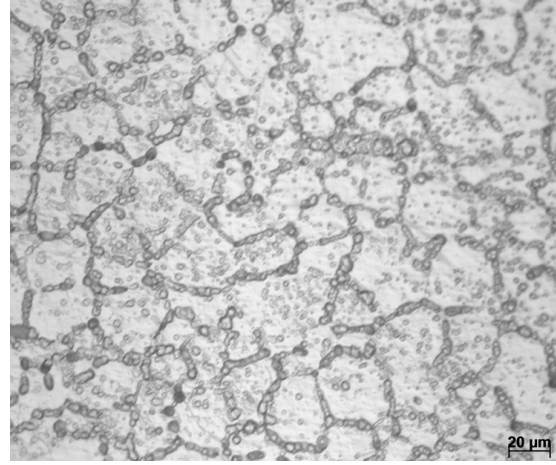
In order to study the effects of alloy chemistry on localized corrosion, the alloys in Table 6.1 were chosen due to their generally increasing chromium, nickel, and molybdenum contents, resulting in a range of PREN. Each alloy was provided as mill annealed 1.5 mm thick sheet, from which 25 mm square samples were cut for polarization testing. Microstructures of the as-received mill annealed materials are shown in Figure 6.1. All testing was in the as-received condition. The samples were wet-ground with 500 grit SiC paper to maintain a consistent surface finish. After grinding, samples were cleaned with acetone and allowed to rest for at least 24 hours to enable the formation of a passive film. The samples were mounted in the Avesta cell and potentiodynamically polarized from -0.4 V *vs.* SCE at a rate of 1 mV/s. All samples were allowed to equilibrate in the solution for 5 minutes before polarization began.

Alloy	C	S	Mn	Cr	Ni	Mo	N	PREN
304L	0.021	0.001	1.61	18.24	8.05	0.43	0.07	21
310S	0.047	0.001	1.88	24.70	20.20	0.07	0.03	25
316L	0.022	0.001	1.54	16.60	10.10	2.09	0.05	24
317L	0.028	0.001	1.24	18.10	11.80	3.00	0.07	29
AL-6XN	0.016	0.0001	0.52	20.55	23.66	6.15	0.21	44

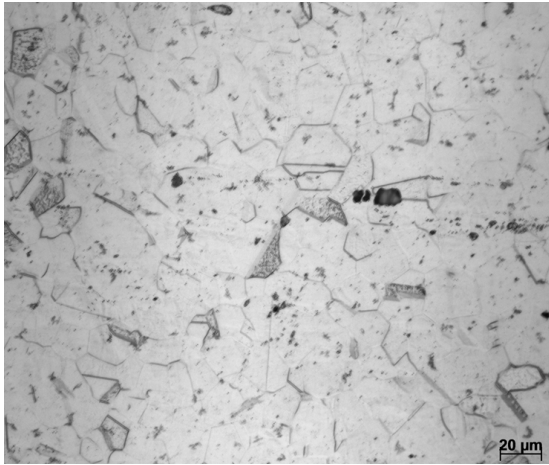
Table 6.1: Alloy chemistry for polarization, EC 2, and EC 3 tests. Alloy compositions in weight percent.



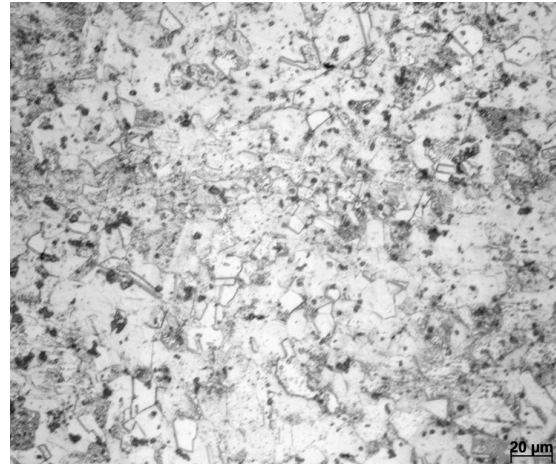
(a) 304L



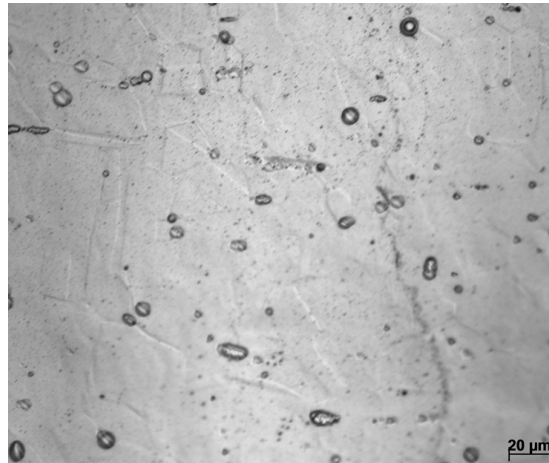
(b) 310S



(c) 316L



(d) 317L



(e) AL-6XN

Figure 6.1: LOM of microstructures of each alloy.

6.1.2 Effects of Environmental Conditions

Each alloy was tested in multiple environments to understand the effect of temperature, chloride concentration, and dissolved oxygen on polarization response, as well as to determine the environment in which SCC testing should occur. To observe the effect of temperature, each alloy was potentiodynamically polarized at 24, 50, and 70 °C in a 3.5 wt.% NaCl non-aerated (no forced air, *not* de-aerated) aqueous solution. The effect of aeration was observed by polarizing at 24 °C in a 3.5 wt.% NaCl aerated aqueous solution. The impact of salinity was measured by testing each alloy at 24 and 70 °C in a 25 wt.% NaCl aerated aqueous solution. These tests were performed by potentiodynamically polarizing each sample until a sharp increase in current occurred, indicating the pitting potential, transpassive dissolution, or oxygen evolution. Once the potentials at which current increases were determined, cyclic polarization curves were generated with the maximum potential at approximately the voltage at which the current density was 100 $\mu\text{A}/\text{cm}^2$. At the maximum potential, the voltage was swept in the cathodic direction at 1 mV/s until the current density dropped below the passive current density. Multiple unidirectional polarization tests were measured to determine the cyclic reversal potential.

6.1.3 Effects of Temperature

Though a cursory test of temperature effects was discussed in Section 6.1.2, a more in depth study was undertaken to elucidate the effect of alloy chemistry on the temperature at which stainless steels pit. The solution for all tests was aerated 3.5 wt.% NaCl aqueous solution. Sample preparation and potentiodynamic scan rate were the same as in Section 6.1.2. Each alloy was cyclically polarized with the scan reversing directions at a current density of 1 mA/cm². Each alloy was tested three times each at 24, 30, 40, 50, 60, and 70 °C.

6.2 Results and Discussion

6.2.1 Effects of Environmental Condition

An annotated example of polarization curves, measured using cyclic polarization, is shown in Figure 6.2. The non-aerated potentiodynamic polarization responses of each alloy were measured at 24, 50, and 70 °C, shown in Figure 6.3. The noise in the curves, particularly near

the corrosion potentials, is attributed to the potentiostat switching between measurement ranges (auto-range feature of the potentiostat to allow measurements across large current variations). A summary of the potentials at which current density sharply increases is shown in Figure 6.4. These potential values, as well as the passive current densities, are comparable with available literature results, however similar studies have not been published for some of the alloys tested here [120]. The sharp increase in current density is attributed to the pitting potential, however a voltage above 1 V indicates oxygen evolution and/or transpassive dissolution. The differentiation between oxygen evolution and transpassive dissolution is discussed later in this section. Alloys that are passive until water oxidation or transpassive dissolution do not have a pitting potential under those conditions. At 24 °C, only 304L and 316L were prone to stable pitting in 3.5 wt.% NaCl solution, however 310S showed evidence of metastable pitting. Metastable pitting is characterized by the current transients, sharp spikes in current in the passive region due to the quick repassivation of these pits. At elevated temperatures, 310S and 317L each expressed a true pitting potential, while the current density increase of AL-6XN remained around 1 V. It is unclear whether AL-6XN showed a true pitting potential or if the transpassive dissolution potential decreased at higher temperatures. Under conditions at which each of the 300 series steels were susceptible to pitting, the pitting potentials correlated with PREN across all alloys and temperatures. Because AL-6XN does not follow this trend, it is likely that the high molybdenum and nitrogen contents increase the critical pitting temperature for this system above 70 °C, which has been shown to be between 70 and 90 °C [95].

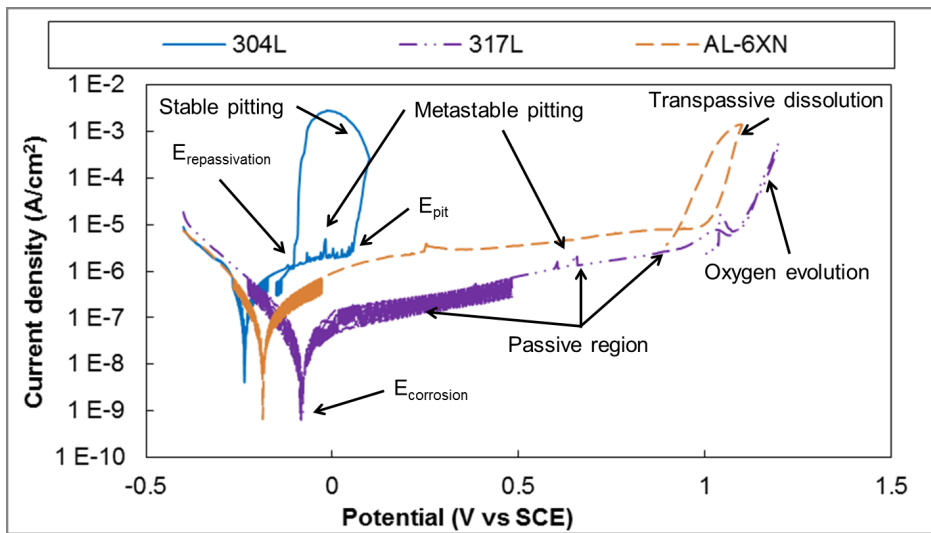
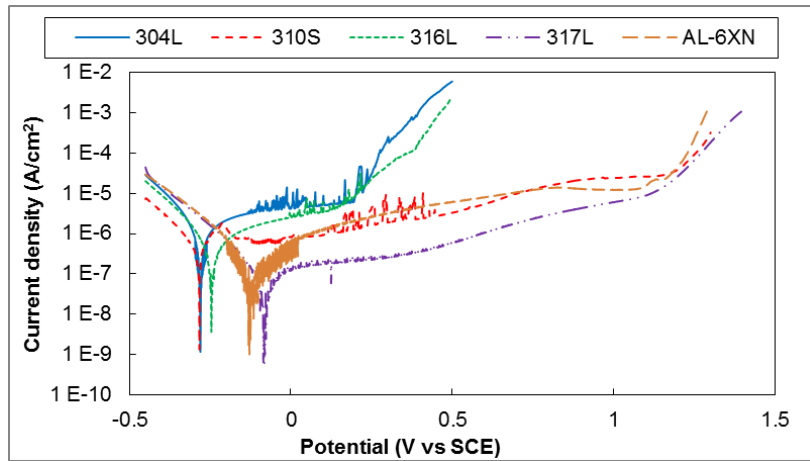
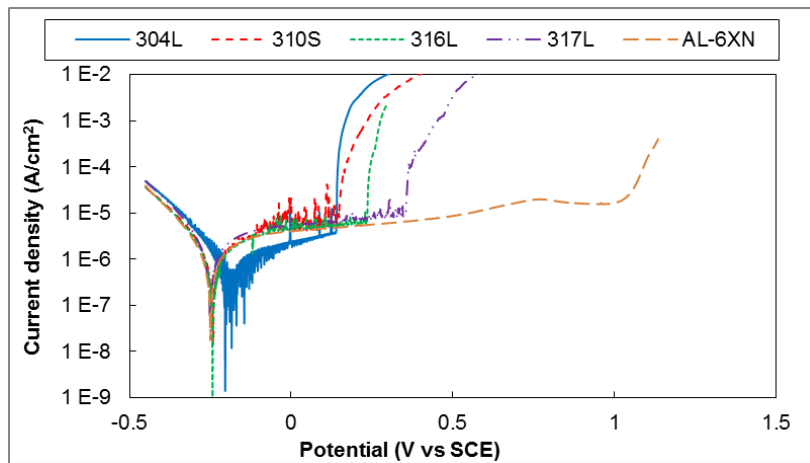


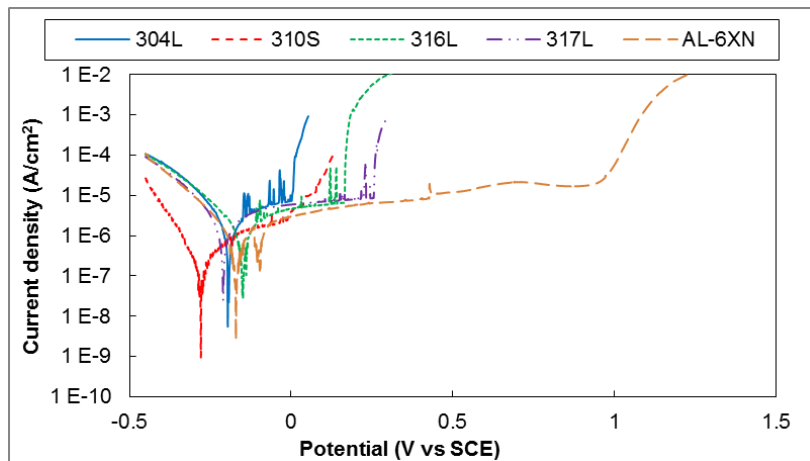
Figure 6.2: Annotated cyclic polarization of three alloys.



(a) 24 °C



(b) 50 °C



(c) 70 °C

Figure 6.3: Potentiodynamic polarization of each alloy in non-aerated 3.5 wt.% NaCl solution.

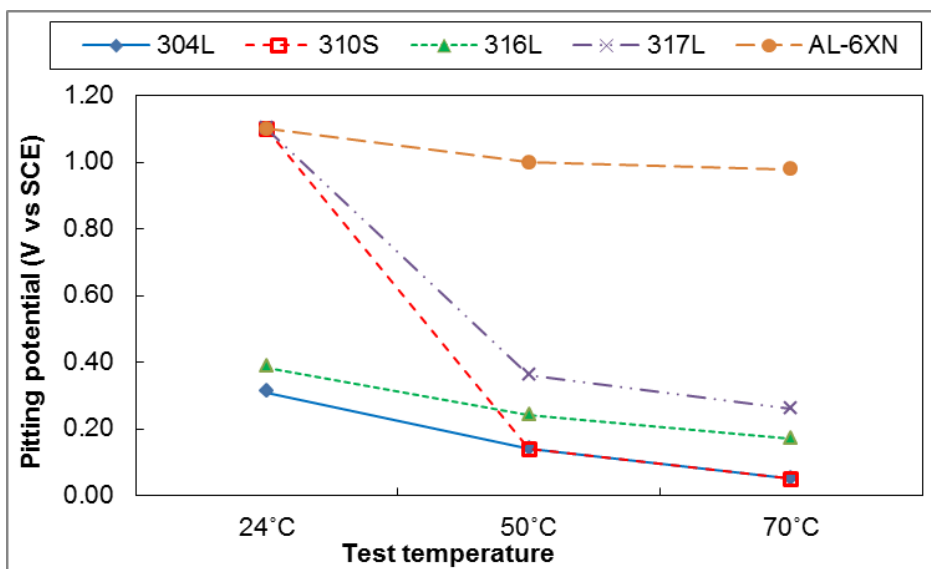


Figure 6.4: Pitting potential or oxygen evolution of each alloy at 24, 50, and 70 °C in non-aerated 3.5 wt.% NaCl solution.

Potentiodynamic polarization response is very dependent on solution chemistry, including dissolved oxygen concentration. To maintain a consistent dissolved oxygen concentration across tests, the solution was aerated throughout polarization. Aerated potentiodynamic polarization responses of each alloy were measured at 24 °C, shown in Figures 6.5. The results are very similar to those of the non-aerated tests, but, as expected, the repeatability between tests is higher with the aerated solution.

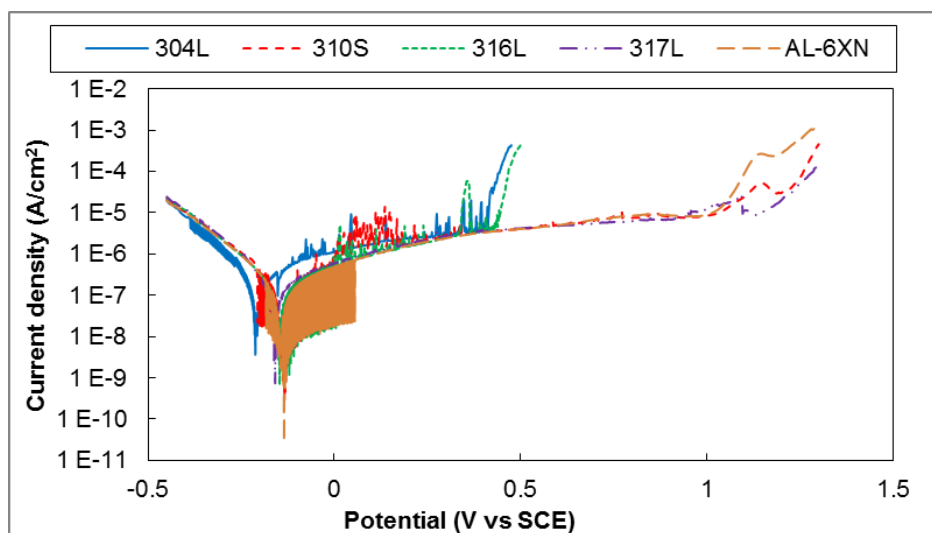


Figure 6.5: Potentiodynamic polarization of each alloy at 24 °C in aerated 3.5 wt.% NaCl solution.

Aerated potentiodynamic polarization responses of each alloy in 25 wt.% NaCl solution measured at 24 °C and 70 °C are shown in Figures 6.6 and 6.7. A comparison of pitting potentials between high and low concentration solutions at 24 °C and 70 °C is shown in Figure 6.8. The higher concentration solution did not decrease the critical pitting temperatures of 310S or 317L below 24 °C. The critical temperature of AL-6XN was still above 70 °C. Though a decrease in critical pitting temperature was not measured, pitting potentials (for each system with a measurable pitting potential) decreased in the higher concentration solution. The pitting potentials of 304L and 310S at 70 °C were near the corrosion potential and difficult to differentiate.

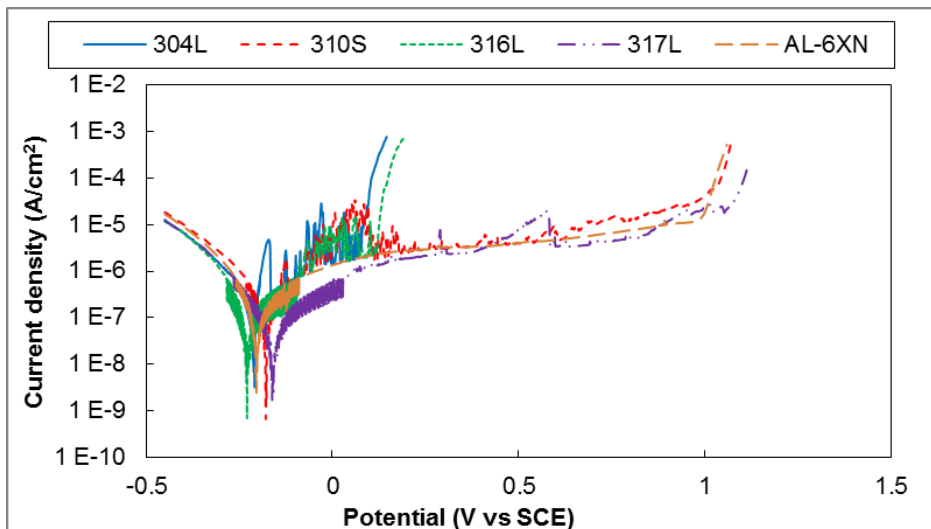


Figure 6.6: Potentiodynamic polarization of each alloy at 24 °C in aerated 25 wt.% NaCl solution.

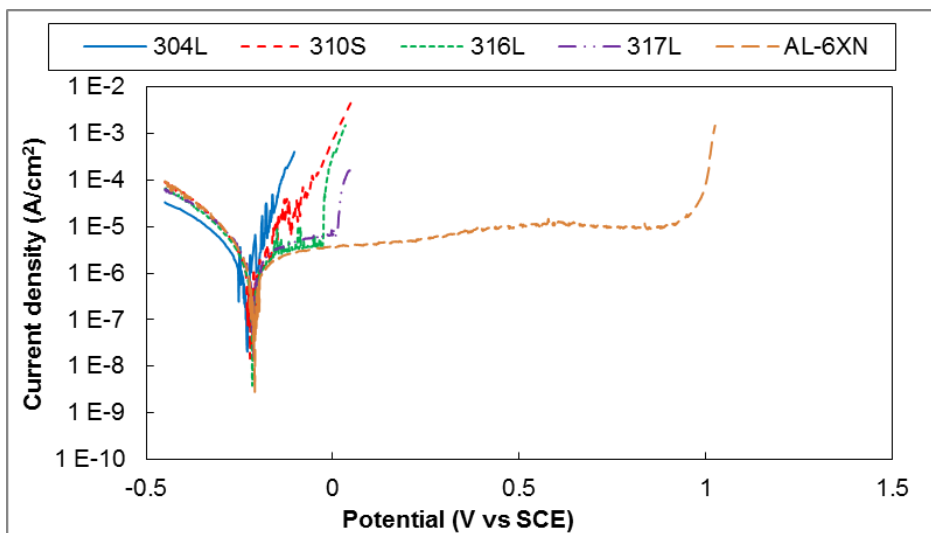


Figure 6.7: Potentiodynamic polarization of each alloy at 70 °C in aerated 25 wt.% NaCl solution.

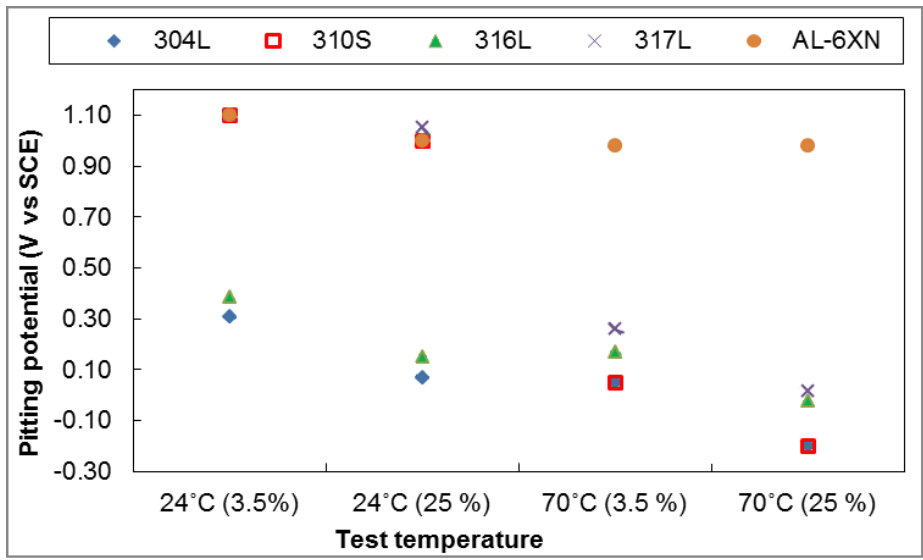


Figure 6.8: Pitting potential or oxygen evolution of each alloy at 24 °C and 70 °C in non-aerated 3.5 wt.% and aerated 25 wt.% NaCl solution.

Cyclic polarization is typically used to determine an alloy's repassivation potential, but the same technique can also be used to differentiate between transpassive dissolution and water oxidation at high applied potentials. A hysteresis loop that is above the original curve (the negative polarization direction produces a higher current than the positive polarization, Figure 6.9) indicates that a corrosion reaction has occurred. Conversely, if the hysteresis loop is below the original curve, a surface reaction caused the increase in current during the positive sweep direction [121]. The repassivation potential is that at which the hysteresis loop intersects the passive region. Figure 6.10 shows that 304L and AL-6XN underwent some corrosion process, while 317L remained stable through the oxidation of water at 24 °C in aerated 25 wt.% NaCl solution. It is likely that transpassive dissolution occurred in AL-6XN and 310S, but not in 317L because of the extremely high chromium content of AL-6XN and 310S compared to 317L. The increase in current for 304L was due to pitting and the pits continued to grow until the potential dropped to the repassivation potential. The rise in current from the AL-6XN sample was due to transpassive dissolution, so, unlike on the 304L, the current density reached a maximum at the point at which the polarization reversed direction. The repassivation potentials followed the same alloy and temperature relationships as pitting potential. Higher molybdenum alloys might be expected to have a proportionally higher repassivation potential because molybdenum increases the repassivation rate at lower pH, but this was not observed [53, 56, 57, 87]. A higher repassivation potential for high molybdenum alloys might be observable under polarization with a slower scan rate to allow time for the passive film to form within the pit.

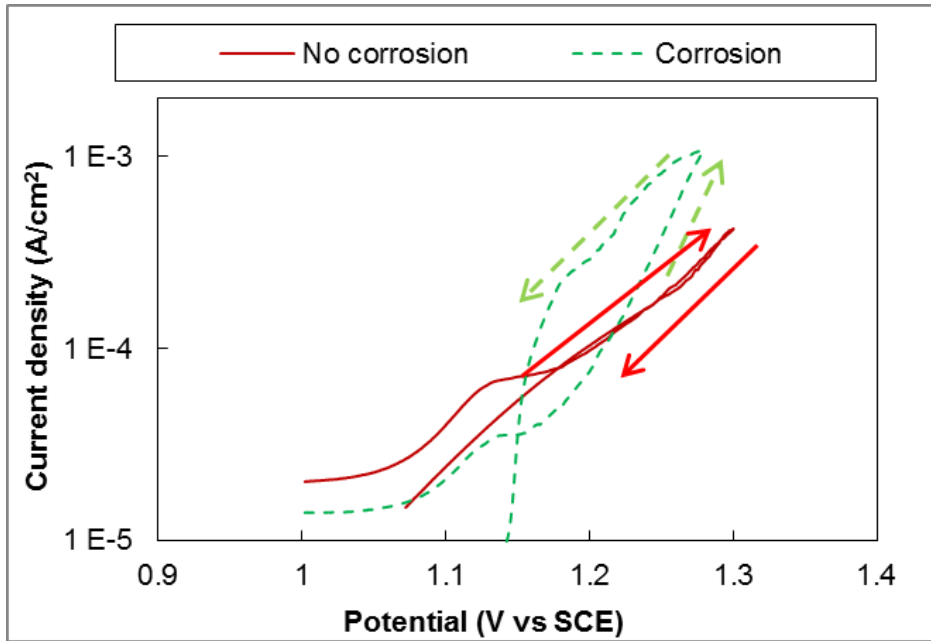


Figure 6.9: Cyclic curves showing corrosion (green) and no corrosion (red)

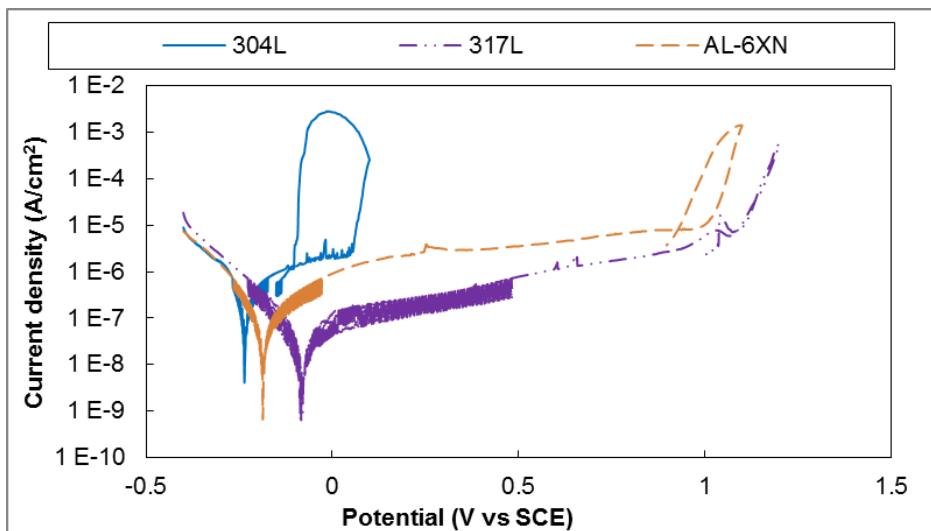


Figure 6.10: Cyclic polarization of 304L, 317L, and AL-6XN at 24 °C in aerated 25 wt.% NaCl solution.

6.2.2 Effects of Temperature

A summary of pitting potentials (or oxygen evolution or transpassive dissolution potentials) for each alloy at various temperatures is shown in Figure 6.11. Similar to previous tests and

as expected, 304L and 316L both pit at every temperature tested, while 316L maintains a higher pitting potential than 304L. The pitting potential of both alloys decreases with temperature, which is consistent with trends in literature [122]. Similarly, no conditions were tested that promoted pitting in AL-6XN. However, the potential at which a sharp increase of current density occurs for both 310S and AL-6XN is lower than that of 317L at low temperatures. This is due to transpassive dissolution of chromium from the higher chromium containing alloys, 310S and AL-6XN, while the chromium does not dissolve in such high quantities in 317L, so the alloy appears stable until oxygen evolution begins. Also consistent with prior testing, neither 317L nor 310S pit at lower temperatures, but begin to pit between 24 °C and 50 °C. However, contrary to PREN rankings, 317L began to pit between 30 °C and 40 °C, while 310S remained passive until between 40 °C and 50 °C. At high temperatures, passivity increases with relation to PREN, however the model breaks down at lower temperatures where 310S is more passive than 317L. The higher pitting resistance of 310S over 317L at between 40 °C and 50 °C is likely due to the higher chromium content of 310S. The repassivation potentials, shown in Figure 6.12, follow the same trends as the pitting potentials. Figure 6.13 shows the difference between the repassivation and pitting potentials. Though there is a slight decrease in the difference between pitting and repassivation potentials in 304L and 316L as temperature increases, the trends are not consistent through all temperatures or alloy systems. The difference between pitting and repassivation is expected to decrease based on the assumption of a boundary condition; there is expected to be some temperature at which a given alloy is never passive, where the pitting and repassivation potentials converge. The corrosion mechanism may not remain consistent throughout the temperature range and which a steel remains passive, so the trend may be sporadic.

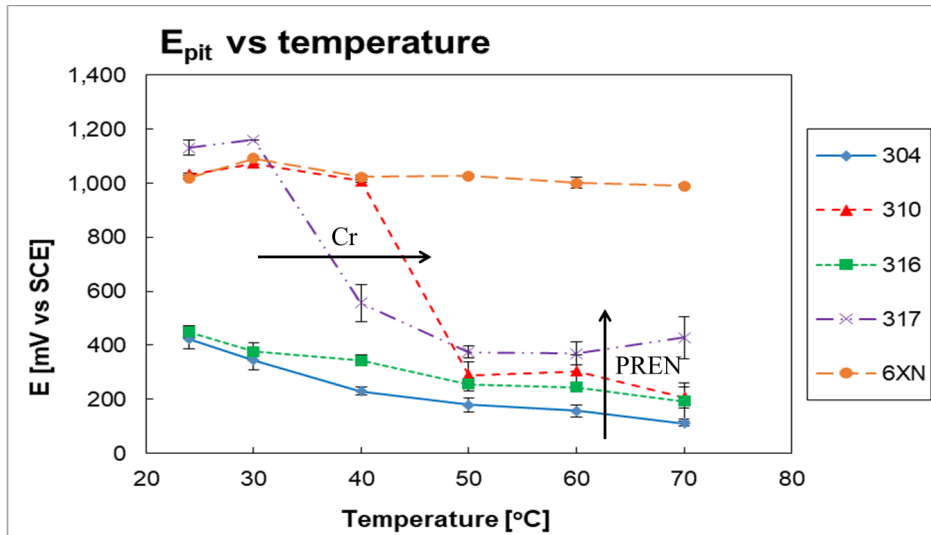


Figure 6.11: Pitting potential or oxygen evolution of each alloy at 24, 30, 40, 50, 60, and 70 °C in aerated 3.5 wt.%. The observed effects of chromium concentration and PREN are noted.

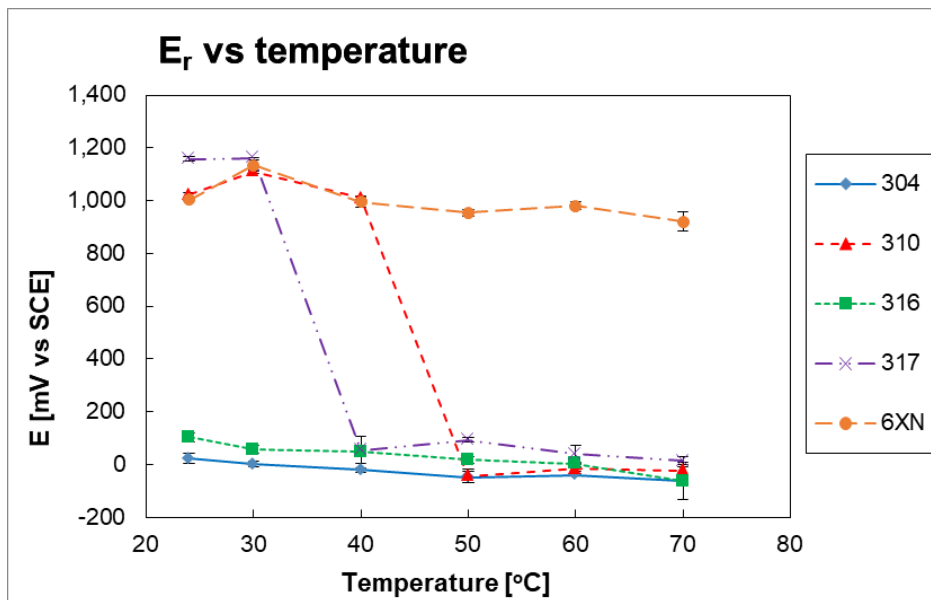


Figure 6.12: Repassivation potential of each alloy at 24, 30, 40, 50, 60, and 70 °C in aerated 3.5 wt.%.

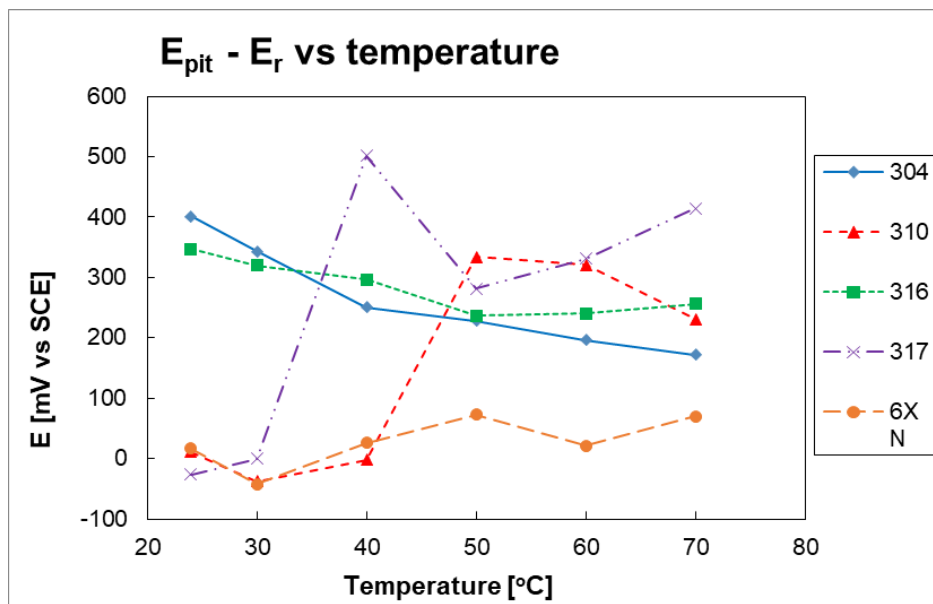


Figure 6.13: Difference between pitting potential or oxygen evolution and repassivation potential of each alloy at 24, 30, 40, 50, 60, and 70 °C in aerated 3.5 wt.%.

The results above have been reconfigured and displayed in Figure 6.14 to illustrate the relationship between PREN and pitting potential. Low PREN alloys, 304L and 316L, pit in every test, however there is a sharp increase of corrosion resistance between a PREN of 24 (316L) and 25 (310S) up to 40 °C. At 40 °C, there is a clear break in the trend where corrosion resistance decreases as PREN increases. At temperatures above 50 °C, there is a linear increase of pitting potential as PREN increases. The linear trend is consistent between 50, 60, and 70 °C tests, indicating that the effect of PREN is temperature-independent if the temperature is above some critical value. If stable pits are able to form, PREN is a valid model; however PREN alone cannot be used to predict the temperature at which an alloy will begin pitting. The lack of predictive power of PREN in some alloy and environment regimes suggests that chromium and molybdenum impact the passive films through different mechanisms.

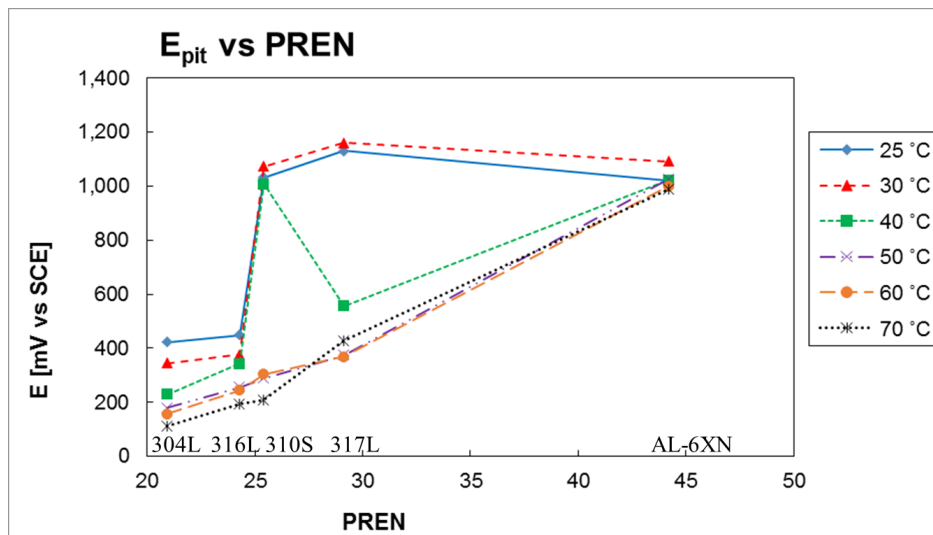


Figure 6.14: Pitting potential or oxygen evolution of each alloy at 24, 30, 40, 50, 60, and 70 °C in aerated 3.5 wt.%. The alloys are ordered by PREN, showing 317L break the trend at 40 °C.

6.3 Discussion

There are many proposed mechanisms by which various elements protect stainless steels, and by which pits nucleate in chloride environments. Though no mechanisms were directly observed, chromium and molybdenum seem to have differing passivation effects since chromium

has a greater impact on an alloy's critical pitting temperature, while molybdenum has a larger impact on pitting potential when stable pits can form. Frankel recently suggested that there are two possible rate controlling steps of pitting, and that the rate controlling step is dependent on the aggressiveness of the solution, as summarized in Figure 6.15 [123]. In his model, the rate controlling step is dependent on solution aggressiveness. It can thus be extrapolated that, for a given environment, the rate controlling process may be alloy dependent, which is probably the reason 310S has a higher corrosion resistance than 317L at 40 °C. Figure 6.16 shows that, while otherwise the curves are superimposable, 310S is susceptible to metastable pitting at 24 °C, while 317L does not appear to have as much passive film breakdown. Though both alloys remain passive, the cause of this passivity appears to be due to different mechanisms that fail at different temperatures.

	Passive film breakdown →	Metastable pitting →	Pit Growth
Less aggressive:	Slow (rate-controlling)	Fast	Fast
More aggressive:	Fast	Fast	Slow (rate-controlling)

Figure 6.15: Rate controlling steps of pitting [123]

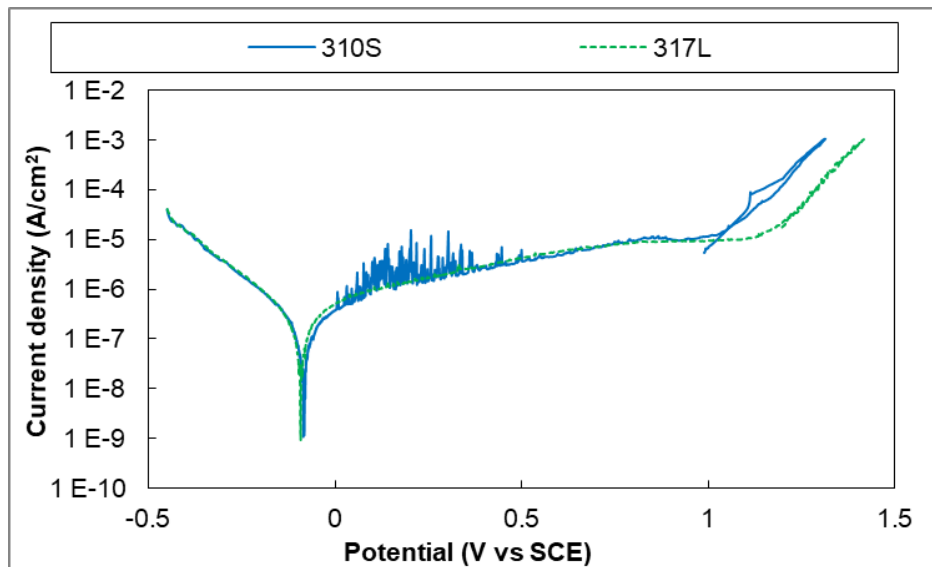


Figure 6.16: Polarization curves of 310S and 317L at 24 °C. 310S shows evidence of metastable pitting while 317L does not.

PREN is a useful tool for estimating pitting resistance, however its applications are limited. There are conditions under which PREN is not predictive, including low temperature

chloride solutions. The breakdown of the model's predictive power is because chromium and molybdenum affect stainless steel through different mechanisms. Each mechanism is impacted differently by various conditions, so a more thorough model must be used to compare alloys across multiple environmental conditions.

It is well established that PREN cannot be used as the sole predictive model of stainless steel corrosion resistance, but it is still ubiquitous in the corrosion industry [94, 98]. The model was developed using a saltwater and ferrocyanide solution, but modern studies tend to use critical pitting temperature in a ferric chloride solution, based on an ASTM standard, to determine pitting resistance [94, 97, 124]. There are limits to the predictive power of PREN, such as extreme alloy chemistries where the impact of alloying elements drift from the expected trends [97]. PREN is also not precise enough to predict comparisons between minute changes within an alloy, but is generally considered sufficient to compare pitting resistance between stainless steel grades [94, 98]. Another potential problem with the simple PREN model is the effect of environment chemistry, since the model is based on specific environment chemistries.

Chromium increases steel passivity while molybdenum decreases active dissolution rate [14, 21, 60]. Molybdenum increases resistance to acidic solutions, but does not increase pitting resistance without the presence of chromium [21, 89]. Chromium and molybdenum have different effects on corrosion resistance and work through different mechanisms, so it can be expected that they have different impacts on corrosion resistance in various environments.

Within the commercial alloys tested, PREN was valid under some conditions, but not all. PREN was able to predict the order of pitting potentials for all alloys that exhibited stable pitting, as expected. However, the critical pitting temperatures measured did not correlate with what PREN predictions. Higher chromium 310S had a higher critical pitting temperature than higher molybdenum (and PREN) 317L. The divergence from PREN was probably because molybdenum is effective at decreasing corrosion in acidic solutions, where the model was developed, so it would have a lower impact than predicted in the neutral solution tested. At low temperatures, chromium imparted a higher pitting resistance than molybdenum, while at higher temperatures, molybdenum was more beneficial. The higher chromium alloy also appeared to undergo more metastable pitting than the higher molybdenum alloy at temperatures where no stable pitting occurred on either alloy. While metastable pitting can be used to determine the corrosion and passivation mechanisms, the experiment was not tuned to observe metastable pitting, so this observed trend is not conclusive.

PREN is not a perfect model, so researchers often dismiss its failings rather than than working to understand them. It was determined that PREN is not a good predictor of corrosion resistance among standard commercial alloys in the very important condition of neutral saltwater. A robust model of pitting resistance would greatly benefit the corrosion community, both in research and materials selection. The PREN model is a widely used, but should be expanded to include other variables, such as pH and environment chemistry.

Chapter 7

Thin Films

The use of metallic thin films is being evaluated for applications including corrosion sensors and protective corrosion resistant coatings. The current understanding of thin film corrosion is not sufficient to relate thin film corrosion of sensors directly to bulk metal corrosion. It is also unclear if thin films can act as protective coatings on metal surfaces. This chapter introduces the methods used to measure thin film corrosion and compare thin film corrosion with bulk metal corrosion. Results comparing the effects of film thickness and substrate conductivity on corrosion are discussed.

7.1 Experimental Materials and Methods

7.1.1 Materials

Corrosion of bulk metals is size-independent, however thickness can change the properties of thin films. The effects of film thickness on corrosion resistance of nanocrystalline metallic thin films is unclear. Most thin film corrosion studies have used relatively thick thin films in the 100-700 nm thickness range [14, 17, 18, 37, 50]. Some studies have focused on thinner films in the 20-100 nm range, in which the grain size tends to be between 50 and 100 nm [16, 33, 125].

Bulk 99.5 % Fe was compared with the films summarized in Table 7.1. All thin films were magnetron sputtered onto silica substrates. Some iron thin films were sputtered on a platinum conduction layer to determine whether the conductivity of the substrate affects

corrosion properties. Samples with a Pt conductive layer required a tantalum adhesion layer between the Pt and silica to prevent spalling.

Fe (nm)	Pt (nm)	Ta (nm)
10	0	15
20	0	0
100	0	0
20	25	15
100	25	15
0	0	15
0	25	15

Table 7.1: Composition and thickness of Fe thin film sputtered on silica substrates. Ta is used as an adhesion layer between the substrate and Fe or Pt layer.

7.1.2 Resistivity

Platinum backings were added to the iron thin films to decrease the resistivity of the system in order to mimic a thin film on the surface of a metal, for applications such as protective coatings. The resistivity of each film was measured using a 4-point resistivity probe to ensure that the conductive Pt layer decreased film resistance. The average for each film type was taken for 6 replicates of each Fe and Fe+Pt+Ta film.

The resistivity of 6 each of 304L and 316L stainless steel thin film samples were measured using the same technique as with the iron thin films to allow a deeper comparison between the various alloy systems.

7.1.3 Potentiodynamic Polarization

Polarization curves were scanned cathodic to anodic at 1 mV/s in aerated 3.5 wt% NaCl solution at 24 °C. Some studies in the literature used faster scan rates (5-10 mV/s) for thin films to ensure the scan was completed before the entire film dissolved, but others used slow scan rates (0.33 mV/s) to improve accuracy [13, 14, 24, 25, 50]. The scan rate of 1 mV/s was chosen because it is within the range of what has been used in literature and is consistent with tests in Chapter 6. After polarization, sample surfaces were imaged using a Zeiss Axio

optical microscope. Bulk Fe samples were wet ground using 500 grit SiC paper, while the thin films were all left in the as-received condition.

7.1.4 SVET

SVET measurements on iron thin film surfaces were carried out using the Pt microelectrode immersed in an electrolyte drop on the sample surface without polarization. Repeated line scans were measured to observe the change across the film over time. Line scans were 2 mm in length with a step size of 50 μm , measuring speed of 25 m/s, time constant of 1 s, and measure delay of 2 s [117]. A drop of either deionized (DI) water, tap water, or 3.5 wt.% NaCl solution, naturally aerated in the atmosphere, was added between the Pt microelectrode and the sample surface immediately before the measurement began. All non-polarized SVET tests were measured at 24 $^{\circ}\text{C}$. In tests using the SVET droplet setup, the microelectrode was approximately 20-30 μm from the sample surface [126]. Tests using the drop with PTFE tape or filled environmental chamber for polarization used a microelectrode distance of approximately 10-20 μm from the sample surface.

7.2 Results and Discussion of Fe and Fe-Pt Films

7.2.1 Resistivity

The measured resistivity of each thin film compared to literature bulk metal resistivity values is shown in Figure 7.1 [127]. The resistivity values measured here are similar to literature results, which follow the trend shown in Figure 7.2 [16]. This trend has also been observed in gold thin films, so it is probably a geometrical effect rather than an alloy chemistry-specific effect [128]. Because metallic thin films tend to have similar thickness-dependent resistivity trends, laminating two dissimilar metals should not have any adverse effects on film electrical response. The measured resistivity values are a valid comparison between sample types, but cannot necessarily be used to determine the exact resistivity values during polarization or SVET testing. It has been shown that the resistivity of thin films can change depending on the environment, shown in Figure 7.3 [17].

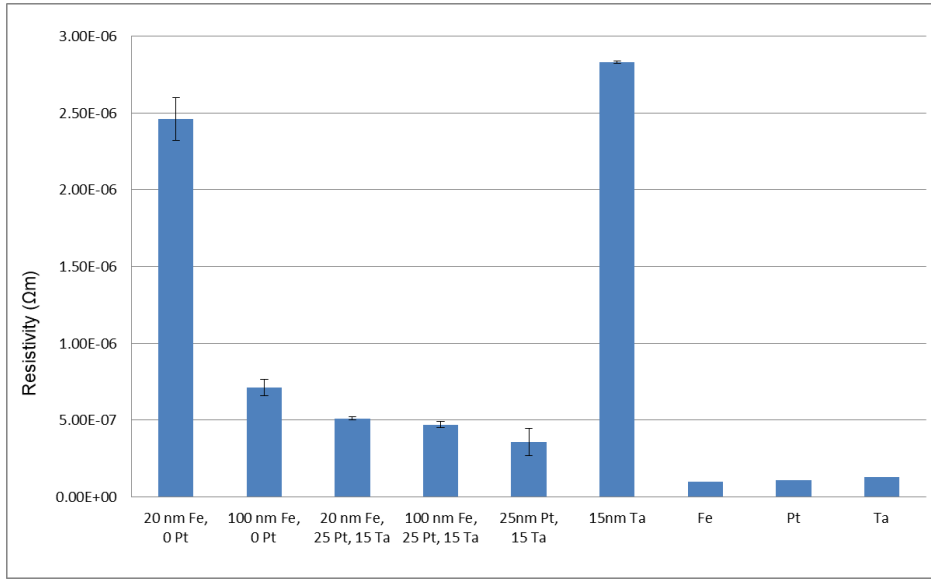


Figure 7.1: Resistivity measurements of Fe thin films and Pt+Ta backed Fe thin films compared to literature values of bulk Fe, Pt, and Ta resistivities [127].

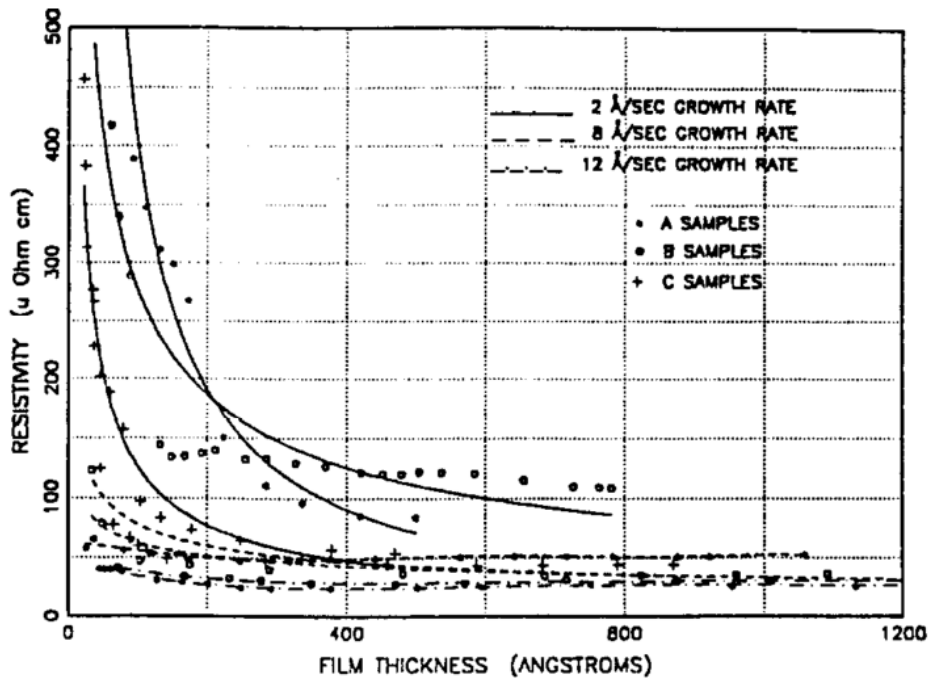


Figure 7.2: Resistivity of iron thin films [16].

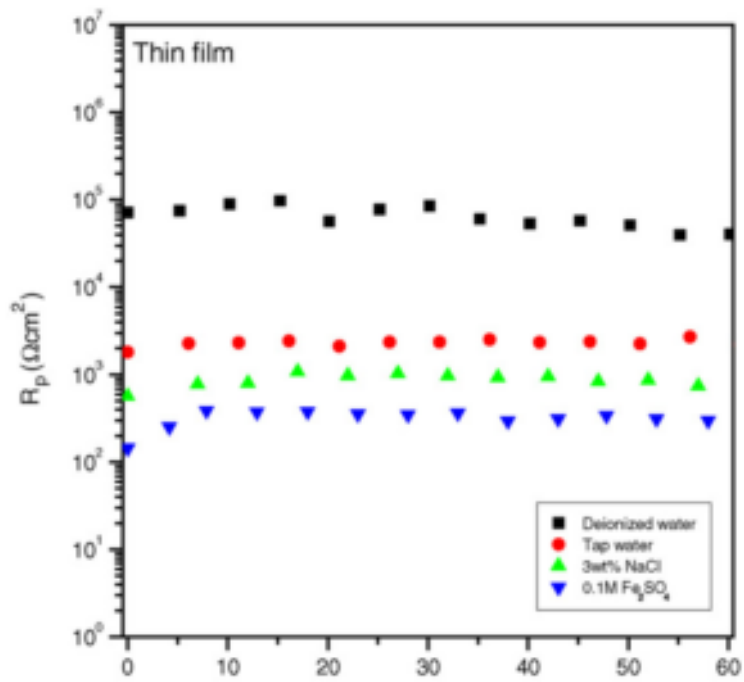
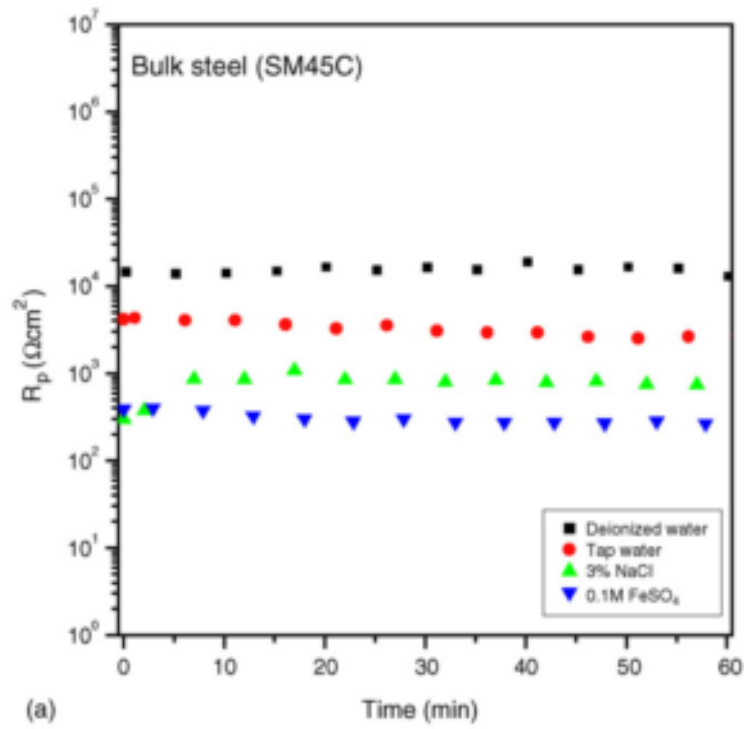


Figure 7.3: Resistivity of bulk steel and 600 nm thin film steel in different electrolytes at 25 °C [17].

7.2.2 Polarization

Potentiodynamic polarization curves of various iron thin film thicknesses, Figure 7.4, show that increasing Fe film thickness increases the corrosion current (I_{corr}) and decreases the corrosion potential (E_{corr}). As iron films increase in thickness, their corrosion resistance continuously decreases over the thicknesses measured. The effect of a platinum conductive layer is shown in Figure 7.5. The conductive layer does not affect the E_{corr} , but does increase the I_{corr} . The E_{corr} of a system appears to be established by the iron film thickness, with thinner films being more noble than thicker films. The same E_{corr} measured in iron thin films with and without platinum layer also indicates that only the iron of the thin film was corroding at the E_{corr} and that the iron did not seem to form a galvanic couple with Pt underlayer. However, the rate of corrosion may be based on electron mobility within the film, resulting higher I_{corr} in lower resistivity films. The noise in the 10 nm iron film with a 15 nm tantalum adhesion layer, Figure 7.4, is probably due to localized corrosion of the film reaching the tantalum layer, causing rapid oxidation and passivation of the tantalum. There might be an effect of galvanic coupling between the iron and tantalum as well, but it is unclear as to why a galvanic couple between tantalum and iron would cause iron corrosion while a platinum-iron couple does not. All thin film samples were tested in the as-received condition, which was a mirror finish with no noticeable scratches or pits. The smooth surface likely improved their corrosion resistance compared to bulk iron, which was ground to 500 grit, but all thin film samples are directly comparable.

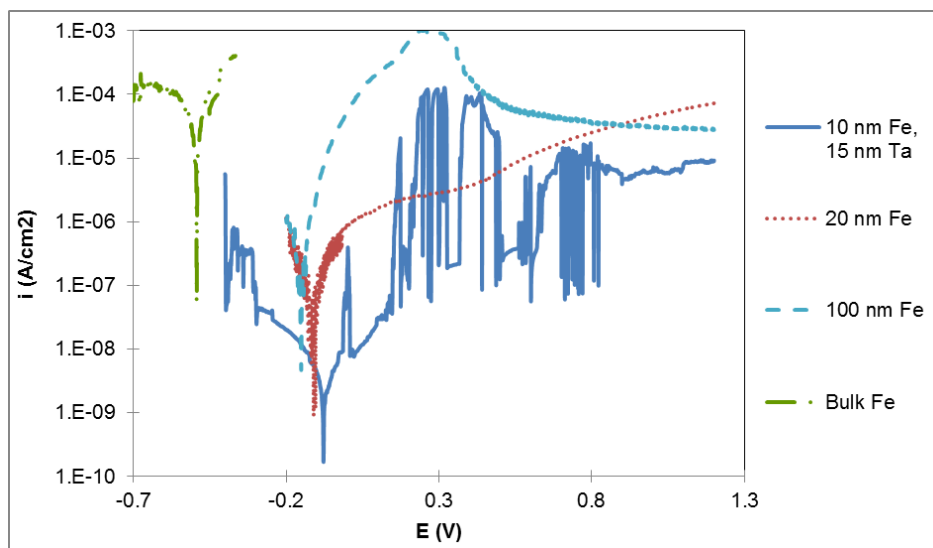


Figure 7.4: Polarization curves of Fe bulk and thin films of various thickness in aerated 3.5 wt.-% NaCl at 24 °C.

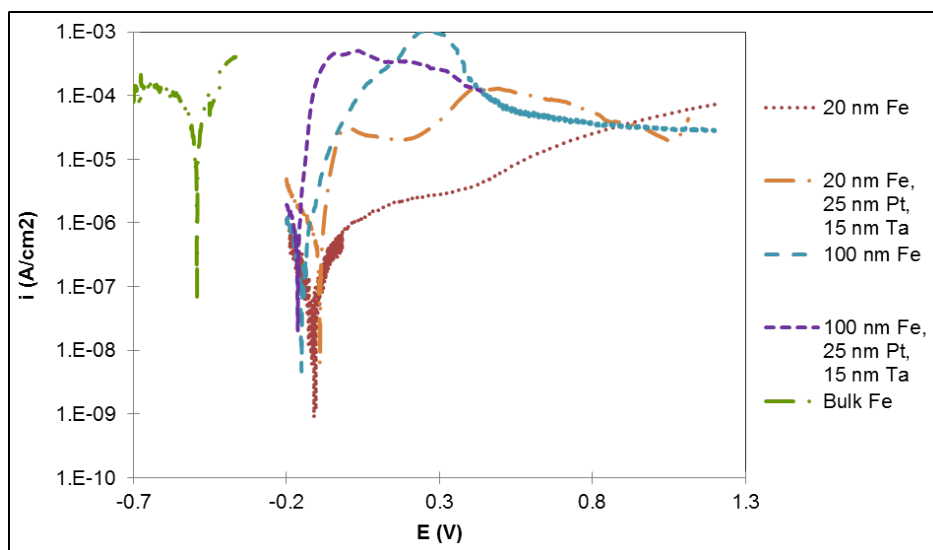


Figure 7.5: Potentiodynamic polarization curves of Fe thin films of varying thickness with and without Pt conductive layers in aerated 3.5 wt.-% NaCl at 24 °C.

The E_{corr} and resistivities of bulk iron, 20 nm and 100 nm iron films on silica, and 20 nm and 100 nm iron films with platinum backings are shown in Figure 7.6. E_{corr} does not scale directly with resistivity. This is clear in the case of the 20 nm films where the two 20 nm Fe films have similar E_{corr} , but their resistivities differ significantly. There is a large change in

E_{corr} due to the thickness of the iron film, but this change is not due to lower resistivity of thicker films.

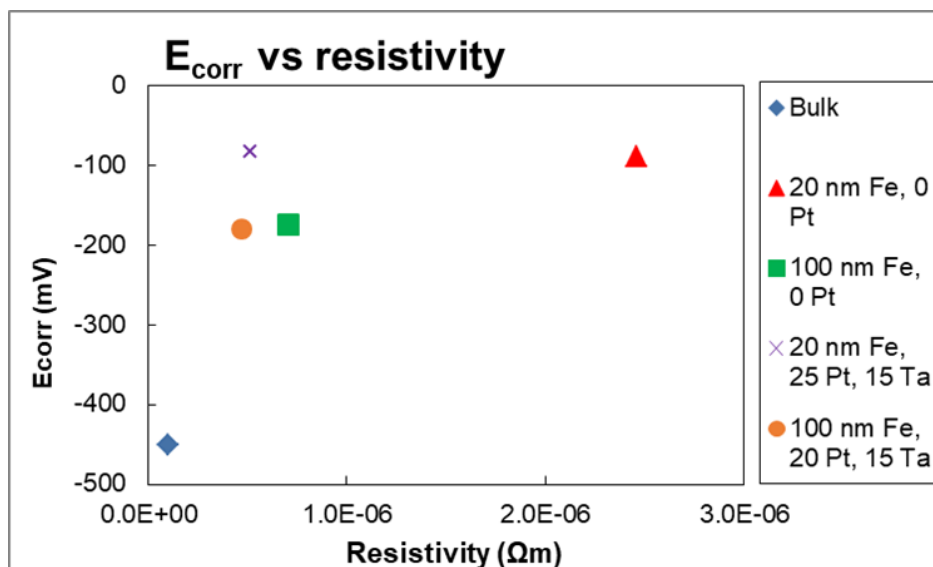
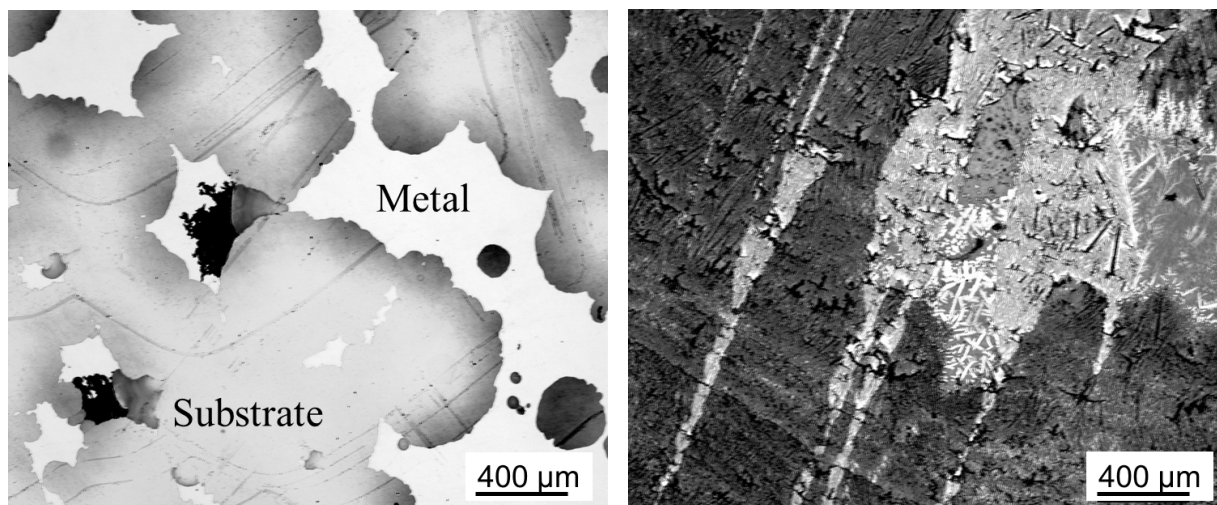


Figure 7.6: Relationship between E_{corr} and resistivity of bulk Fe and Fe thin films of varying thickness with and without Pt conductive layers in aerated 3.5 wt/% NaCl at 24 °C.

Light optical micrographs of 100 nm iron thin films, with and without a platinum conductive layer, after potentiodynamic polarization are shown in Figure 7.7. Samples with iron sputtered directly onto silica substrates show islands of residual metal surrounded by regions of exposed silica. The metal appears to have locally corroded until the substrate became exposed, at which point the corrosion expanded outward radially, as has been seen in similar thin film systems [16]. There was no observable color change on the iron samples sputtered on silica. The corroded region of the platinum backed samples, however, turned gold, similar to the bulk iron. The platinum conductive layer changed the corrosion behavior by preventing the localized corrosion observed in the iron thin films without platinum. Because the electrons were able to travel through a different path during corrosion of the platinum backed samples, the corrosion mechanism was altered from the pure iron thin film samples, allowing the more conductive film to act more like bulk iron.



(a) 100 nm Fe on silica substrate

(b) 100 nm Fe with 25 nm Pt and 15 nm Ta on silica substrate

Figure 7.7: LOM images of samples after polarization.

7.2.3 SVET Environment Composition

SVET was used to observe open circuit corrosion across a sample by using a Pt vibrating microelectrode to measure the local change in potential across ionic currents above the metal surface. Figure 7.8 shows that many of the peaks and troughs measured were maintained spatially throughout the duration of the test of 20 nm iron on a silica substrate in tap water. This implies that the local anodes and cathodes were at distinct points on the metal surface. However, some of the features wax and wane throughout testing, suggesting that these regions of corrosion were either metastable or that the metal corroded through to the substrate, halting further corrosion in that region. The effect of electrolyte solution is shown in Figure 7.9. At time $t=0$, there were peaks and troughs in the line scan. The higher potential signals (peaks) correspond to the cathodic areas, and the lower potentials (troughs) correspond to anodic regions. With time, the peaks and troughs maintained spatially, but the overall signal decreased for both the cathodic and anodic regions. Tap water (Figure 7.9(a)) showed higher potentials at $t=0$ with peaks and troughs, followed by a decrease in potential over time, while maintaining the initial anodic and cathodic positions. In contrast, salt water (Figure 7.9(b)) showed significant peaks and troughs at $t=0$ followed by an increase and leveling off of the signal. DI water (Figure 7.9(c)), had initial peaks and troughs with diminishing extrema, as well, but the overall signal did not significantly increase or decrease.

The trends across all solutions were similar between 20 nm and 100 nm iron sputtered on silica. The 20 nm iron with platinum conductive layer also showed similar trends to the iron samples without platinum in DI water and tap water. However, in salt water, the 20 nm iron sputtered on a platinum conductive layer is similar to the DI water tests of iron thin film without platinum, with larger initial peaks that diminished over time, but with no overall change across the sample at longer times, shown in Figure 7.10.

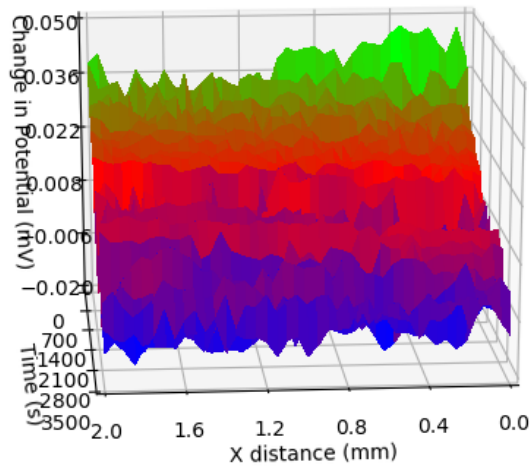
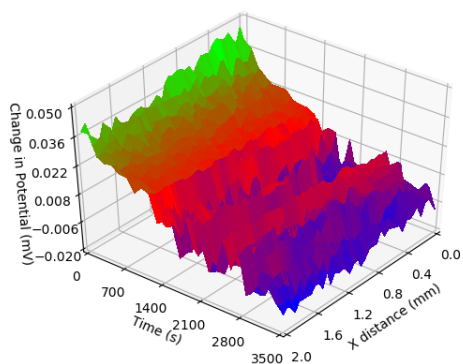
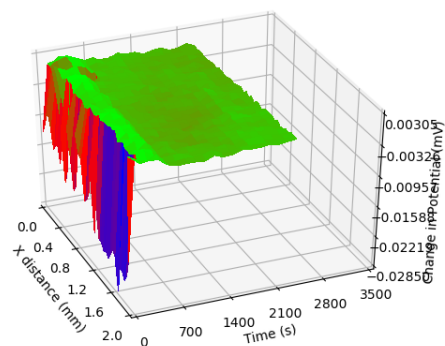


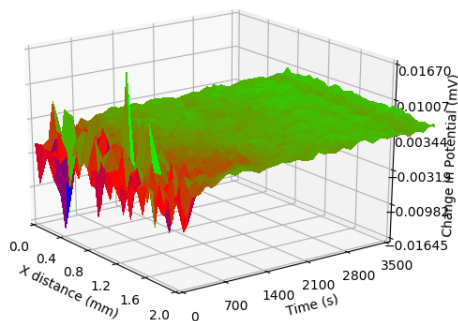
Figure 7.8: SVET measurement of 20 nm iron on a silica substrate in tap water at 24 °C.



(a) Tap water (same results as shown in Figure 7.8)



(b) 3.5 wt.% NaCl



(c) DI water

Figure 7.9: SVET measurement of 20 nm iron on a silica substrate at 24 °C.

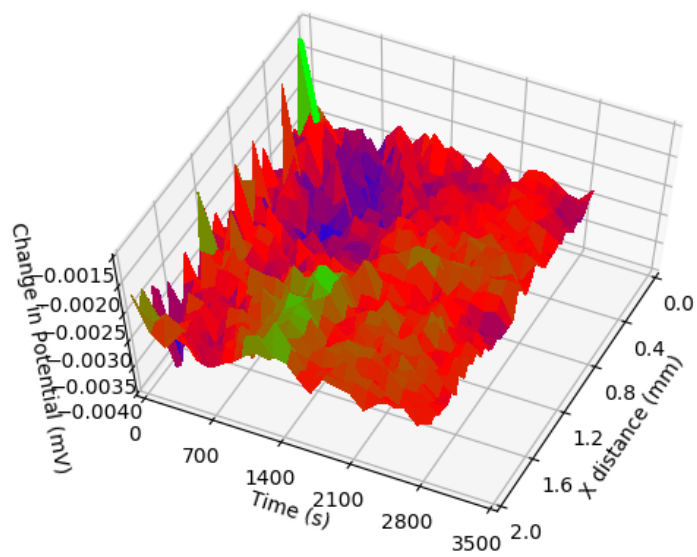


Figure 7.10: SVET measurement of 20 nm iron with platinum conductive layer on a silica substrate in 3.5 wt.% NaCl at 24 °C.

The peaks of SVET measurements correspond to cathodic regions and the troughs correspond to anodic regions, so the difference in potential between the peaks and the troughs should be an indicator of corrosion rate [22]. A summary of the difference between minimum and maximum potentials for each sample under each condition is shown in Figure 7.11. There appears to be some correlation between solution and ionic flow through the solution, though only one test was run for each system, so the results are still preliminary. It should also be noted that the sample-microelectrode distance was constant between different solutions for a given sample, but only approximate between samples. The ionic current, as measured by the potential difference, appears to decrease as ionic concentration within the solution increases. This could be an effect of the corrosive nature of the solution, with NaCl solution being the most corrosive solution and deionized water being the least. However, the measurement could also be influenced by the conductivity of the solutions, resulting in different potential differences for the same ionic current. Between the samples, the potential difference loosely correlates with film resistivity, with 20 nm iron with no platinum having the least corrosion and 100 nm iron with platinum corroding the most.

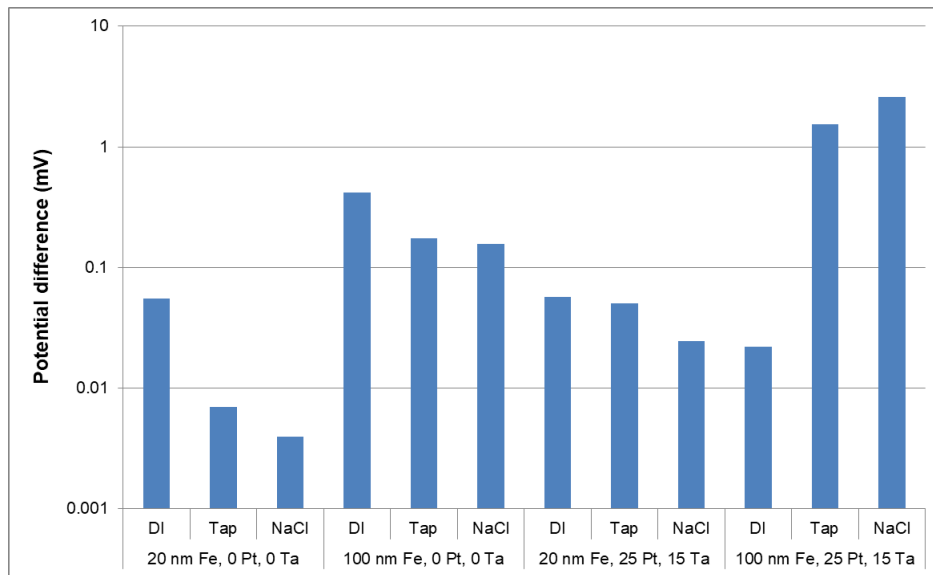


Figure 7.11: Difference between minimum and maximum potentials in SVET measurements in each condition.

Resistivity measurements showed that the platinum backed films were less resistive than iron films sputtered on silica, which may allow for faster corrosion rates. LOM images showed the non-platinum backed iron films corroded to the substrate, leaving islands of uncorroded

metal, while the platinum backed films left a layer of golden corrosion product. SVET results supported these results by demonstrating a different corrosion process between the films with and without a platinum conductive layer in NaCl solution. While the nanocrystalline structure of Fe thin films improves corrosion resistance over bulk coarse grained iron, the conductivity of these systems also plays a role in the corrosion mechanism in chloride containing aqueous environments.

7.2.4 Submerged SVET

Hydrophobic PTFE tape was used to prevent the formation of a metal-water-air boundary, creating a fully submerged test environment. The SVET results from Section 7.2.3 were influenced by the metal-water-air interface, so fully submerged tests are closer analogs to the polarization tests in Section 7.2.2. SVET results from each iron thin film system are shown in Figures 7.12-7.15. During these experiments, the microelectrode was closer to the sample surfaces than in Section 7.2.3, resulting in different morphologies that are probably closer to the actual morphology of the corroding surface. Each sample appeared to have large anodic and cathodic regions at early times, indicating corrosion, and a more level system at later times, indicating a decrease in corrosion rate. In the 20 nm and 100 nm films on silica, a clear localized anode is present at the initiation of the measurement. At later times, the anodic region moves outward, which can be seen in the form of diagonal low regions in the SVET map. Because the corrosion reaches the substrate, anodic regions in the insulating substrate do not reappear at later times. The 20 nm and 100 nm iron films with platinum conductive layers show larger anodic regions that wax and wane in size over time rather than consistently moving outward. Anodic regions also reappear at later times on the platinum backed films, probably because the iron corrosion did not reach the substrate. The difference in corrosion morphology between otherwise identical films with and a without conductive backing measured using SVET indicates that the corrosion mechanism is dependent on substrate conductivity.

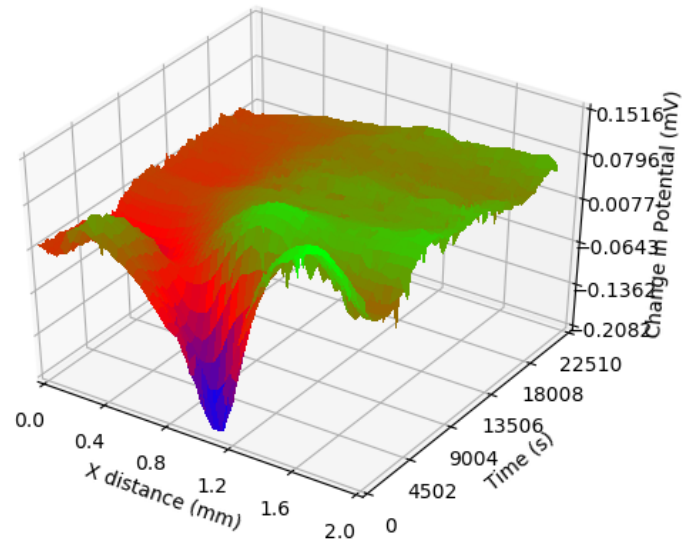


Figure 7.12: SVET measurement of 20 nm iron without platinum conductive layer on a silica substrate in 3.5 wt.% NaCl at 24 °C.

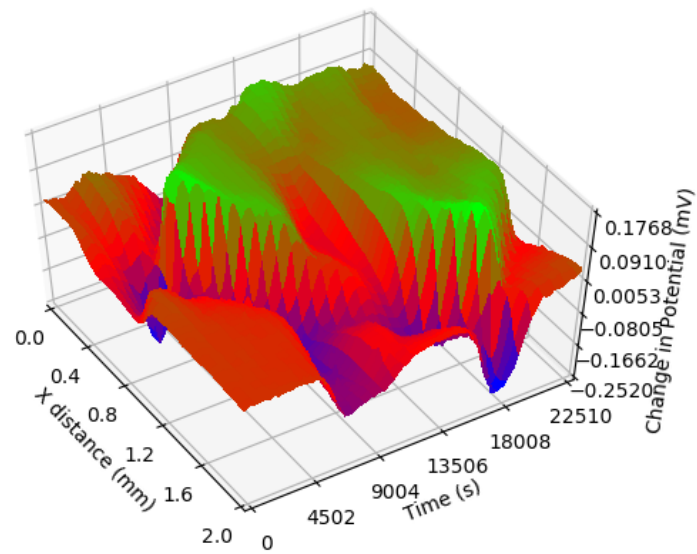


Figure 7.13: SVET measurement of 100 nm iron without platinum conductive layer on a silica substrate in 3.5 wt.% NaCl at 24 °C.

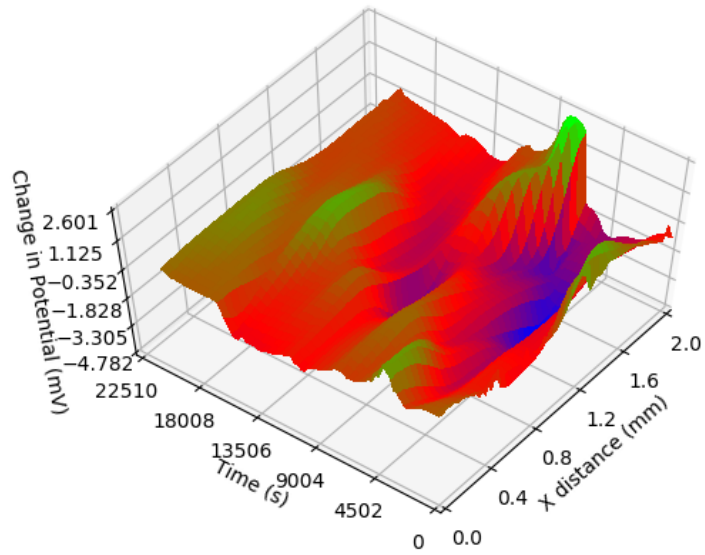


Figure 7.14: SVET measurement of 20 nm iron with platinum conductive layer on a silica substrate in 3.5 wt.% NaCl at 24 °C.

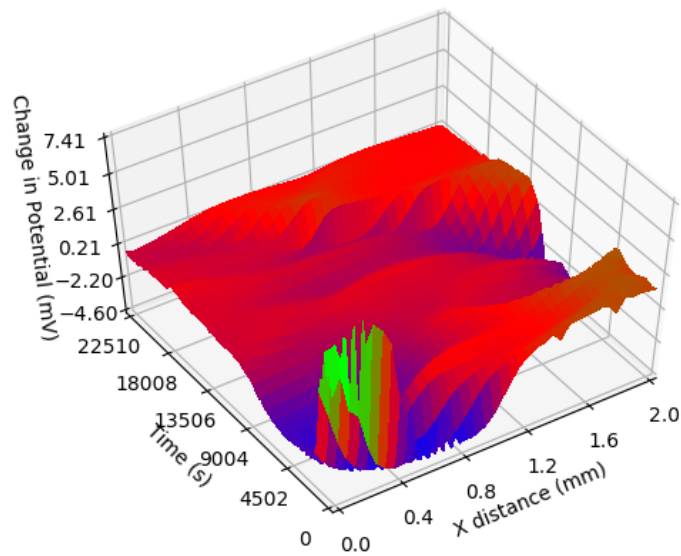


Figure 7.15: SVET measurement of 100 nm iron with platinum conductive layer on a silica substrate in 3.5 wt.% NaCl at 24 °C.

The relative corrosion reaction rates, quantified by the difference between anodic and cathodic potentials, is shown in Figure 7.16, though the same caveats should be employed as noted in Section 7.2.3. The potential difference correlates with sample resistivity, supporting the hypothesis that the higher resistivity of thinner films leads to higher corrosion resistance. However, Figure 7.17 shows that the measured corrosion rates do not correlate directly with total sample resistivity. Corrosion rate increases significantly with the addition of a conductive backing rather than increasing consistently with lower total resistivity. Substrate conductivity appears to have a higher impact than film resistivity on the relative corrosion reaction rate.

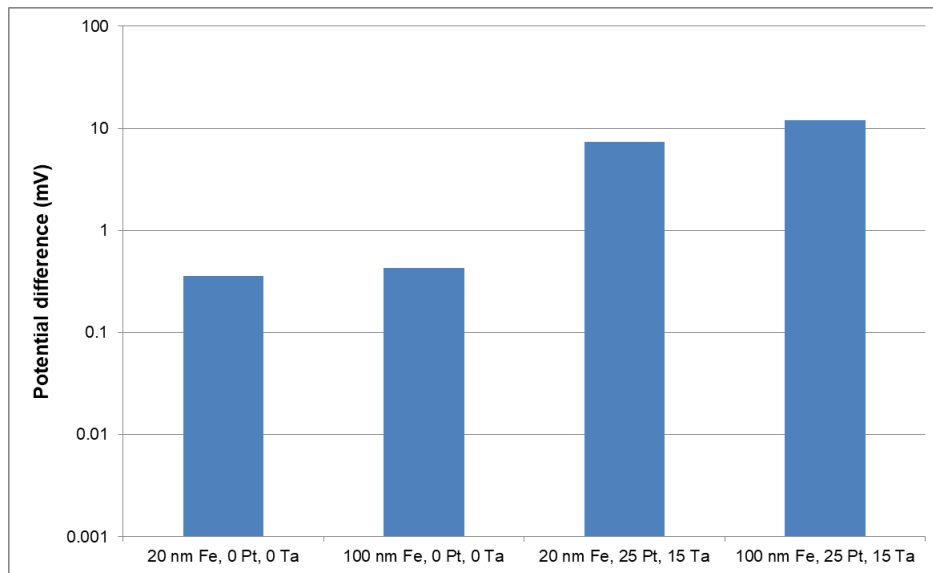


Figure 7.16: Difference between minimum and maximum potentials in SVET measurements in each condition.

SVET results show that iron thin films sputtered on insulating films undergo localized corrosion in the NaCl solution while iron thin films sputtered on conductive substrates undergo general corrosion. These results are consistent with LOM results of polarized thin film. While total film resistivity may play a role in thin film corrosion, the conductivity of the substrate appears to have a larger impact on corrosion rate and mechanism.

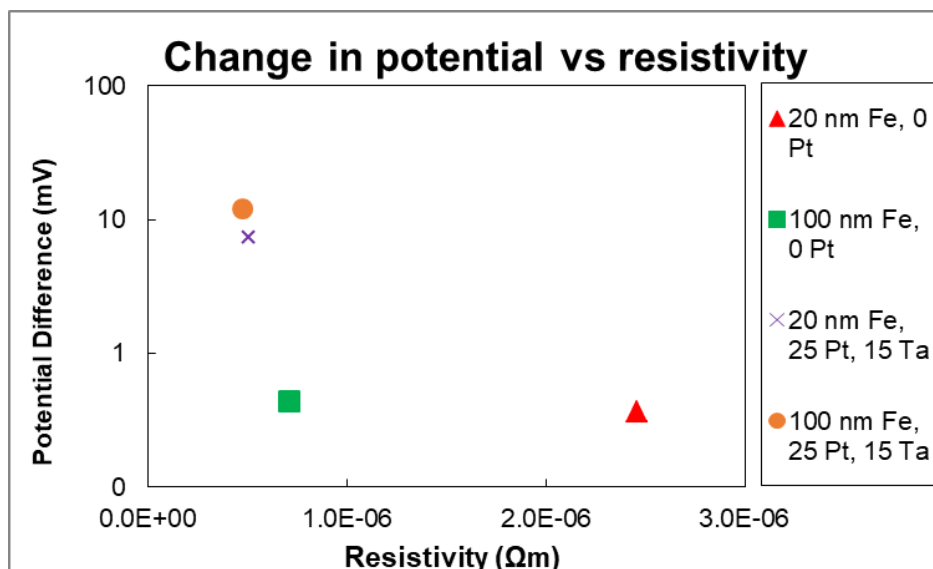


Figure 7.17: Relationship between total change in potential in SVET assay and resistivity of Fe thin films of varying thickness with and without Pt conductive layers in aerated 3.5 wt/% NaCl at 24 °C.

7.3 Discussion

Magnetron sputtered metallic thin films tend to be nanocrystalline, resulting in very high grain boundary surface areas compared to bulk cast metals [24, 25, 33]. These films have been found to have no preferential orientation, but columnar structures have been observed [14, 37, 40]. The high grain boundary surface areas lead to higher diffusion rates through the metal, which amplify the corrosion behavior. In non-passivating conditions, such as copper in salt water, this results in increased corrosion rates [25]. Copper thin films exhibit higher current densities compared to bulk copper, but the polarization responses are otherwise similar. The E_{corr} of copper thin films in salt water are the same as the E_{corr} of bulk copper, and the shape of polarization curves are similar as well. Conversely, stainless steel thin films tend to be more passive than bulk stainless steels. The E_{corr} and passive current densities tend to be similar, but thin films tend to have higher pitting potentials [24, 33]. Thin films tend to be polycrystalline with no texture, so the corrosion properties have been largely attributed to differing diffusion rates rather than structural differences between thin films and bulk metal [13, 14, 19]. Decreased size and number of inhomogeneities has also been

shown to affect thin film corrosion in the case of stainless steels, but may not be as important in non-passivating systems[12].

This work concentrated on iron thin films, which were found to be more corrosion resistant than bulk iron in salt water. Thinner films were found to be more corrosion resistant, as determined by their increased E_{corr} and decreased I_{corr} as thickness decreased. Though this does not follow the same model proposed for other non-passivating metals, the results were consistent with literature results for iron and carbon steel thin films [13, 23]. However, there are many variables that were not accounted for, such as substrate or deposition parameters, so the results could not be compared directly. Unlike the cases of copper and stainless steel, the polarization curves of iron thin films do not follow the same trends as in bulk iron. There is no consensus on the mechanism of iron thin film corrosion, but these results show that the corrosion properties are related to film thickness.

Substrate properties, such as surface roughness, have been shown in the literature to affect the corrosion properties of carbon steel thin films [13]. The effect of surface roughness was attributed to introducing defects to the surface of the metal film, resulting in localized corrosion. This work demonstrated that substrate conductivity is another factor that can impact thin film corrosion by directly comparing the same film on different substrates under comparable conditions using the same methodology. Conductive substrates increased I_{corr} , but did not have a significant influence on E_{corr} for both 20 nm and 100 nm iron thin films. Iron thin films sputtered directly onto silica glass substrates (insulating) appeared to undergo localized corrosion, resulting in shiny metallic regions and bare substrate regions in 20 nm and 100 nm films. The localized nature of thin film corrosion has been seen in the literature in carbon steel thin films sputtered on glass [13]. Microscopy results were consistent with SVET results that showed a localized anode that expanded outward over time, resulting in original anodic region losing its anodic character. Though the corrosion appears localized, it is unclear if there is a protective passive film that prevents general corrosion. The corroded surface of iron thin films sputtered onto platinum coated substrates (conductive) were different in appearance to the iron films on insulating substrates. The conductive-backed corroded films were gold in color and appeared rough, similar to corroded bulk iron (rust). The platinum substrates were not exposed, nor were there visible regions of uncorroded iron metal; there were no shiny, metallic features visible on the corroded surfaces of either 20 nm or 100 nm platinum-backed films. SVET results supported the microscopy results, showing large, diffuse anodic regions that did not expand outward over

time. Though the initial local anodes faded over time both on samples with and without conductive backings, the anodic region did not reappear on the films without platinum (because the metal was completely removed), while the anodic regions reappeared on the platinum-backed films. Both film thickness and conductive backings affect film resistivity, but neither corrosion potentials nor the magnitude of SVET results scaled directly with total film resistivity. Rather, the impact of film thickness and substrate conductivity appear to be partially independent.

SVET has been used in studies in the literature, but it is still an underutilized instrument whose use in these investigations has not been fully explored [22, 126]. The evolution of corrosion over time has been studied using SVET mapping techniques, but this has been limited to long times and few time-points due to the limitations of 2-dimensional mapping techniques [22]. Thus, SVET has historically not been used extensively in quickly changing conditions. The line scan method developed in this work facilitated a compromise between measuring spatial and temporal information. Small time steps enabled monitoring the fast corrosion process of iron while the line scans illustrate the growth or motion of corrosion. Though this innovative approach is promising, only one assay was conducted under each condition, so the repeatability is unknown. The SVET results were consistent with other techniques, so the results appear reasonable, but further trials must be completed before the results can be considered fully quantitative. Similarly, the features on the corroded surfaces were much smaller than the 2 mm line scan area, but the results must be repeated to ensure the area is representative of the corrosion processes that occur on iron thin films. When this approach has been validated, it will provide a powerful tool for investigating the progress of corrosion under different conditions.

Chapter 8

Slow Strain Rate Testing

Stress corrosion cracking causes premature part failure of austenitic stainless steels when exposed to chloride environments. Because it is a complicated phenomenon, there are many methods to measure and observe SCC initiation and growth. It has been shown that cyclic loading can be used to control the corrosion mechanism, but less work has concentrated on monotonic loading [74]. This chapter describes the SSRT method with which SCC can be measured and controlled, in an attempt to develop a model system in which various alloys and environmental conditions can be isolated, tested, and analyzed individually, as well as results obtained using that method approach.

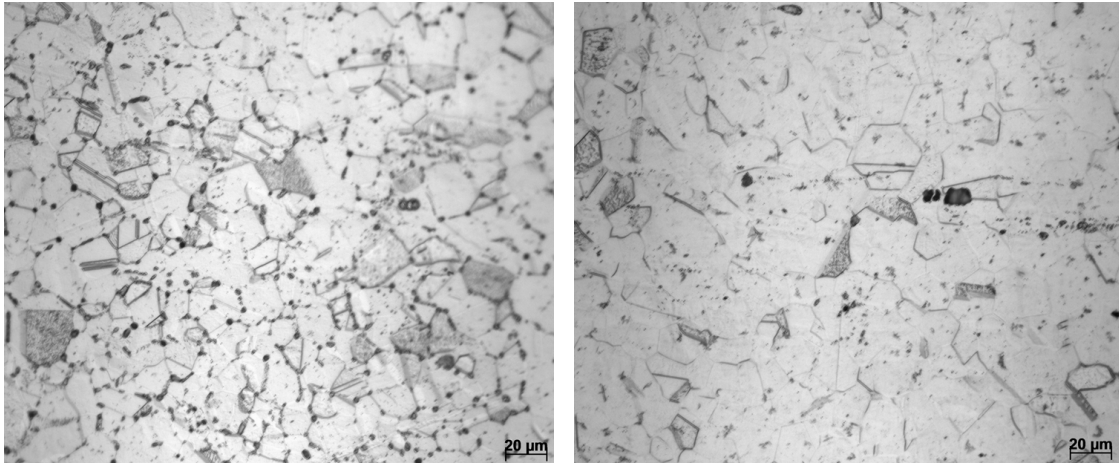
8.1 Experimental

8.1.1 Preliminary Tests: Effect of Specimen Geometry

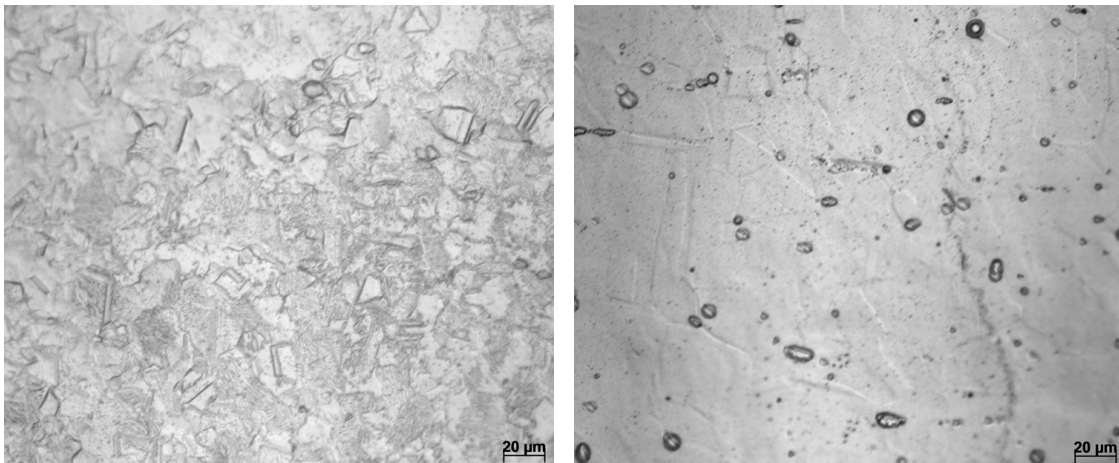
A set of preliminary tests was conducted to develop the SSRT method. The alloys shown in Table 8.1 were chosen due to their generally increasing chromium, nickel, and molybdenum contents and commercial availability. Each alloy was provided as mill annealed 1.5 mm thick sheet from ATI's Brackenridge plant. Microstructures of the as-received mill annealed materials are shown in Figure 8.1. All testing was in the as-received condition.

Alloy	C	Cr	Ni	Mo	N
304L	0.029	18.03	8.03	0.35	0.07
316L	0.021	16.61	10.03	2.02	0.05
904L	0.010	20.02	24.18	4.29	0.05
AL-6XN	0.016	20.53	23.95	6.19	0.22

Table 8.1: Alloy chemistry for EC 1 tests. Alloy compositions in weight percent.



(a) 304L



(b) 904L

(c) AL-6XN

Figure 8.1: LOM of microstructures of each alloy.

Mechanical testing was conducted in air and in an aqueous environment with tensile samples of the three different geometries shown in Figure 8.2. The notches act as stress

concentrating features, qualified by triaxialities. Triaxiality, η , is a way of quantifying stress state, which is a function of loading type and specimen geometry, Equation 8.1, based on the hydrostatic stress, σ_m , and Von Mises equivalent stress σ . Triaxiality of a round bar can be analytically calculated using Equation 8.2, where a is notch length and R is notch radius [129]. Triaxiality can also be used to describe loading directions, where 0 is a shear load, negatives are compressive, and 1/3 is uniaxial tension of a round bar, but all experiments discussed here employed uniaxial loading, so only triaxialities above 1/3 were tested. High triaxiality indicates a notch, which acts as a stress concentrator. Although the equation used is for round specimens, it can be used to estimate differences in triaxiality in flat specimens as well [129]. The triaxiality of the flat samples was approximately 0.33, the wide notch was 0.65, and the sharp notch was 2.11. These values were chosen to enable measurements over a wide range of triaxiality while maintaining uniaxial loading and relatively simple sample geometries. The specimens were machined entirely using computer numerical control (CNC) milling, except for the sharp notch which required wire electric discharge machining (EDM). The coupons were fixed to the test frame through a pin-loading clevis to enable the use of EC 1.

$$\eta = \frac{-\sigma_m}{\sigma} \quad (8.1)$$

$$\eta = \frac{\sqrt{3}}{3} \left[1 + 2 \ln \left(1 + \frac{a}{2R} \right) \right] \quad (8.2)$$

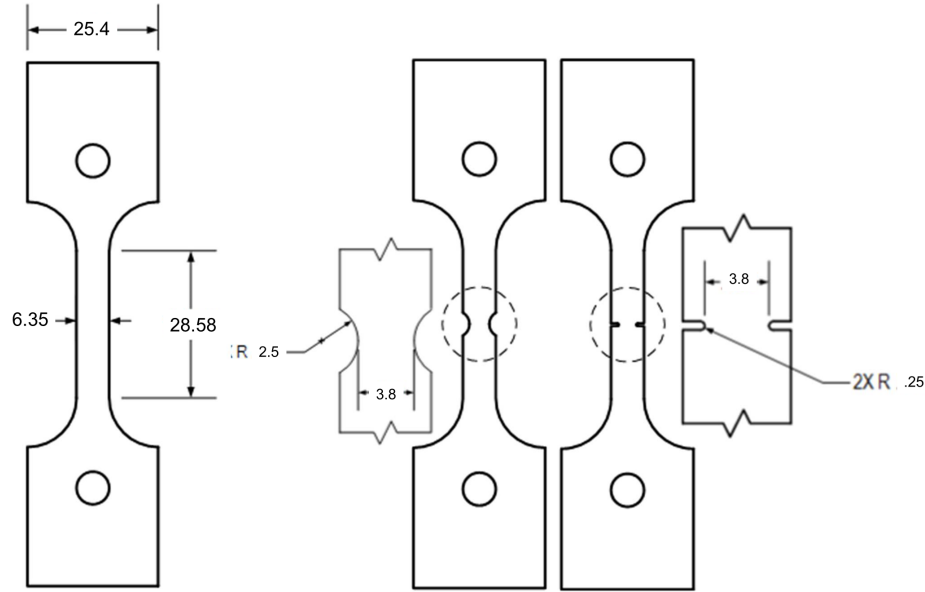


Figure 8.2: Flat tensile specimens of varying triaxiality (measurements in mm). Triaxialities of the un-notched flat samples was 0.33, the wide notch was 0.65, and the sharp notch was 2.11

For each alloy, three specimens of each geometry were strained at a constant extension rate of 5×10^{-4} mm/s (strain rate of 1.75×10^{-5} s $^{-1}$) to failure in air at 24 °C and three were tested in a heated aqueous environment. The extension rate was based on the acceptable strain rates for SSRT in ASTM standard G129 of 7.94×10^{-5} s $^{-1}$ - 4.47×10^{-8} s $^{-1}$ [130]. The aqueous tests were held at 70 °C in a 3.5 wt% NaCl solution. There was no electric polarization in any condition.

The fracture surfaces of 304L and AL-6XN flat samples were observed to determine the mode of failure.

8.1.2 Effects of Polarization and Environment

The the clevis-loading environmental chamber used in preliminary tests, EC1, could not be used to test polarized conditions, so, as described in Sections 5.2.4 and 5.2.5, experimental setups were developed to incorporate sample polarization in various environments. The alloys tested are shown in Table 6.1, and sample geometry is shown in Figure 8.3. Stress-strain curves were recorded in air for each alloy for comparison with corroded samples. 304L samples were polarized at 0.35 V (vs. SCE) (above the pitting potential) for 2 minutes

and dropped from 0.35 V to 0.10 V (above the repassivation potential) in 3.5 wt.% NaCl solution at 24 °C at an extension rate of 5×10^{-4} mm/s (strain rate of 2.5×10^{-5} s⁻¹). For comparison, AL-6XN was potentiostatically polarized at 1.10 V (above transpassive dissolution potential) for 2 minutes in 3.5 wt.% NaCl solution at 70 °C at the same extension rate of 5×10^{-4} mm/s.

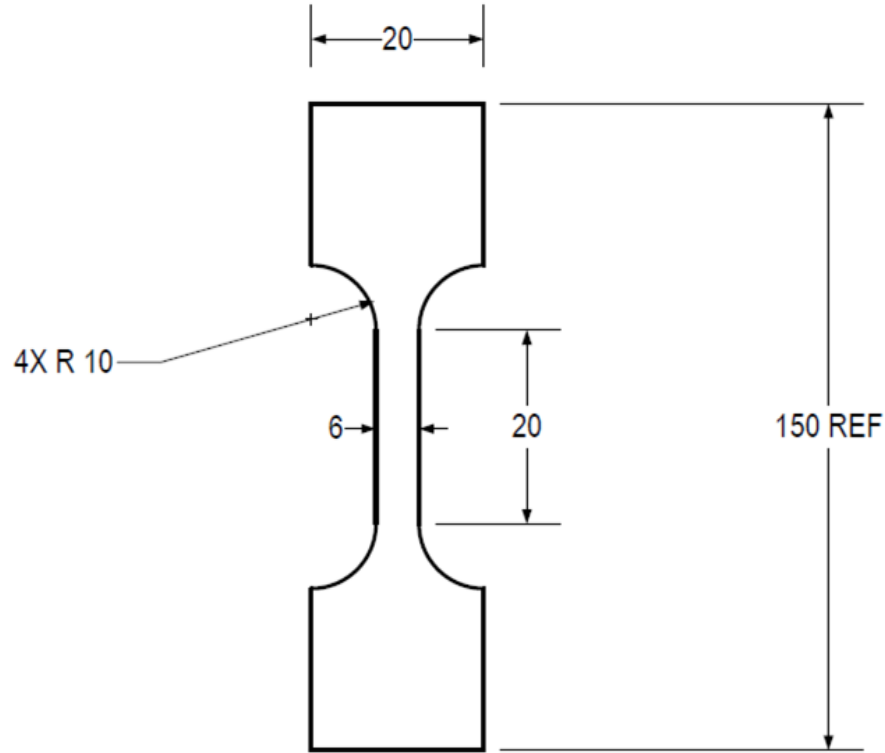


Figure 8.3: Flat tensile specimens for polarized SSRT (measurements in mm).

An interrupted drop-potential test was performed on 304L by polarizing the sample to 0.35 V for 2 minutes then dropping to 0.10 V for the remainder of the test, but rather than straining to failure, the experiment was halted at 2 mm, approximately 1/3 of the nominal strain to failure. The interrupted test environment was aerated 3.5 wt.% NaCl solution at 24 °C at an extension rate of 1×10^{-4} mm/s (strain rate of 5×10^{-6} s⁻¹). The surfaces were analyzed via SEM for evidence of SCC.

To determine whether SCC occurs at high chloride concentrations on 304L, a drop-potential test was performed in an aerated 25 wt.% NaCl solution at 24 °C at an extension rate of 1×10^{-4} mm/s. The sample was polarized at 0.14 V for 2 minutes, then dropped

to -0.05 V until failure. A lower strain rate was chosen to promote more SCC, based on the premise demonstrated in Figure 8.4 [131].

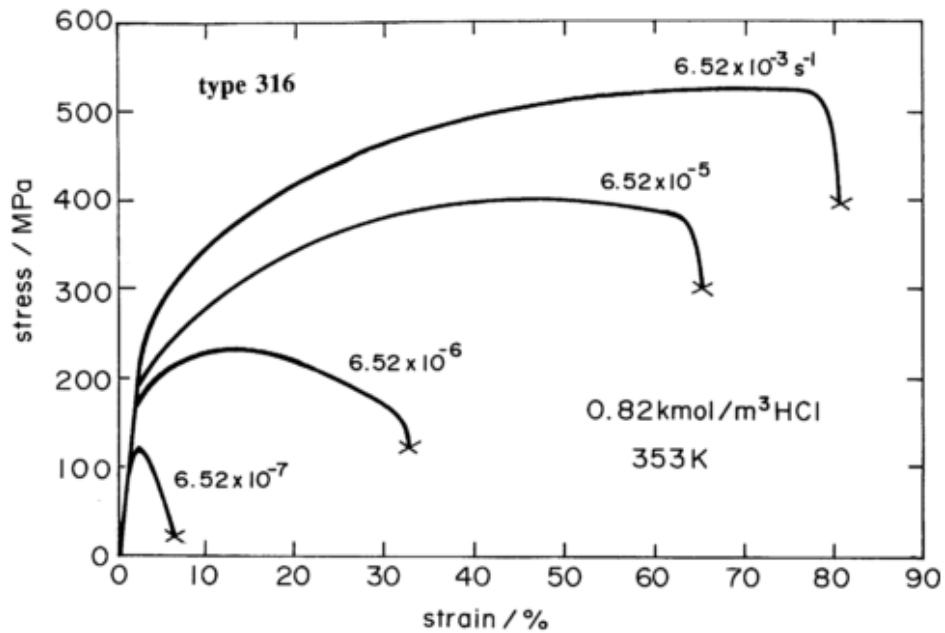


Figure 8.4: Effect of strain rate on environmental effects in 316 in 0.82 kmol/m^3 HCl solution at 353 K [131]

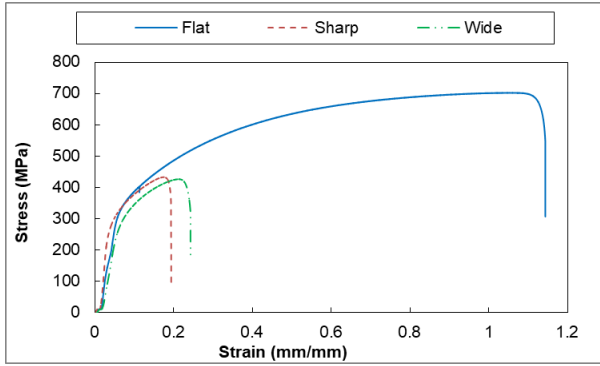
The effect of pH was tested on 316L by comparing samples strained to failure at an extension rate of $1 \times 10^{-4} \text{ mm/s}$. One sample was submerged in a nitrogen-deaerated 0.1 M HCl (pH 1), 2.9 wt.% NaCl solution $24 \text{ }^\circ\text{C}$. The chloride content of the solution was the same as 3.5 wt.% NaCl solutions and $24 \text{ }^\circ\text{C}$ was chosen for safety reasons. Two samples were immersed in aerated 3.5 wt.% NaCl solution at $70 \text{ }^\circ\text{C}$ to compare to the low pH conditions. The stress-strain results were normalized by comparing with samples strained in air and in $70 \text{ }^\circ\text{C}$ deionized water. Each other alloy was also tested in pH 1 solution under the same conditions and compared to dry tests.

8.2 Results and Discussion

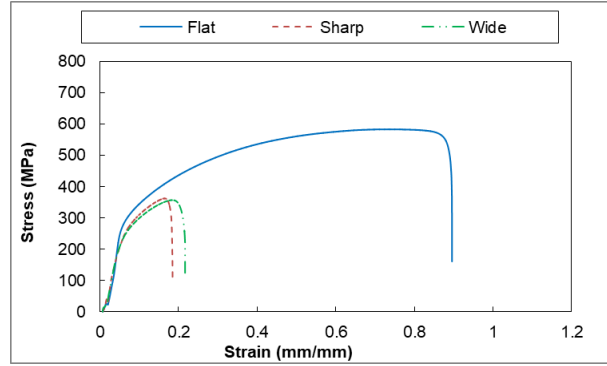
8.2.1 Effect of Geometry

Tensile testing, in both wet and dry conditions, was repeatable. The load frame measurements and environmental setup allowed for reliable results from which conclusions can be

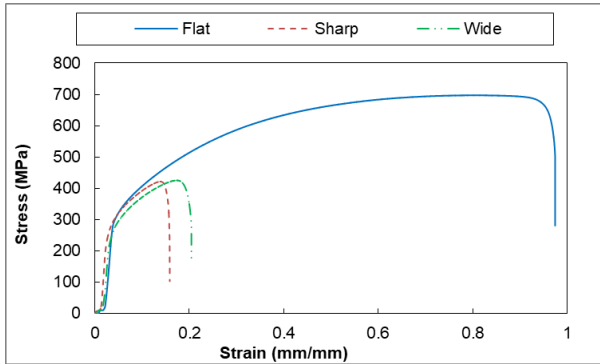
deduced, even with a low number of tests. An extensometer was used for the dry tests, but only crosshead data are reported so that all data can be compared. The temperature and flow rate were very consistent until a pump failure during AL-6XN tests resulted in inconsistent flow rates and higher temperature variability. As a result, only one AL-6XN wide notch specimen was tested. Engineering stress-strain results are shown in Figure 8.5, however it should be noted that the strain measurements for the notched samples are only approximate due to the sample geometry.



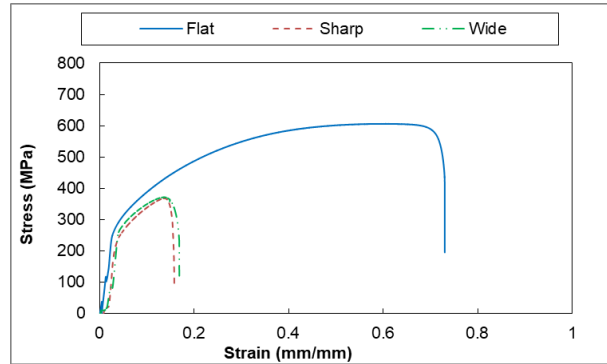
(a) 304L in air at 24 °C



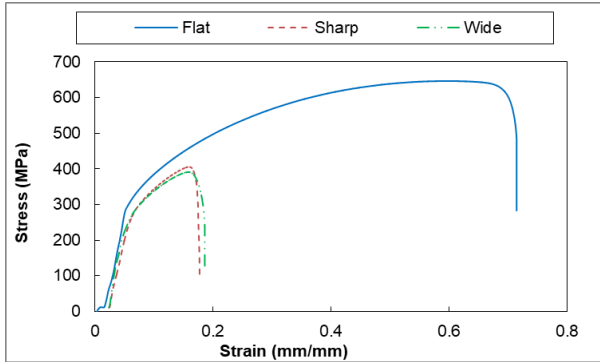
(b) 304L in NaCl solution at 70 °C



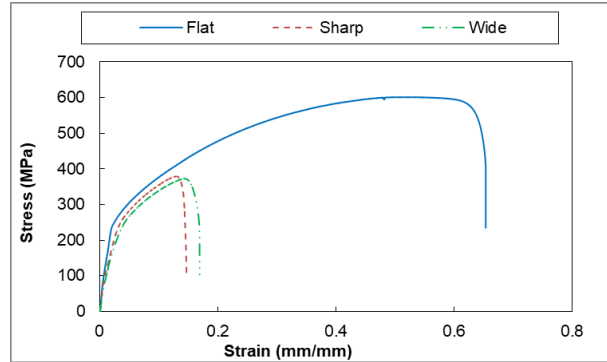
(c) 316L in air at 24 °C



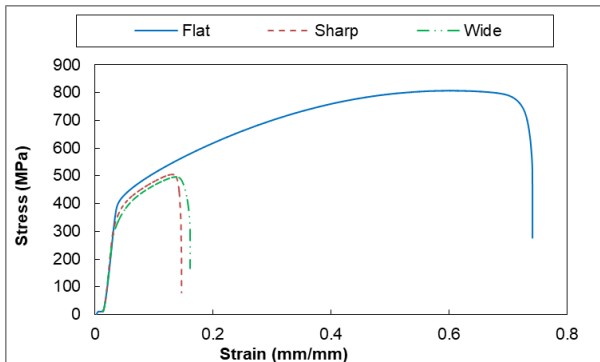
(d) 316L in NaCl solution at 70 °C



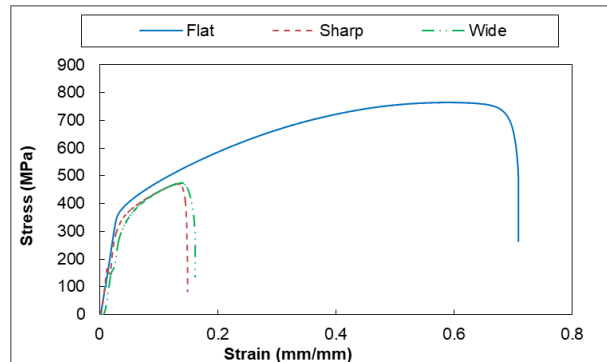
(e) 904L in air at 24 °C



(f) 904L in NaCl solution at 70 °C



(g) AL-6XN in air at 24 °C



(h) AL-6XN in NaCl solution at 70 °C

Figure 8.5: The effect of geometry on mechanical properties.

The notched samples failed at lower stresses and strains than the flat samples in both water and air tests. Notched samples of each alloy failed at stresses about 60 % of that of the flat specimen. The strain was decreased to about 20 % of the flat in each alloy.

In air, ductility is dependent on specimen stress state, which can be quantified by equivalent stress and triaxiality [132]. Specimen geometries with higher triaxialities exhibit lower ductility [132]. The effect of the machined notches was as expected: the large stress and strain drops between the flat and notched samples were due to the decreased cross-sectional area. The amounts by which the notch decreased the final strain are shown in Figures 8.6 and 8.7. The difference between the sharp and wide notched samples is attributed to the dissimilar triaxialities, which is known to affect specimen ductility. Each alloy was affected similarly by the geometrical changes, as anticipated.

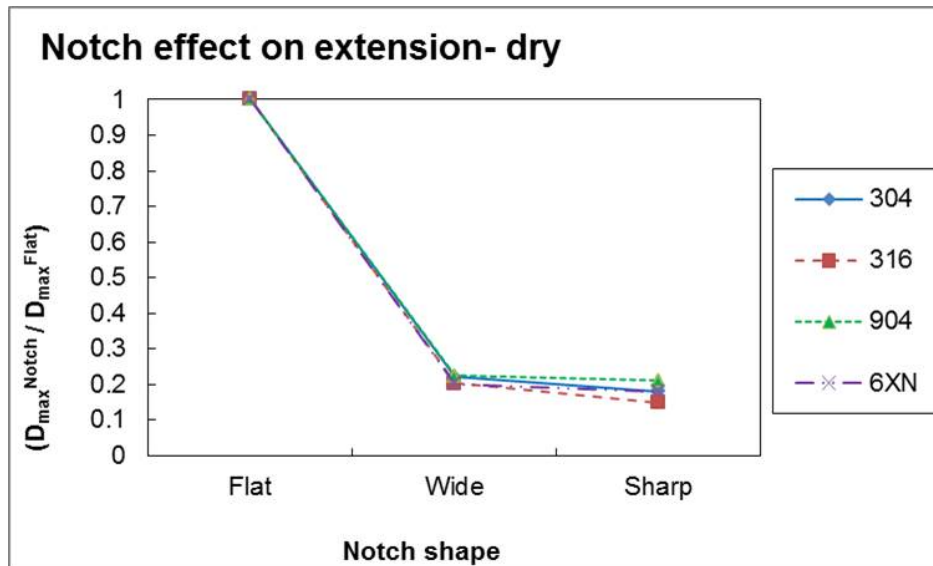


Figure 8.6: Effect of stress state on strain at failure in air at 24 °C

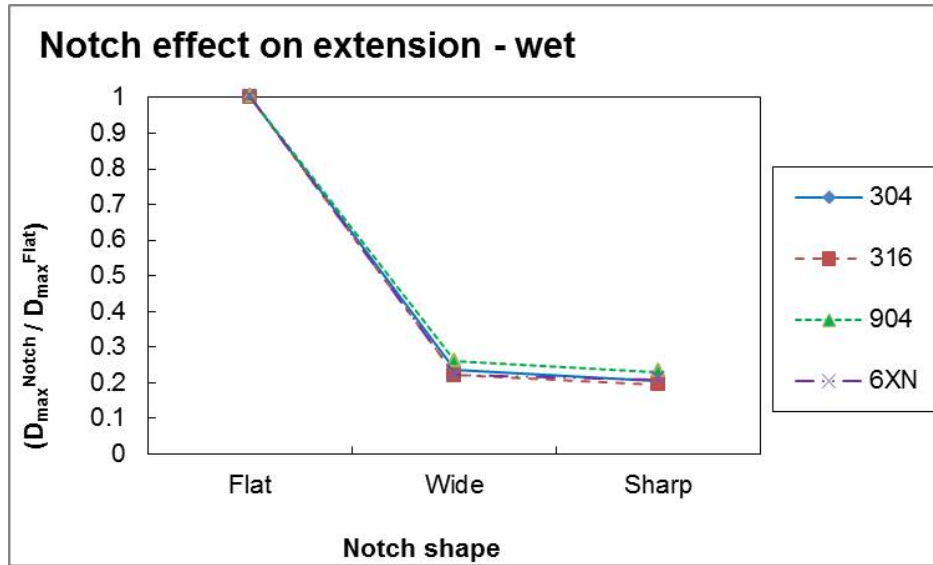
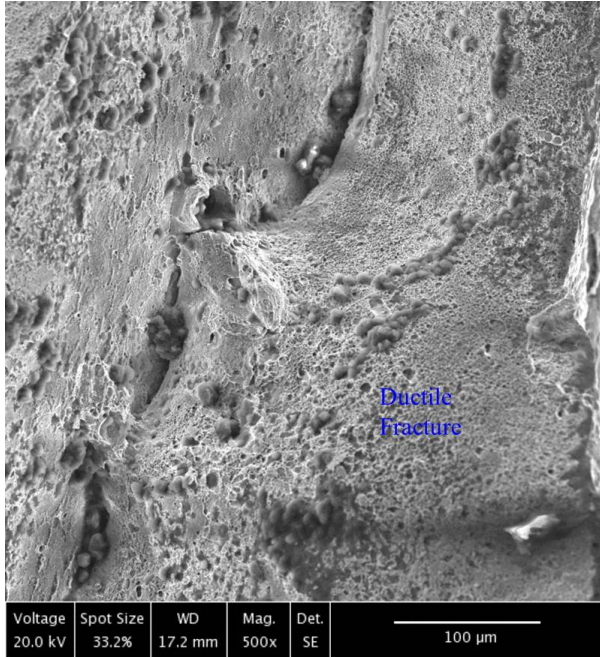
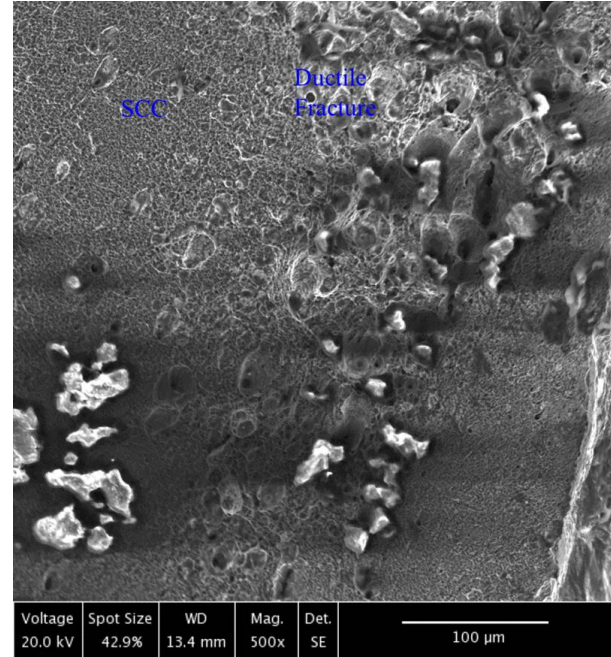


Figure 8.7: Effect of stress state on strain at failure in NaCl solution at 70 °C

Stress-strain data in Figure 8.5 show that alloys 304L and 316L were susceptible to SCC, while 904L and AL-6XN displayed little SCC. The electron micrographs in Figures 8.8 and 8.9 show the effect of SCC on the fracture surface. The aqueous 304L sample shows signs of transgranular SCC while the surface of the aqueous AL-6XN resembles that of the dry AL-6XN sample.



(a) Dry air at 24 °C

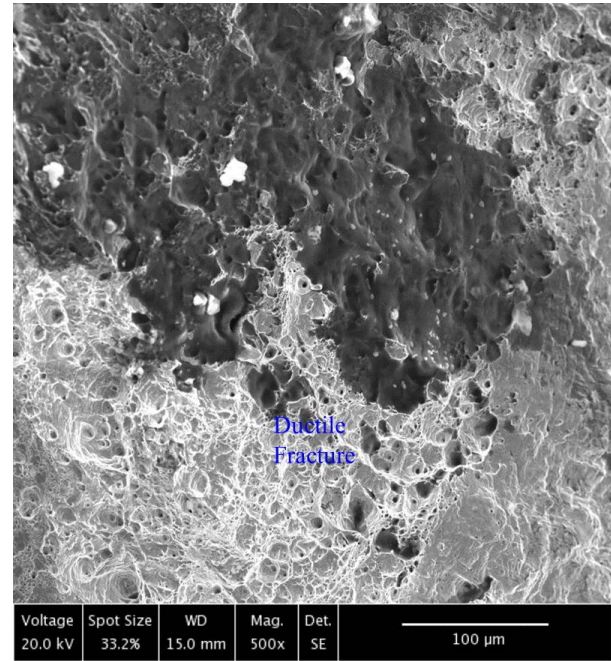


(b) NaCl solution at 70 °C

Figure 8.8: Fracture surface of 304 flat samples



(a) Dry air at 24 °C



(b) NaCl solution at 70 °C

Figure 8.9: Fracture surface of 6XN flat samples

In each alloy, there was little effect of geometry on SCC, as shown in Figure 8.10. Some effects of geometry on strain at failure were observed in Figure 8.11. These tests cannot be interpreted simply in the context of stress state effects. The original objective of this work was to create conditions that would lead to varying extents of SCC. However, there were major differences in test time and strain rate for each geometry, which complicates interpretation of the results. Each specimen was pulled at a constant extension rate, meaning the notched samples were exposed to higher local strain rates, which could affect the amount of mechanical and corrosive failure. The time-in-test was different for the geometries as well, flat specimen tests lasted approximately 10-15 hours while the notched specimen tests lasted only approximately 2-4 hours.

Different SCC test methods show opposing results based on the amount of time the specimen spends in the corrosive solution [71]. Because SCC is a combination of mechanical failure and corrosion, cracking can be increased either with stress or time [59]. For these tests to be effective measures of SCC, strain rates must be slow enough to permit environmental effects [133]. Therefore the larger environmental effects observed for the flat specimens were concluded to be a consequence of the low strain rate and long time immersed in the solution (approx. 15 hours). The local strain rates in the notched specimens were higher and their durations much shorter (approx. 4 hours).

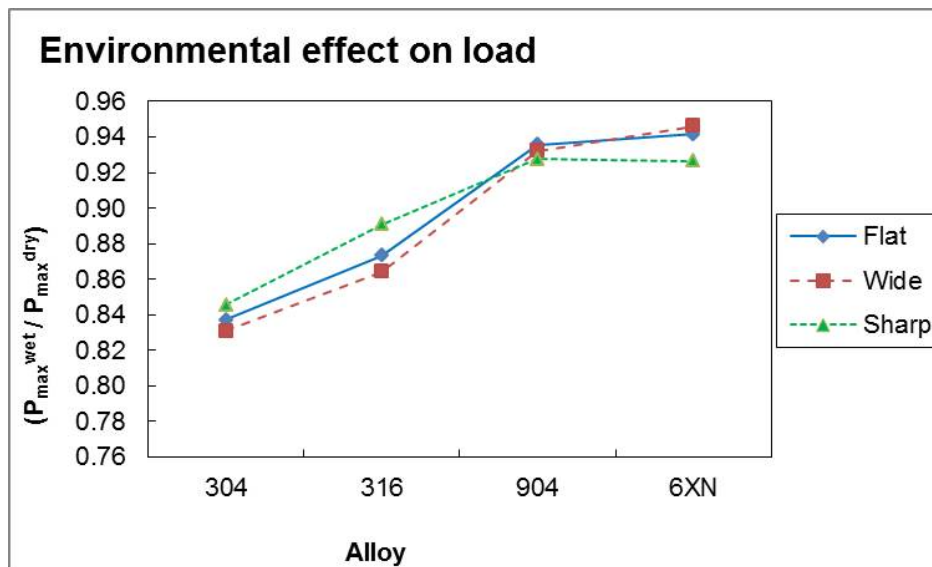


Figure 8.10: Environmental effect of notch on stress

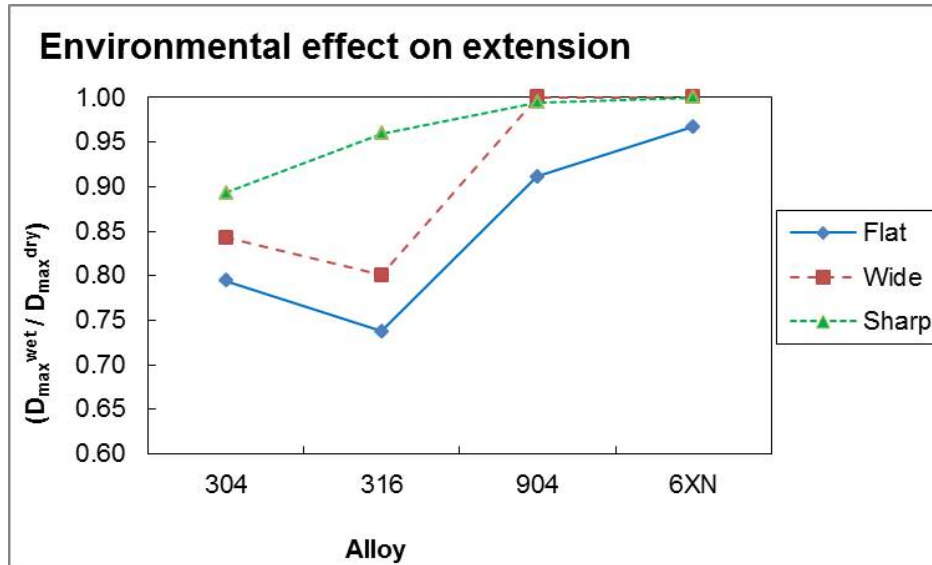


Figure 8.11: Environmental effect of notch on strain

The influence of environment on stress and strain was affected by alloy chemistry. The super-austenitic grades (904L and AL-6XN) showed a low environmental effect, while 304L and 316L showed a large drop in both maximum stress and strain to failure. Decreased ultimate stress demonstrates a decrease in cross sectional area at the onset of non-uniform deformation. Decreased strain at failure is due to either cracking or decreased cross sectional area. (Though difficult to visualize in these non-polarized tests, this separation of maximum stress and strain to failure effects can be seen in Figure 8.18.)

The decrease in both mechanical properties in 304L is probably due to both pit formation (decrease in cross sectional area) and SCC. Strain results suggest that 316L underwent more SCC than 304L, while environmental effect on maximum stress suggest that there was less pitting on 316L than 304L. Strain data for the 316L sharp notched sample contained some experimental error that was not found in the other alloys, which could contribute to part of the divergence from the trend. Despite these complications, the tests did show the feasibility of the SSRT setup and the ability to load specimens in a chloride environment over a range of temperatures.

8.2.2 Effect of Polarization and Environment

All stress-strain results are shown in Figures 8.12-8.16. The specimen deformed while polarized to its pitting potential showed the lowest load-carrying capacity of all specimens. The extensive pitting led to a continuous decrease in specimen cross-section which was consistent with the continuously varying load carrying capacity of the specimen. This was also shown in the 25 wt.% NaCl drop-potential test, Figure 8.12. After failure, the sample showed signs of significant pitting, including some pits that grew through the entire thickness of the sample. The drop-potential test on 304L still exhibited an environmental effect, though not as severe. The acidic test also shows a decreased mechanical properties, similar to the drop-potential test, however the strain at failure is much larger. Another aspect of the effect of environment is the shape of the stress-strain curve. The low pH and low chloride content drop-potential tests exhibit similar behavior; both curves show work hardening, but very little necking, as characterized by the sudden drop in stress at failure. The potentiostatic and high chloride drop-potential tests, which resulted in significant pitting, exhibit a large decrease of cross-sectional area before failure, shown by the extended decrease in stress before failure. To clarify the effect of polarization, results for 304L potentiostatic and drop-potential SSRT in 3.5 wt.% NaCl are shown in Figure 8.18 and the current measured in the interrupted drop-potential test is shown in Figure 8.19. The current increased to a high level during the initial polarization above the pitting potential, then decreased significantly when the polarization dropped. At the lower polarization, the current increased over time as corrosion continued, then reached a steady state where the current remained consistent for the duration of the test.

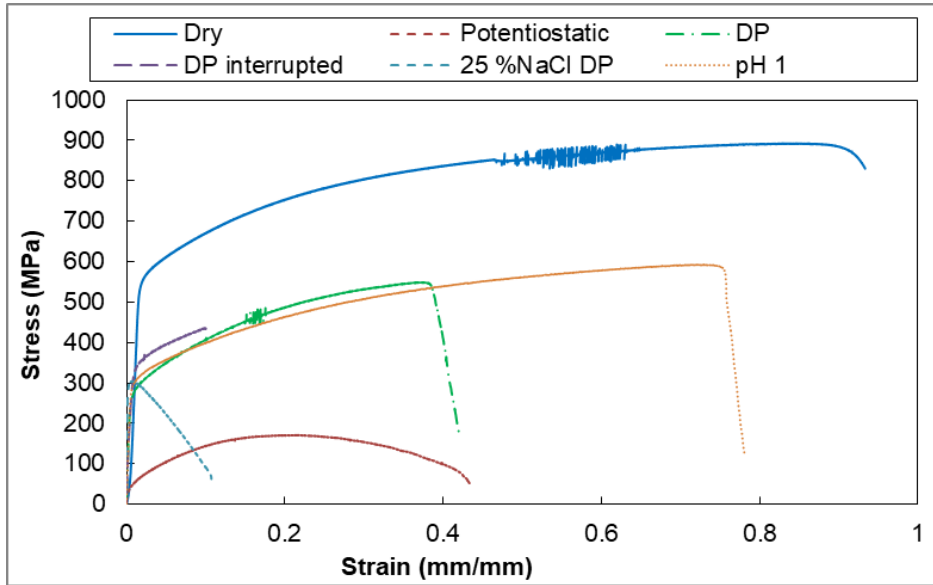


Figure 8.12: Stress-strain curves of 304L under different environmental and polarization conditions.

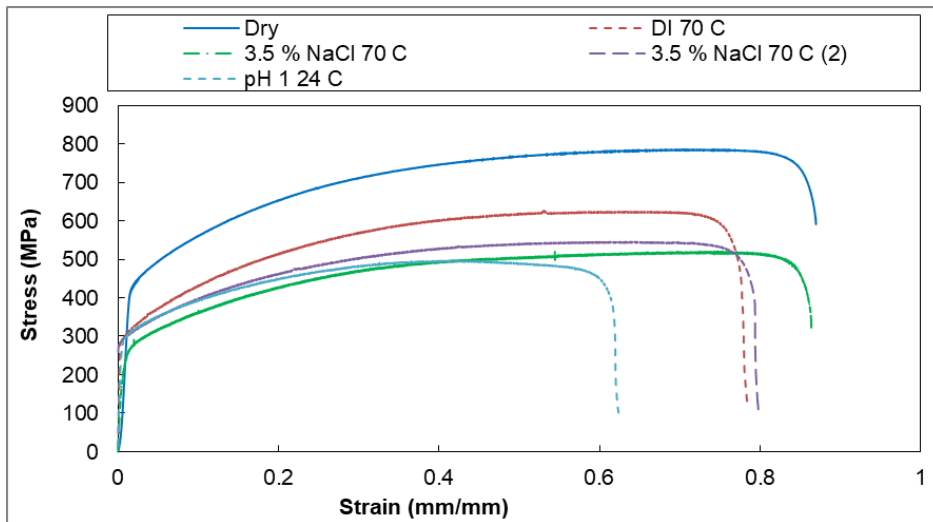


Figure 8.13: Stress-strain curves of 316L under different environmental and polarization conditions.

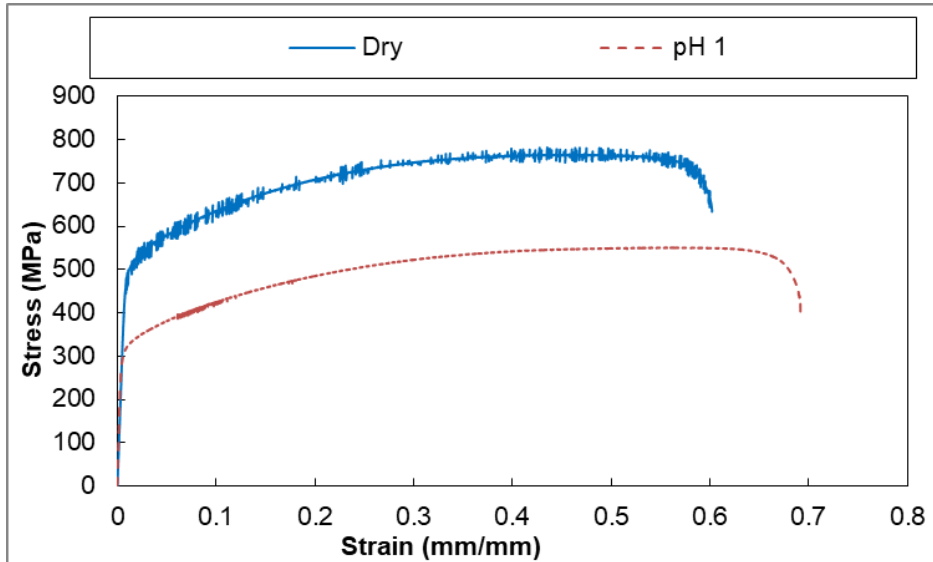


Figure 8.14: Stress-strain curves of 310S in acidic and dry conditions.

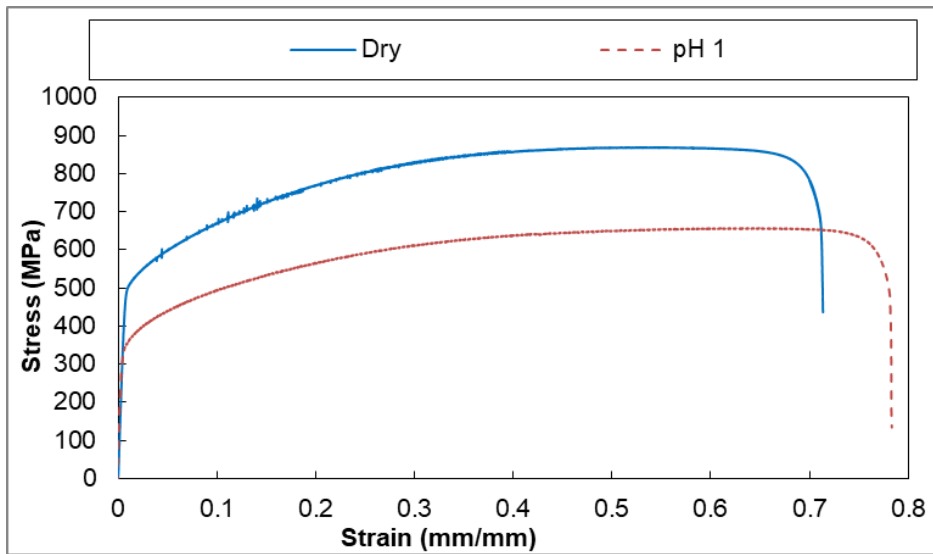


Figure 8.15: Stress-strain curves of 317L in acidic and dry conditions.

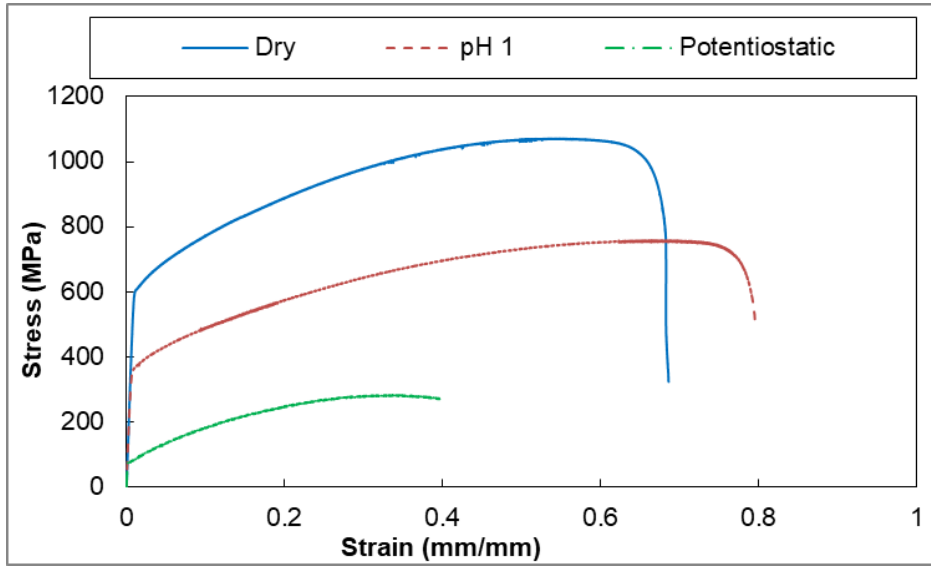


Figure 8.16: Stress-strain curves of AL-6XN under different environmental and polarization conditions.

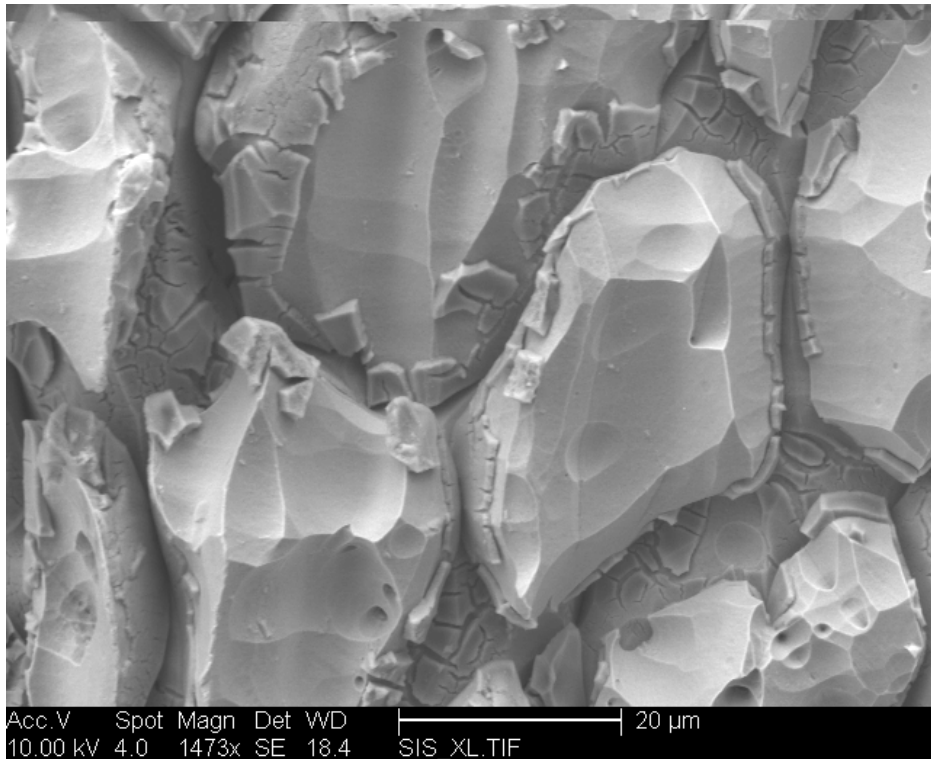


Figure 8.17: Etched surface of AL-6XN after polarized SSRT.

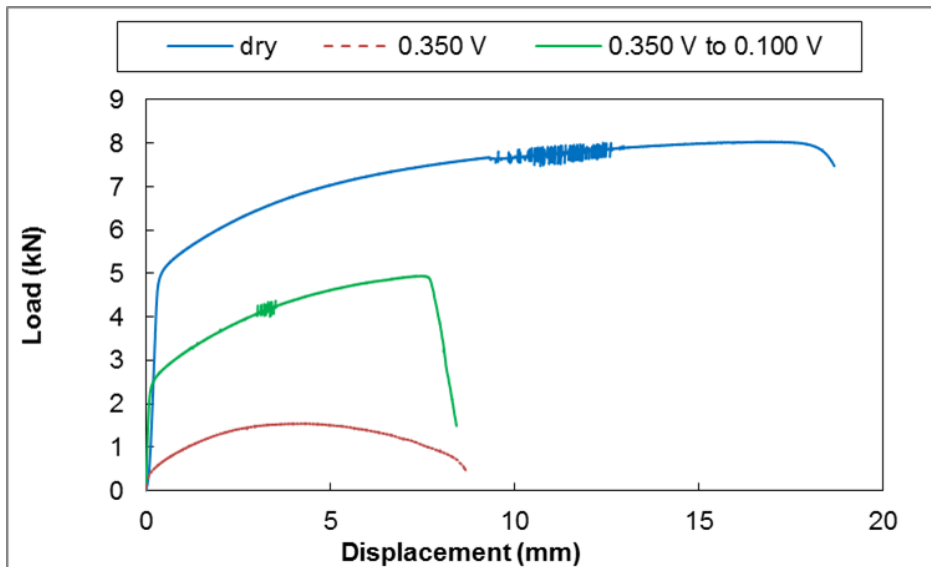


Figure 8.18: Stress-strain curves of polarized 304L at 24 °C in non-aerated 3.5 wt.% NaCl solution.

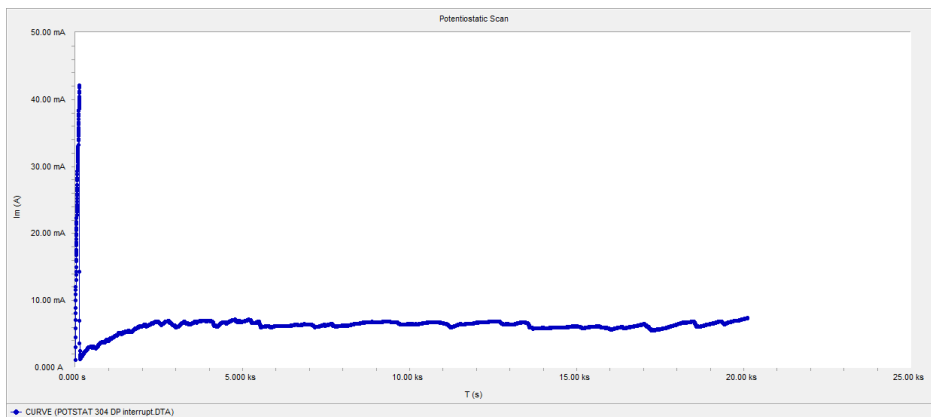


Figure 8.19: Current in interrupted drop-potential test. The current increases as pitting occurs, then drops as the potential drops below the pitting potential, then increases to a steady level as corrosion continues.

The stress-strain curve of potentiostatically polarized AL-6XN is shown in Figure 8.16. The surface of the sample became rough, shown in Figure 8.17, but there were no signs of pitting or SCC. The decreased mechanical properties are probably due to decreased cross sectional area resultant from transpassive dissolution.

The interrupted test did not show any clear signs of SCC. There were many pits on the surface ranging greatly in size, shown in Figure 8.20, but neither the pit mouths nor bases showed any visible cracking. It is not known whether SCC were simply not visible, closed during unloading, or had not formed yet.

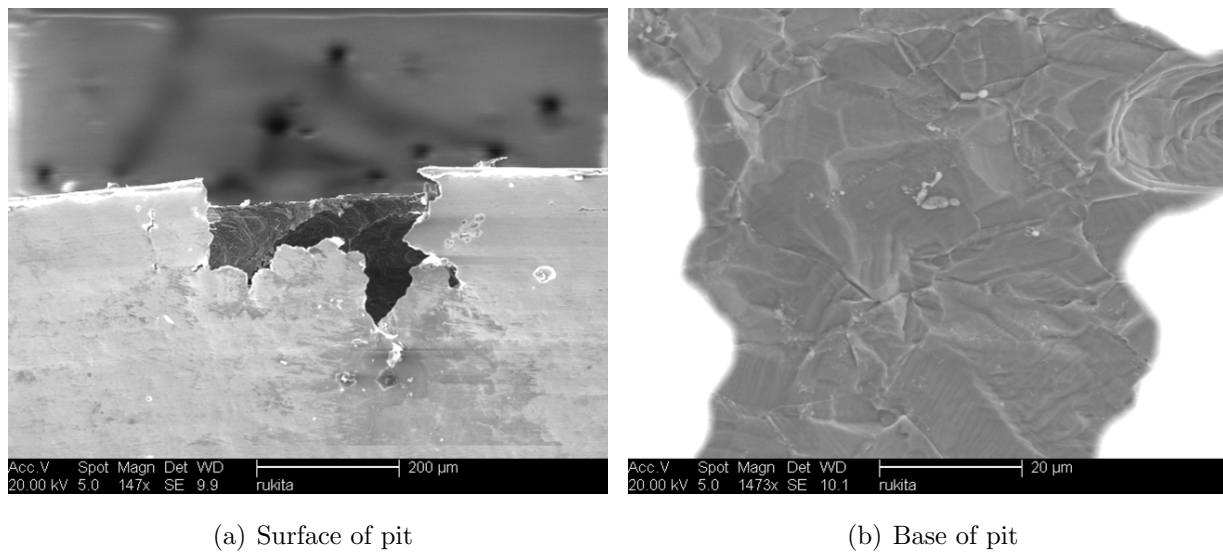


Figure 8.20: Pit on 304 surface after drop-potential test in aerated 3.5 wt.% NaCl at 24 °C

Figure 8.13 shows that the dry test and DI water test did not correlate closely. This demonstrates that the dry tests cannot necessarily be used to evaluate the extent of SCC because of the difference in setup and sample loading procedure. Using the DI test as a baseline, 3.5 wt.% NaCl at 70 °C did not appear to cause significant SCC, though the stresses are somewhat lower in the salt water. Based on mechanical properties, the acidic solution caused either SCC or a significant decrease of cross-sectional area before failure. The fracture surface of the DI and acidic tests are shown in Figure 8.21. The DI surface was comprised entirely of traditional ductile cup-cone structures, as expected. While there was significant ductile failure mode apparent on the acid test fracture surface, there was also evidence of transgranular SCC. A cross section near the fracture surface, Figure 8.22, shows cracking all along the surface of the sample to a depth of about 50 μm along the wide

edge and 100 μm along the narrow edge of the specimen. The deeper corrosion along the narrow edge is due to the increased inclusion surface area along the plane of rolling. This is supported by the corrosion geometry along the wide sample edge, which contains cracks perpendicular to the sample edge and possible crevice corrosion parallel to the edge.

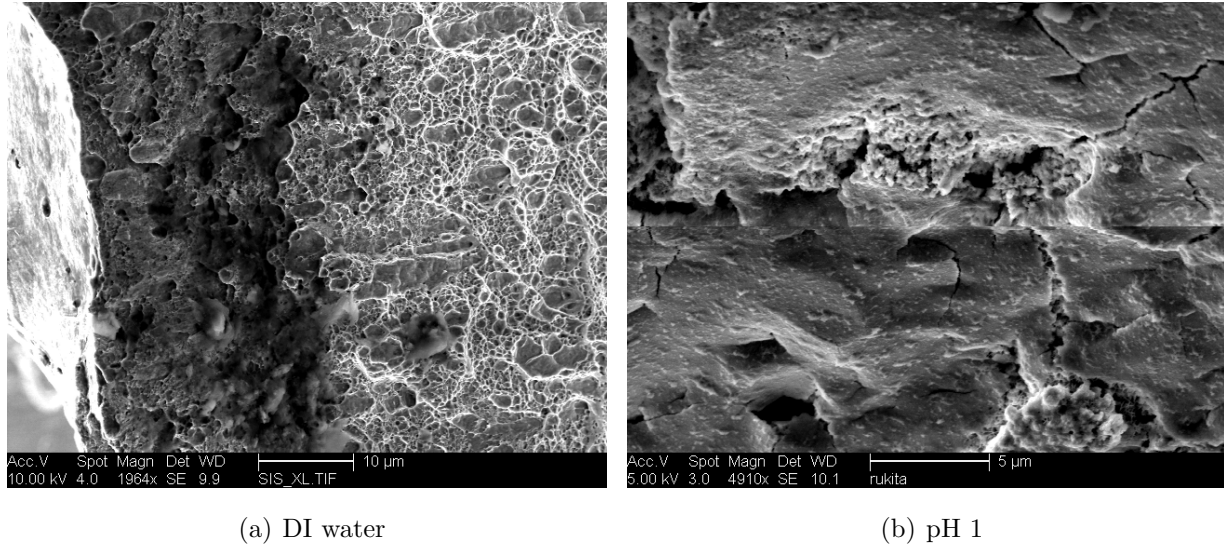
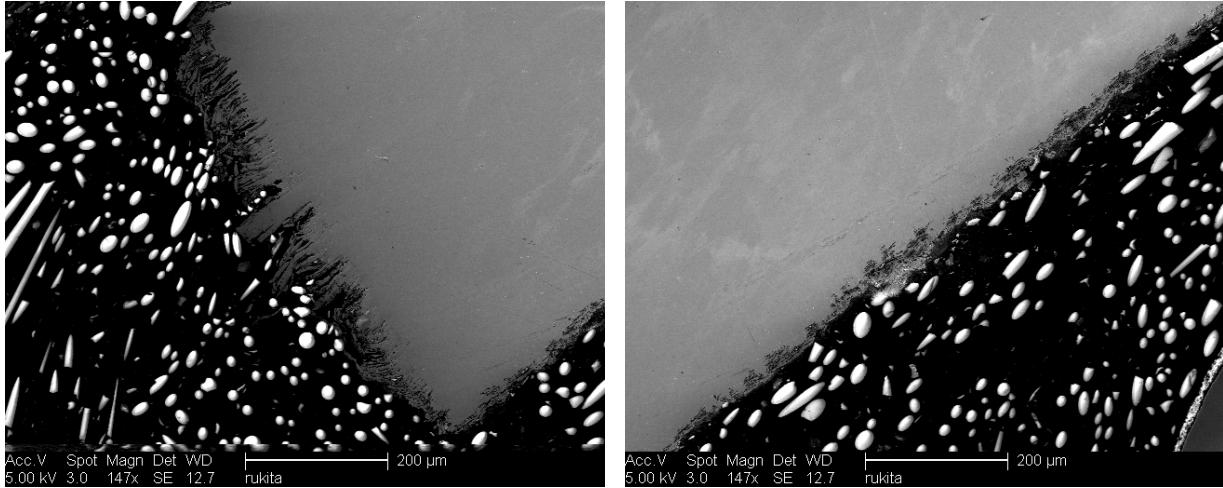
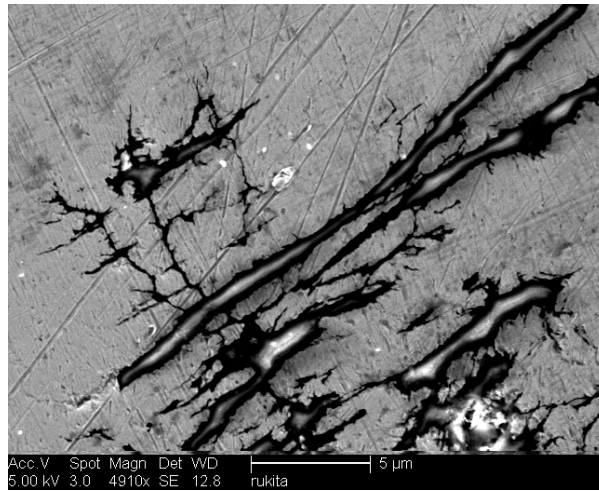


Figure 8.21: Fracture surfaces of 316L tested in DI water (ductile) and acidic solution (SCC).



(a) Narrow edge

(b) Wide edge



(c) Wide edge

Figure 8.22: Cross section near fractures surface of 316L pH 1 acidic solution (SCC).

The interplay between pit growth, SCC, and ductile failure is related to the relative growth of pits and SCC. In SSRT, the rate of plastic deformation leading to ductile failure is controlled by elongation rate, so the remaining variables are environment and polarization, which determine pitting and SCC rates. Neither pit growth rates nor SCC growth rates were directly measured, so it is difficult to quantitatively determine the varying effects of the environments and polarizations tested. Tsujikawa measured crack growth rates ranging approximately 1-10 $\mu\text{/h}$, depending on polarization and conditions [74]. SCC was observed to extend around 100 μ from the sample edges, which suggests a similar crack growth rate.

Using monotonic loading, it was possible to control the primary failure mode, favoring pitting, SCC, or ductile failure. While much is still unknown, it is clear that SSRT can produce similar trends observed using other SCC testing methods.

8.3 Discussion

Stress corrosion cracking is dependent on numerous system properties, such as alloy chemistry and material condition, environment chemistry and temperature, strain rate, external polarization, etc [29, 74, 102, 113, 131, 134]. Many studies have concentrated on determining the role of these variables in SCC of austenitic stainless steels. The goal of this work was to develop a method using drop-potential polarization to elucidate the pit-crack transition in commercially available materials.

The method used was developed to enable comparison of multiple commercially available materials. Though there are conditions that have been shown to cause SCC in some of the alloys tested, the conditions, such as environment and strain rate, were chosen to promote SCC in multiple systems rather than tailored to a specific alloy [131, 134]. One example of non-ideal conditions is strain rate, where although there are conditions under which both 304 and 316 will undergo SCC, these conditions are not ideal to test both alloys, shown in Figure 8.23 [131].

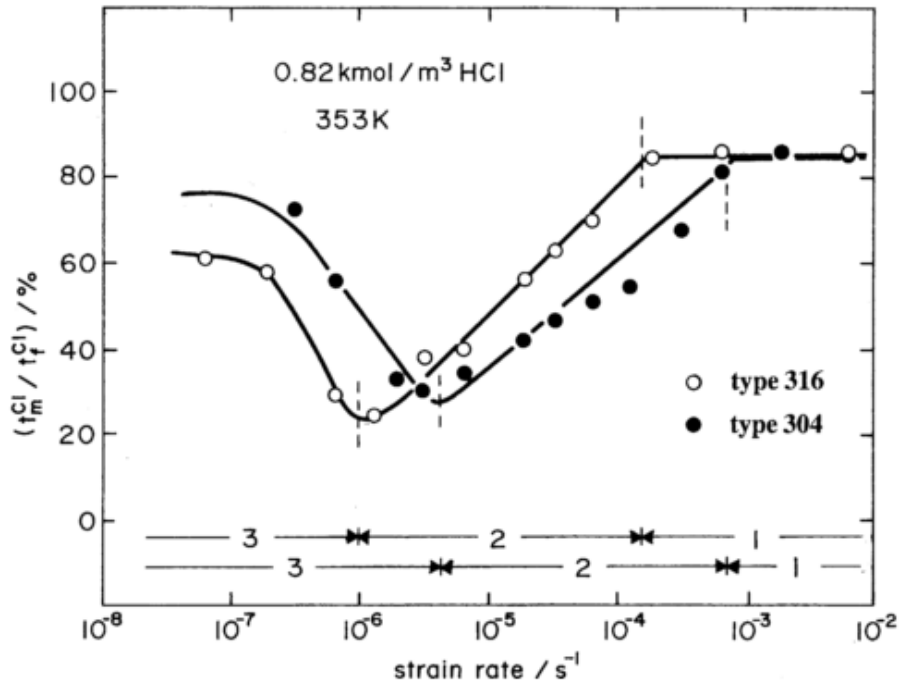


Figure 8.23: Effect of strain rate on SCC in 304 and 316 stainless steels in acid [131].

As with environmental test conditions, sample geometry was governed by constraints due to material comparison rather than being able to employ ideal conditions. Flat stock was used throughout SCC testing because it was the only stock material available for some of the materials tested, so it was used for all alloys to maintain consistency. Though SCC occurs on flat material, it is not ideal for uniaxial SSRT for multiple reasons. The rectangular cross-section of the sample deforms into a more complex geometry during non-uniform deformation, making it more difficult to track damage growth direction than in a system with the same cross-section shape before and after deformation. Furthermore, the initial flat-rolled material is anisotropic due to the rolling process. Corrosion processes occur at different rates in the rolling plane and perpendicular to the rolling plane due to the shape of the inclusion particles within the steel. This can be seen in the corroded sample cross section, where corrosion was deeper on the narrow edge than the wide edge. The corrosion on the wide edge of the sample also showed cracks perpendicular to the edge with crevice corrosion parallel to the edge due to inclusions in the metal. Round samples would simplify fracture and cross-section analysis due to the simple radial symmetry of the fracture surface and cross-section. Samples machined from round material would minimize the different cor-

rosion processes occurring around the perimeter of the sample due to the radial symmetry. While the SCC evaluation was not under ideal conditions, a viable method was developed to mechanically deform flat samples in a controlled environment with an applied potential. This method can be used in cases where round cross-section samples are not available or ideal. This method can also be expanded to other non-round specimen geometries where forming a water-tight seal around the sample is non-trivial.

Chapter 9

Conclusion

While both chromium and molybdenum each increase pitting resistance, the mechanism by which they do so is different. Based on polarization curves at varying temperatures, chromium has a larger impact on the temperature at which the passive film breaks down while molybdenum has a greater impact on pitting potential in an environment where stable pitting can occur. Molybdenum also decreases metastable pitting, while chromium does not have a pronounced effect on the occurrence of metastable pitting.

The corrosion properties of iron thin films of varying thickness, both with and without conductive backings, demonstrated that conductivity influences thin film corrosion. Thicker films corrode faster than thinner films while maintaining the same corrosion mechanism based on corrosion morphology. Conductive backings on iron thin films increase corrosion rate while also changing the mechanism of corrosion, shown by the corrosion morphology. While the mechanisms are not fully understood, iron thin films sputtered onto insulating substrates appear to undergo localized corrosion while iron thin films on conductive substrates appear to undergo general corrosion similar to that of bulk iron.

It was possible to control the failure mechanism of 300 series stainless steels (304L and 316L) using monotonic loading in chloride solutions. Using different environmental and polarization conditions, the failure mechanism can be controlled, resulting in either stress corrosion cracks, ductile mechanical failure, or catastrophic reduction in area due to pitting. However, there was not enough evidence to definitively conclude that monotonic loading shows the same interplay between SCC and pitting as has been observed with cyclic loading.

Chapter 10

Future Work

10.1 Bulk Pitting

While models, such as PREN, have been validated under many conditions, it is clear that lacunae remain in their predictive power regarding their applicability. One such unpredicted variable is temperature, which has been shown here to cause divergence from the PREN model, specifically regarding the impact of chromium and molybdenum. To further study the interplay between temperature and alloy chemistry, investigational alloys with a gradient of composition should be developed to separate the influences of chromium and molybdenum on corrosion. The effect of alloy chemistry on the temperature at which pitting begins can be determined for chromium and molybdenum separately. Alloys that combine both chromium and molybdenum within the studied gradient can be used to determine if the alloying effects are synergistic, independent, or competing. Similar experimentation can also be employed to investigate the influence alloying under other environmental conditions. This can lead to further exploration of the mechanisms by which chromium and molybdenum increase corrosion resistance and to develop better models of alloy pitting resistance.

10.2 Thin Film Corrosion

It is clear that electrical conductivity influences the corrosion of nano-crystalline iron, though the cause of this effect is elusive. It is difficult to examine the impact of film resistivity directly without also changing other significant variables such as film thickness or alloy chemistry. Instead, it would be expedient to observe the effects of substrate conductivity on thin film

corrosion. Thin films of consistent thickness should be sputtered onto inert substrates (noble metals, doped semiconductors, *etc.*) with a range of electrical conductivities. A combination of potentiodynamic polarization, SVET, and optical or electron microscopy can be used to probe the effect of substrate conductivity on corrosion rate and mechanism. The results will help direct the efforts to develop protective coatings, corrosion sensors, and other metallic thin film systems.

Initial testing of stainless steel films was initiated, showing that the resistivity of 200 nm 304L and 316L stainless steel films are similar to their bulk alloy resistivity. Polarization curves must be measured before other testing can be initiated. SVET measurements can be made by polarizing the thin films above their pitting potential, thus allowing SVET scans to measure the localized corrosion response.

To study the effect of alloy chemistry further, model stainless steel alloys can be sputtered onto silica substrates. Rather than analyzing multiple distinct alloy compositions, thin films can be fabricated with continuous ranges of alloy composition. The base alloy for each test should be 304 stainless steel because it is a cost effective method to ensure a consistent base alloy. A range of chromium or molybdenum can be sputtered with the base 304 to create a range of chromium (18-25 wt.%) or molybdenum (0-7wt.%) while keeping all other constituents constant. In order to ensure complete mixing, this technique sputters the metals in alternating layers, creating a homogeneous alloy in the thickness direction. Based on 304 and 316 preliminary results, these gradient thin films can be polarized under conditions that will ensure that some alloy composition ranges will corrode, while other alloy compositions will remain passive. The results can be compared with those of bulk stainless steel alloys to further study the effects of chromium and molybdenum on corrosion resistance of stainless steels.

10.3 Stress Corrosion Cracking

Various failure modes can be produced using monotonic loading by adjusting the environment and electrical polarization. However, the failure mechanism cannot yet be fully predicted, so a better model must be developed. Polarization is a powerful technique that can be utilized to effect the desired failure mechanism, so further study on the effects of polarization on pitting and SCC should be implemented. This examination should concentrate primarily on drop-potential testing, specifically the impact of varying hold times above the pitting potential

as well as the effects of dropping to different potential regions (near pitting potential, above repassivation potential, below repassivation potential, etc.). By strengthening SSRT as a tool to control localized corrosion and mechanical failure, the mechanism by which alloys undergo SCC can be further illuminated.

References

- [1] A. Stierle: *Science* 2008, vol. 321 (321), pp. 349–350.
- [2] J. Waldman: *Rust: the longest war*: Simon Schuster, New York, NY, 2015.
- [3] E. McCafferty: *Introduction to Corrosion Science*: 2010.
- [4] R. Zaera, J. Rodríguez-Martínez, a. Casado, J. Fernández-Sáez, a. Rusinek, R. Pesci: *International Journal of Plasticity* 2012, vol. 29, pp. 77–101.
- [5] V. M. Blinov: *Russian Metallurgy (Metally)* 2010, vol. 2009 (6), pp. 478–487.
- [6] C.-O. Olsson, D. Landolt: *Electrochimica Acta* 2003, vol. 48 (9), pp. 1093–1104.
- [7] M. Yajima, M. Ariei: *Materials Performance* 1980, vol. 19 (12), pp. 17–19.
- [8] W. Pollock, J. Barnhart (Eds.): *Corrosion of Metals Under Thermal Isulation*: ASTM International, Ann Arbor, MI, 1984.
- [9] G. Lü, C. Xu, Y. Lü, H. Cheng, Z. He: *Chinese Journal of Chemical Engineering* 2008, vol. 16 (4), pp. 646–649.
- [10] T. S. Mintz, X. He, L. Miller, R. Pabalan, Y.-M. Pan, L. Caseres, G. Oberson, D. Dunn: *Coastal Salt Effects on the Stress Corrosion Cracking of Type 304 Stainless Steel*: in: *NACE Corrosion*: 2013.
- [11] M. Anoop, K. Balaji Rao, N. Lakshmanan: *International Journal of Pressure Vessels and Piping* 2008, vol. 85 (4), pp. 238–247.
- [12] K. M. Zhang, J. X. Zou, T. Grosdidier: *Journal of Nanomaterials* 2013, .
- [13] S. Jung, S. Li, Y.-G. Kim: *Electrochemistry Communications* 2006, vol. 8, pp. 658–664.
- [14] S. Fujimoto, H. Hayashida, T. Shibata: *Materials Science and Engineering A* 1999, vol. 267 (2), pp. 314–318.
- [15] Duplex stainless steels - a simplified guide: <http://www.bssa.org.uk/topics.php?article=668>.
- [16] R. S. Schepis, L. J. Matienzo, F. Emmi, W. Unertlb, K. Schriider: *Thin Solid Films* 1994, vol. 251, pp. 99–102.

- [17] S. Li, Y.-G. Kim, S. Jung, H.-S. Song, S.-M. Lee: *Sensors and Actuators B* 2007, vol. 120, pp. 368–377.
- [18] M. Kurosaki, M. Seo: *Corrosion Science* 2003, vol. 45 (11), pp. 2597–2607.
- [19] C. Pan, L. Liu, Y. Li, B. Zhang, F. H. Wang: *Journal of the Electrochemical Society* 2012, vol. 159 (11), pp. C453–C460.
- [20] G and C Merriam Co., 1966.
- [21] K. Sugimoto, Y. Sawada 1977, vol. 17 (November 1975), pp. 425–445.
- [22] H. Uchida, M. Yamashita, S. Inoue, K. Koterazawa: *Materials Science and Engineering A* 2001, vol. 319-321, pp. 496–500.
- [23] K. Miyake, K. Ohashi, H. Takahashi, T. Minemura: *Surface and Coatings Technology* 1994, vol. 65, pp. 208–213.
- [24] C. Pan, L. Liu, Y. Li, F. Wang: *Corrosion Science* 2013, vol. 73, pp. 32–43.
- [25] E. M. Pinto, A. S. Ramos, M. T. Vieira, C. M. A. Brett: *Corrosion Science* 2010, vol. 52 (12), pp. 3891–3895.
- [26] a. J. Sedriks: *International Materials Reviews* 1982, vol. 27 (1), pp. 321–353.
- [27] Y. Kim, M. Fregonese, H. Mazille, D. Féron, G. Santarini: *NDT & E International* 2003, vol. 36 (8), pp. 553–562.
- [28] S. Nagarajan, V. Raman, N. Rajendran: *Journal of Solid State Electrochemistry* 2009, vol. 14 (7), pp. 1197–1204.
- [29] D. Du, K. Chen, H. Lu, L. Zhang, X. Shi, X. Xu, P. L. Andresen: *Corrosion Science* 2016, .
- [30] M. A. Streicher: *Journal of The Electrochemical Society* 1955, vol. 103 (7), pp. 375–390.
- [31] L. F. Lin, C. Y. Chao, D. Macdonald: *Journal of Electrochemistry Society: Electrochemical Science and Technology* 1981, vol. 128 (6), pp. 1194–1198.
- [32] J. E. Truman: *Corrosion Science* 1977, vol. 17, pp. 737–746.
- [33] T. Li, L. Liu, B. Zhang, Y. Li, F. Wang: *Corrosion Science* 2016, vol. 104, pp. 71–83.
- [34] L. Liu, Y. Li, F. Wang: *Journal of Materials Science & Technology* 2010, vol. 26 (1), pp. 1–14.
- [35] L. Liu, Y. Li, F. Wang: *Electrochimica Acta* 2008, vol. 54 (2), pp. 768–780.
- [36] W. Ye, Y. Li, F. Wang: *Electrochimica Acta* 2006, vol. 51 (21), pp. 4426–4432.
- [37] N. Merakeb, A. Messai, A. I. Ayesh: *Thin Solid Films* 2016, vol. 606, pp. 120–126.
- [38] L. Liu, Y. Li, F. Wang: *Electrochimica Acta* 2010, vol. 55 (7), pp. 2430–2436.

- [39] T. Li, L. Liu, B. Zhang, Y. Li, X. Wang, F. Wang: *Electrochemistry Communications* 2015, vol. 52, pp. 80–84.
- [40] T. Li, L. Liu, B. Zhang, Y. Li, F. Wang: *Corrosion Science* 2016, vol. 111, pp. 186–198.
- [41] J. Soltis: *Corrosion Science* 2015, vol. 90, pp. 5–22.
- [42] D. Horner, B. Connolly, S. Zhou, L. Crocker, a. Turnbull: *Corrosion Science* 2011, vol. 53 (11), pp. 3466–3485.
- [43] 1979, , pp. 190–195.
- [44] N. Aouina, F. Balbaud-Celerier, F. Huet, S. Joiret, H. Perrot, F. Rouillard, V. Vivier: *Electrochimica Acta* 2011, vol. 56 (24), pp. 8589–8596.
- [45] P. J. Carvalho, L. M. C. Pereira, N. P. F. Gonçalves, A. J. Queimada, J. A. P. Coutinho: *Fluid Phase Equilibria* 2015, vol. 388, pp. 100–106.
- [46] Y. Huang, S. T. Tu, F. Z. Xuan: *Nuclear Engineering and Design* 2013, vol. 257, pp. 45–52.
- [47] R. C. Newman: *Corrosion* 2001, vol. 57 (12), pp. 1030–1041.
- [48] Z. Szklarska-Smialowska, E. Lunarska: *Werkstoffe und Korrosion* 1981, vol. 32, pp. 478–485.
- [49] Y. González-Garca, G. Burstein, S. González, R. Souto: *Electrochemistry Communications* 2004, vol. 6 (7), pp. 637–642.
- [50] M. P. Ryan, N. J. Laycock, R. C. Newman, H. S. Isaacs: *Journal of The Electrochemical Society* 1998, vol. 145 (5), pp. 1566.
- [51] J. W. Tester, H. S. Isaacs: *Journal of Electrochemistry Society: Electrochemical Science and Technology* 1975, vol. 122 (11), pp. 1438–1445.
- [52] A. Alamr, D. F. Bahr, M. Jacroux: *Corrosion Science* 2006, vol. 48 (4), pp. 925–936.
- [53] N. Mottu, M. Vayer, J. Dudognon, R. Erre: *Surface and Coatings Technology* 2005, vol. 200 (7), pp. 2131–2136.
- [54] D. Rodrigues-Marek, M. Pang, D. F. Bahr: *Metallurgical and Materials Transactions A* 2003, vol. 34 (June), pp. 1291–1296.
- [55] M. Ameer, a.M. Fekry, F. E.-T. Heakal: *Electrochimica Acta* 2004, vol. 50 (1), pp. 43–49.
- [56] C. Y. Chao, L. F. Lin, D. Macdonald: *Journal of The Electrochemical Society* 1981, vol. 128 (6), pp. 1187.
- [57] M. Tsujikawa, M. Egawa, N. Ueda, a. Okamoto, T. Sone, K. Nakata: *Surface and Coatings Technology* 2008, vol. 202 (22-23), pp. 5488–5492.

- [58] G. Lü, H. Cheng, C. Xu, Z. He: Chinese Journal of Chemical Engineering 2008, vol. 16 (2), pp. 314–319.
- [59] H. E. Hanninen: International Metals Reviews 1979, vol. 3 (241).
- [60] N. J. Laycock, R. C. Newman: Corrosion Science 1997, vol. 39 (10-11), pp. 1771–1790.
- [61] M. K. Ahn, H. S. Kwon, H. M. Lee: Corrosion 1998, vol. 40 (2), pp. 307–322.
- [62] a. Turnbull, K. Mingard, J. Lord, B. Roebuck, D. Tice, K. Mottershead, N. Fairweather, a.K. Bradbury: Corrosion Science 2011, vol. 53 (10), pp. 3398–3415.
- [63] D. Mesa, C. Garzón, a.P. Tschiptschin: Wear 2011, vol. 271 (9-10), pp. 1372–1377.
- [64] L. K. Zhu, Y. Yan, L. J. Qiao, A. a. Volinsky: Corrosion Science 2013, vol. 77, pp. 360–368.
- [65] P. C. Pistorius, G. T. Burstein: Corrosion Science 1994, vol. 36 (3), pp. 525–538.
- [66] G. T. Burstein, S. P. Vines: Journal of The Electrochemical Society 2001, vol. 148 (12), pp. B504–B516.
- [67] F. M. Bayoumi, W. a. Ghanem: Materials Letters 2005, vol. 59 (26), pp. 3311–3314.
- [68] T. Shibata, T. Haruna: Corrosion Engineering 1992, vol. 41, pp. 977– 987.
- [69] L. Fournier, M. Savoie, D. Delafosse: Journal of Nuclear Materials 2007, vol. 366 (1-2), pp. 187–197.
- [70] S. Cissé, L. Laffont, M.-C. Lafont, B. Tanguy, E. Andrieu: Journal of Nuclear Materials 2013, vol. 433 (1-3), pp. 319–328.
- [71] H. Khatak, P. Muraleedharan, J. Gnanamoorthy, P. Rodriguez, K. Padmanabhan: Journal of Nuclear Materials 1989, vol. 168 (1-2), pp. 157–161.
- [72] D. Desjardins, J. Daret, M. C. Petit, J. J. Pauthe: Corrosion Science 1980, vol. 20 (December 1978), pp. 177–187.
- [73] Y. Kondo: Corrosion Science 1989, vol. 45 (1), pp. 7–11.
- [74] S. Tsujikawa, T. Shinohara, C. Liang: Development of improved Type 304 stainless steel resistant to stress corrosion cracking in chloride environments: in: Proceedings of International Conference on Stainless Steels: 1991: pp. 196–203.
- [75] S. Pal, R. Ibrahim, R. Singh Raman: Engineering Fracture Mechanics 2012, vol. 82, pp. 158–171.
- [76] H. Fujikawa, N. Maruyama: Materials Science and Engineering: A 1989, vol. 120, pp. 301–306.
- [77] C. Liu, D. Macdonald: Journal of Pressure Vessel Technology 1997, vol. 119 (November), pp. 393–401.

- [78] O. Conejero, M. Palacios, S. Rivera: *Engineering Failure Analysis* 2009, vol. 16 (3), pp. 699–704.
- [79] V. Kain, K. Chandra, K. Adhe, P. De: *Journal of Nuclear Materials* 2004, vol. 334 (2-3), pp. 115–132.
- [80] CSI Stainless Steel Selection Guide: 2014.
- [81] Stainless Steel Grade Chart 2000,.
- [82] K. Lo, C. Shek, J. Lai: *Materials Science and Engineering: R: Reports* 2009, vol. 65 (4-6), pp. 39–104.
- [83] G. G. Shepel, V. S. Vakhrusheva, T. a. Dergach, S. a. Panchenko, a. a. Tereshchenko: *Steel in Translation* 2010, vol. 39 (12), pp. 1107–1110.
- [84] L. Jin: *Journal of Materials Engineering and Performance* 1995, vol. 4 (1), pp. 734–739.
- [85] R. C. Scarberry, D. L. Graver, C. D. Stephens: *Materials Protection* 1967, vol. 6 (6), pp. 54–57.
- [86] S. M. Hussaini, S. K. Singh, A. K. Gupta: *Journal of King Saud University - Engineering Sciences* 2013, , pp. 1–7.
- [87] C.-C. Wu, S.-H. Wang, C.-Y. Chen, J.-R. Yang, P.-K. Chiu, J. Fang: *Scripta Materialia* 2007, vol. 56 (8), pp. 717–720.
- [88] a. a. Popov, a. S. Bannikova, S. V. Belikov: *The Physics of Metals and Metallography* 2009, vol. 108 (6), pp. 586–592.
- [89] R. C. Newman 1985, vol. 25 (5), pp. 331–339.
- [90] M. Murayama, K. Hono, H. Hirukawa, T. Ohmura, S. Matsuoka: *Scripta Materialia* 1999, vol. 41 (5), pp. 467–473.
- [91] A. U. Malik, N. Siddiqi, I. N. Andijani: *Desalination* 1994, vol. 97 (1-3), pp. 189–197.
- [92] Y. Jiang, T. Sun, J. Li, J. Xu: *Journal of Materials Science and Technology* 2014, vol. 30 (2), pp. 179–183.
- [93] V. K. Lorenz, G. Medawar: *Thyssenferschung* 1969, vol. 3, pp. 97–108.
- [94] J. H. Cleland: *Engineering Failure Analysis* .
- [95] AL-6XN Alloy (UNS N08367) 2014,.
- [96] S. Heino: *Metallurgical and Materials Transactions A* 2000, vol. 31 (8), pp. 1893–1905.
- [97] B. S. DeForce: *NACE* 2017, .
- [98] L. F. Garfias-Mesias, S. R. Taylor: *NACE* 2016, (7837), pp. 1–9.
- [99] R. P. Reed 1975, vol. 6 (July).

- [100] T. Cassagne: Stress Corrosion Cracking of Stainless Steels in Chlorides Environments: in: Joint EFC NACE Workshop: 2007.
- [101] M. O. Speidel: Metallurgical Transactions A 1981, vol. 12A (May).
- [102] H. R. Copson: Effect of Composition on Stress Corrosion Cracking of Some Alloys Containing Nickel: Interscience Publishers, 1959: pp. 247–266.
- [103] U. Kamachi Mudali, P. Shankar, S. Ningshen, R. Dayal, H. Khatak, B. Raj: Corrosion Science 2002, vol. 44 (10), pp. 2183–2198.
- [104] Z. Begum, a. Poonguzhali, R. Basu, C. Sudha, H. Shaikh, R. Subba Rao, A. Patil, R. Dayal: Corrosion Science 2011, vol. 53 (4), pp. 1424–1432.
- [105] B. Chen, P. Flewitt, D. Smith: Materials Science and Engineering: A 2010, vol. 527 (27–28), pp. 7387–7399.
- [106] R. P. M. Procter 1990, vol. 25 (4).
- [107] S. Lynch: Acta Metallurgica 1988, vol. 36 (10), pp. 2639–2661.
- [108] T. Magnin, A. Chambreuil, B. Bayle: Acta Metallurgica 1996, vol. 44 (4), pp. 1457–1470.
- [109] T. Couvant, L. Legras, F. Vaillant, J. M. Boursier, Y. Rouillon 2005, (Figure 1), pp. 1069–1081.
- [110] M. Kamaya, T. Haruna: Corrosion Science 2007, vol. 49 (8), pp. 3303–3324.
- [111] H. S. Khatak, J. B. Gnanamoorthy, P. Rodriguez: Metallurgical and Materials Transactions A 1996, vol. 27 (5), pp. 1313–1325.
- [112] R. C. Newman: Stress-Corrosion Cracking Mechanisms: in: Corrosion mechanisms in theory and practice: 1995: pp. 311–372.
- [113] R. W. Staehle: Corrosion Science 2007, vol. 49 (1), pp. 7–19.
- [114] H. J. Dundas: Effect of Molybdenum on Stress Corrosion Cracking of Austenitic Stainless Steel.PDF: Tech. rep. 1975,.
- [115] D. k. Schroder: Resistivity: in: Semiconductor Material and Device Characterization: 3rd Edition: John Wiley & Sons, Inc., Hoboken, NJ, 2006: pp. 1–59.
- [116] Introduction to electrochemical scanning probe techniques: <http://research.shu.ac.uk/espnet/esp.htm>.
- [117] R. Sides: NACE Slides 2013, , pp. 1–11.
- [118] J. Liu, T. Zhang, G. Meng, Y. Shao, F. Wang: Corrosion Science 2015, vol. 91, pp. 232–244.

- [119] D. Macdonald, C. Liu, M. Urquidi-Macdonald, G. H. Stickford, B. Hindin, A. K. Agrawal, K. Krist: *Corrosion* 1994, vol. 50 (10), pp. 761–781.
- [120] R. Ovarfort: *Corrosion Science* 1988, vol. 28 (2), pp. 135–140.
- [121] E. Bettini, C. Leygraf, J. Pan: *International Journal of Electrochemical Science* 2013, vol. 8 (10), pp. 11791–11804.
- [122] S. Matsch, H. Böhni: *Russian Journal of Electrochemistry* 2000, vol. 36 (10), pp. 1122–1128.
- [123] G. S. Frankel, T. Li, J. R. Scully: *Journal of the Electrochemical Society* 2017, vol. 164 (4), pp. 180–181.
- [124] ASTM International 2014, vol. G48-11 (2009), pp. 1–11.
- [125] G. Qiao, Z. Zhou, J. Ou: *Proceedings of 1st IEEE International Conference on Nano Micro Engineered and Molecular Systems, 1st IEEE-NEMS 2006*, , pp. 541–544.
- [126] R. Akid, M. Garma: *Electrochimica Acta* 2004, vol. 49 (17-18), pp. 2871–2879.
- [127] Electrical or thermal conductivity, resistivity, density and melting point: <http://www.tibtech.com/conductivity.php> 2017,.
- [128] S. Bahamondes, S. Donoso, A. Ibanez-Landeta, M. Flores, R. Henriquez: *Applied Surface Science* 2015, vol. 332, pp. 694–698.
- [129] Y. Bai, X. Teng, T. Wierzbicki: *Journal of Engineering Materials and Technology* 2009, vol. 131.
- [130] ASTM International 2014, vol. G129-00, pp. 1–7.
- [131] R. Nishimura, Y. Maeda: *Corrosion Science* 2004, vol. 46, pp. 769–785.
- [132] Y. Bai, T. Wierzbicki: *International Journal of Fracture* 2009, vol. 161 (1), pp. 1–20.
- [133] R. Parkins: *Development of Strain-Rate Testing and Its Implications: ASTM*, 1979: pp. 5–25.
- [134] F. Mancia, A. Tamba: *Corrosion* 1986, vol. 42 (6), pp. 362–367.